MODULATION AND CONTROL OF CHARGE TRANSPORT THROUGH SINGLE MOLECULE JUNCTIONS

by

KUN WANG

(Under the Direction of Bingqian Xu)

ABSTRACT

Building electronic devices out of single molecules has been the ultimate goal of downscaling electric circuits. Understanding charge transport through single-molecule junctions is central to achieving this goal. To gain deeper insights into charge transport through single molecules, this dissertation centers on detailed experimental modulation and control of charge transport through single-molecule junctions using modified scanning probe microscope break-junction (SPM-BJ) techniques.

First, I explored the effect of molecule-electrode contact interfaces. Using force-conductance cross-correlation analysis, I mapped out the correlation between conductance and force of modulated Au-octanedithiol-Au junctions measured with CAFM-BJ. The investigation of the conductance change during junction elongation showed a unique contact tunneling barrier of octanedithiol, which was interpreted by a newly developed contact barrier model. A systematic control of anchoring groups of benzene-based molecular junctions showed that current rectification occurred whenever asymmetric anchoring groups were introduced, which is mainly due to asymmetry in potential drop across the contacts.

Second, I studied the impact of DNA's structural change on its conductance. The conductance of poly $d(GC)_4$ DNA duplex was found to decrease by two orders of magnitude during a B- to Z-form structural transition, which is mainly attributed to the breaking of π-π stacking between adjacent base pairs caused by the transition. Using stretch-hold mode STM-BJ technique, the structural transition was successfully monitored solely based on conductance measurements.

Then, I attempted to modify the structure of DNA for functional I-V feature. A DNA-based molecular rectifier was for the first time constructed by site-specific intercalation of coralyne molecules into a custom-designed DNA duplex. Measured I-V curves of the resulting DNA-coralyne complex showed strong rectification with a rectification ratio of 15 at 1.1V. Based on NEGF-DFT calculations, this rectification is mainly caused by asymmetric coupling of the HOMO-1 level to the electrodes when an external bias is applied, an unprecedented rectification mechanism.

Finally, Fermi level pinning of charge transfer resonances was investigated in junctions composed of terthiophene containing molecular wires.

Taken together, these results not only provide new understanding of charge transport through molecules, they also opened new route for building functional molecular electronic devices.

INDEX WORDS: Molecular electronics (ME), Single-molecule junction, Scanning probe microscope break-junction (SPM-BJ), Scanning tunneling microscope break-junction (STM-BJ), Conductive atomic force microscope break-junction (CAFM-BJ), Single-molecule conductance, Molecule-electrode contact interfaces, DNA, Structural transition, Current-voltage (I-V) characteristics, Rectification, Quantum interference, Fano-resonance.

MODULATION AND CONTROL OF CHARGE TRANSPORT THROUGH SINGLE MOLECULE JUNCTIONS

by

KUN WANG

BS, Shandong University, China, 2011

A Dissertation Submitted to the Graduate Faculty of The University of Georgia in Partial Fulfillment of the Requirements for the Degree

DOCTOR OF PHILOSOPHY

ATHENS, GEORGIA

2016

MODULATION AND CONTROL OF CHARGE TRANSPORT THROUGH SINGLE MOLECULE JUNCTIONS

by

KUN WANG

Major Professor: Bingqian Xu
Committee: Steven Lewis
Susanne Ullrich

Electronic Version Approved:

Suzanne Barbour
Dean of the Graduate School
The University of Georgia
December 2016

DEDICATION

To

My parents, Yimin Liang and Chengren Wang, and my wife, Yan Du.

ACKNOWLEDGEMENTS

I would first and foremost like to express my greatest appreciation and special thanks to my major advisor Professor Bingqian Xu for his invaluable guidance, academic advices, and financial support throughout my PhD. His enthusiasm and motivation were always pushing me forward and this definitely transformed me to be a better scientist. I would not have been able to step over the obstacles and difficult times without his constant help. I would also like to thank the supportive and knowledgeable committee members, Professor Steven Lewis and Professor Susanne Ullrich, for useful discussion, advice and support during my PhD. Much appreciation goes to the rest of the research group, both past and present, including Dr. Cunlan Guo, Mr. Joseph Hamill, Dr. Bin Wang, Dr. Mengmeng Zhang, Ms. Tong Zhang and Mr. Alex Reese for helping me in my PhD research.

I would also like to thank the help of our collaborators, Professor Simon Higgins and Dr. Andrea Vezzoli of University of Liverpool, UK and Professor Yonatan Dubi and Ms. Elinor Zerah-Harush of Ben-Gurion University of the Negev, Israel. The current form of the dissertation is made possible due to their hard work and helpful suggestions.

It is undoubtedly true that the life of a PhD student goes far beyond laboratory walls. I would like to thank all the wonderful people I met that made me feel welcome in Athens, GA - the bulldog nation which has become my second hometown. I also appreciate the friendship I have built with many fantastic human beings who have accompanied me along this bitter and sweet journey.

In particular, I would like to thank my mother and my father for their constant love and support. I am proud to be your son, and I hope I can make you proud, too.

Final thanks go to the most important person in my life. Yan, I could not have this done without you, your love, your help, your support and your kindness.

As a closing remark, I would like to quote Claude Bernard: *The joy of discovery is certainly the liveliest that the mind of man can ever feel*. But this ultimate joy was, is and will be only deserved after going through mistakes, failures, depression, and confusion which again and again served as the excuse to steer you away from the truth. Stay focused and keep going, the final result will be different.

TABLE OF CONTENTS

Page

LIST OF TABLES

Page

LIST OF FIGURES

Page

CHAPTER 1

INTRODUCTION AND BACKGROUND

1.1 History of Molecular Electronics

Over the past half a century, the development of microelectronic industry has been governed by a golden rule known as Moore's Law, where, as a result of electric circuit miniaturization, computing power have doubled every two years or so.[1] As the Moore's Law-driven silicon-chip industry is approaching to an end, alternative materials and technologies for building tinier, faster electronics are highly in demand. Stimulated by the desire to search for candidate materials, researchers have looked at the possibility of using single molecules as building blocks in electric circuits since the 1970s. This concept of building electronic component out of single molecules is called molecular electronics (ME). Molecular circuits built by this attractive idea could raise device density by a factor of ~10^4 compared to the current level of solid state devices.[2] Equally important is that the conceived nanometer long single-molecule device will add an overwhelming degree of functionality and structural flexibility, which enables the fabrication and design of low-cost self-assembled molecular circuits, structure-determined molecular switches, nanoscopic quantum interference and electrochemically controllable molecular devices that has no analogy in conventional solid state electronics.[3, 4]

One important driving force of the field of ME was the theoretical proposal by Aviram and Ratner in 1974, where a molecular rectifier was conceived by wiring a molecule to two metallic electrodes (**Figure 1.1A**).[5] It for the first time suggested the possibility of making and measuring a single-molecule circuit from the theoretical perspective. Unlike the continuous and condensed energy-band dispersion of bulk materials, the energy levels, molecular orbitals (MOs), are quantized and discrete in a nanometer-scale molecule.[6, 7] This quantized feature is what distinguishes single-molecular devices from classical p-n junctions.[6] The energy gap resides between the highest-occupied (HOMO) and the lowest-unoccupied molecular orbital (LUMO) is called the HOMO-LUMO gap (HLG).[8] Just like the Fermi level of bulk electrodes varies from material to material, the HOMO and LUMO differ from molecule to molecule. Thus bridging an individual molecule between two metallic electrodes results in the merging of discrete states into continuous states. This unique trait is believed to lead to intriguing electrical and mechanical properties.

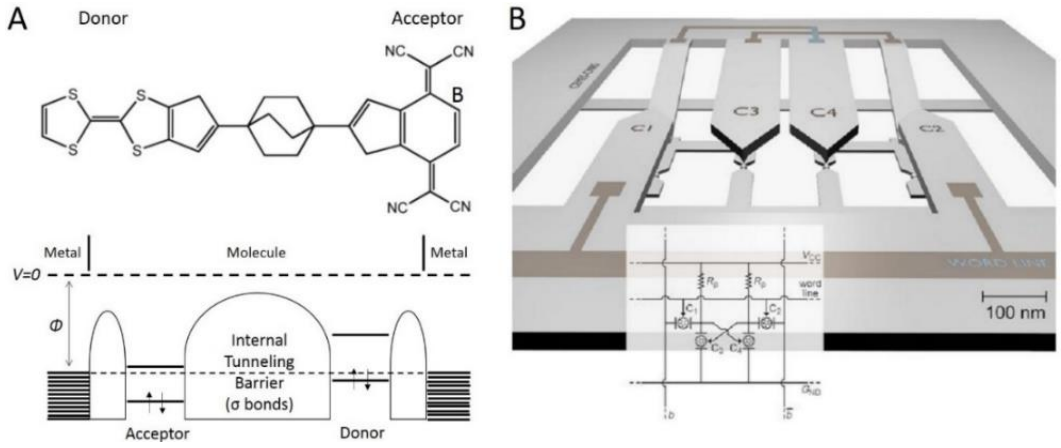

Figure 1.1 (A) Molecular rectifier proposed by Aviram and Ratner in 1974. Reprinted from ref. 5 with permission from Elsevier. (B) Example architecture of a hybrid molecular electronic device

proposed in Aviram's review paper in 2000. Reprinted from ref. 19 by permission from Macmillan Publishers Ltd, copyright (2000).

With this initial excitement, a large body of research has been spurred.[9-13] However, in the decade since the concept of ME was conceived, no significant progress has been achieved by experimentalists. Wiring a molecule to the electrodes or attaching the electrodes to molecules turned out to be the biggest challenge. Experimental efforts following this "bottom-up" approach were made employing increasingly smart unconventional means: using mercury drops as electrodes,[11] using Lorentz force to cross metallic wires,[9] and trapping molecules in a nanopore.[12, 13] But the experimental results turned out to be chaotic and not reliable enough. Other techniques involving sandwiching robust molecules between electrode layers were proven to be too destructive for small molecules.[10, 14, 15] Achieving a reliable contact of molecule and electrodes was hardly reachable, and remained a major obstacle that hindered the progress of science towards single-molecule device for more than a decade.[16]

In the 1990's, it was the development of scanning tunneling microscopy (STM) and later the atomic force microscopy (AFM) that brought us the most significant breakthrough in molecular electronics.[17] It rapidly turned out that these scanning probe microscopy (SPM) techniques could realize the measurement of electrical signals, like conductance and I-V characteristics, at the single molecule level (see **1.3** for details). The first experimental attempt of determining the conductance of a molecule was conducted by Mark Reed's group at Yale University, collaborating with James Tour's group, then at the University of South Carolina.[18] They stretched a gold wire in the solution of sample molecules until breakage occurred, which resulted in the formation of two tips of atomic

sharpness covered by molecules. Then two tips where brought together by means of a piezo-controlled bendable substrate while measuring the current flow.[18] Using this method, they successfully tested the current-voltage characteristics of benzene-1,4'-dithiol molecules. The invention of this technique, now known as mechanically controlled break junction (MCBJ), has proven to be a significant breakthrough in the field of ME and also served as the precursor for the development of the widely-used SPM-BJ techniques. Then review papers by Aviram et al. and a few others in the early 2000s summarized the proposed molecular structures of the day that were promising for building electronic rectifier, switches and storages, and also pictured the possible architecture of hybrid molecular circuits (**Figure 1.1B**).[19] Meanwhile, worldwide interest was sparked due to their success. This point in time was marked as the true beginning of molecular electronics.[17]

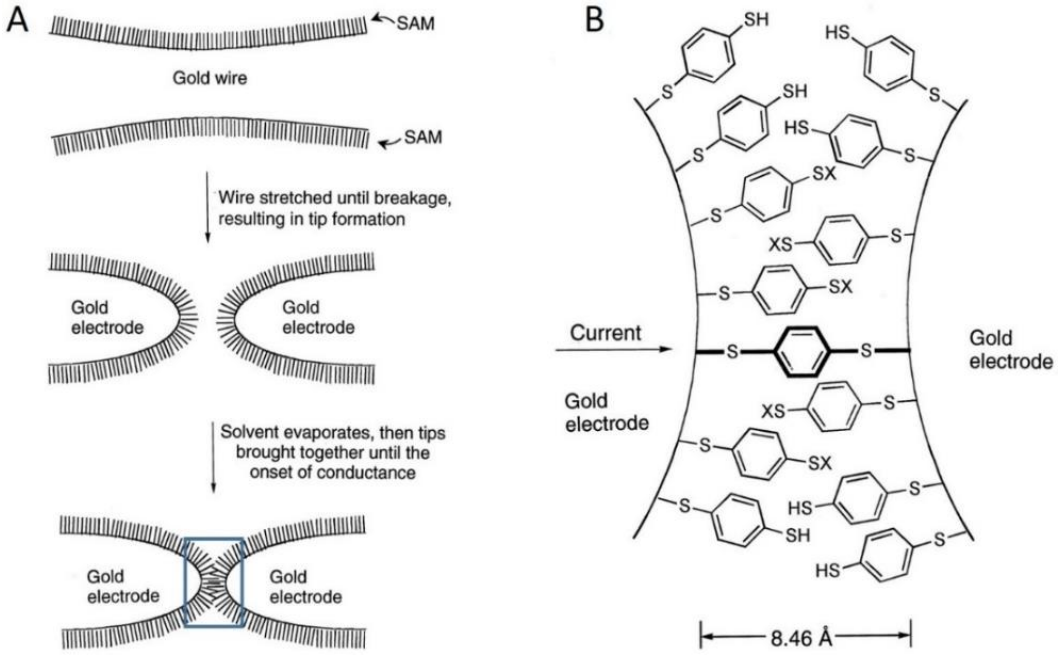

Figure 1.2 Experimental work by Mark Reed et al. in 2000. (A) Schematic of measurement process. (B) A schematic of a benzene-1,4-dithiolate SAM between proximal gold electrodes (enlarged view of the squared area in A). Reprinted from ref. 18 with permission from AAAS.

1.2 Charge Transport in Molecular Junctions

Charge transport through a molecule that is wired between two electrodes is dominated by quantum tunneling effect because molecule is a nanoscopic object. Although the most appropriate theoretical language is still evolving, the Landauer-Buttiker formalism[20, 21] is perhaps the most well accepted theoretical framework for describing ballistic transport in one dimension nanoscopic object. In this formalism, electron transport problem is converted into a scattering problem. The energy distribution of electrons entering the left (right) electrode from the left (right) reservoir is $f_{left}(E)(f_{right}(E))$ and according to the Landauer-Buttiker formula, the current passing from left to right is

$$I = \left(\frac{2e}{h}\right)\int_{-\infty}^{\infty} dET(E)\left[f_{left}(E) - f_{right}(E)\right] \tag{1.1}$$

where e is the charge on one electron, h is Planck's constant, E is energy, $T(E)$ is transmission coefficient for electrons passing from one electrode to the other electrode via the molecule and f is the Fermi-Dirac distribution of energy at the electrodes.

Close to equilibrium, $f_{left}(E) = \left[e^{\beta\left(E-E_F^{left}\right)} + 1\right]^{-1}$ and $f_{right}(E) = \left[e^{\beta\left(E-E_F^{right}\right)} + 1\right]^{-1}$, where E_F^{left} (E_F^{right}) is the Fermi-energy of the left (right) electrode and $\beta = \frac{1}{k_B T}$, where k_B is Boltzmann Constant and T is temperature. When a

voltage difference of V is applied between the left and right electrode, then $E_F^{left} = E_F + \frac{eV}{2}$ and $E_F^{right} = E_F - \frac{eV}{2}$. This suggests that at zero temperature, but finite voltage

$$I = \left(\frac{2e}{h}\right) \int_{E_F - eV/2}^{E_F + eV/2} dET(E) \tag{1.2}$$

To obtain the conductance of a metal-molecule-metal junction, one needs to average $T(E)$ over an energy window of width eV centered on the Fermi energy. If $T(E)$ does not change significantly over eV, the Fermi functions can then be Taylor expanded to yield electrical conductance in the zero-voltage, finite temperature limit:

$$G = \frac{I}{V} = G_0 \int_{-\infty}^{\infty} dET(E) \left(-\frac{df(E)}{dE}\right) \tag{1.3}$$

where G_0 is the quantum of conductance and has a value of $\frac{2e^2}{h} \approx 77.48 \mu S$.

Finally, the conductance G of a metal-molecule-metal junction is given by

$$G = G_0 T(E_F) \tag{1.4}$$

The above expressions assume that an electron remains phase coherent as it passes from one electrode to the other and does not undergo inelastic scattering.[22] This has been proven to be a reasonable assumption for short molecules.[23] However as the length of a molecule increases, the probability of inelastic scattering (e.g. from phonons or other electrons) becomes non-negligible[24] and the above expressions require further correction or modification.

1.3 Single Molecule Break-Junction Technique

The major barrier experimentalists had to come across in the early 2000s lied in the large fluctuations in the data sets of the conductance measurements. It was difficult to determine how many molecules were bridged across the electrodes and how many

contributed to the measured results. Many discrepancies emerged not only between experimental data and simulated results, but also among data sets collected from different labs.[25-30] This later was mainly attributed to the lack of appropriate controls of experimental conditions, such as making solid contact between a molecule and two electrodes and reproducing similar molecule-electrode contact structure. Therefore, what was in urgent need back then was a repeatable and reliable experimental platform that could at least minimize the fluctuations in experimental data, and raise confidence for further investigation.

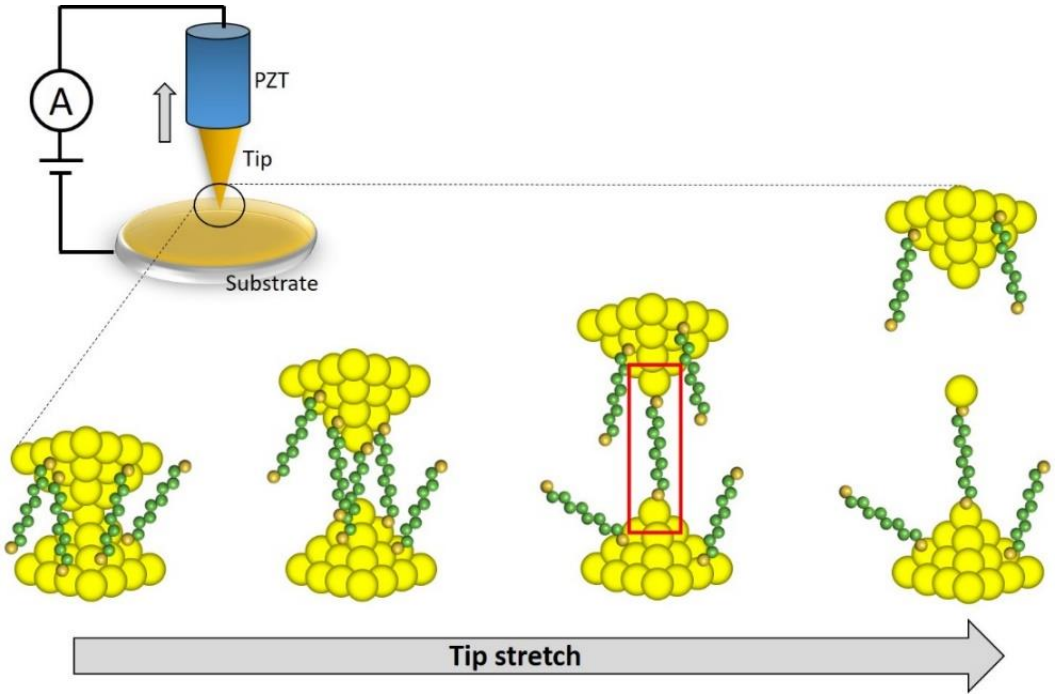

Figure 1.3 Working principle of STM-BJ technique. Molecular junction composed of an individual molecule, namely single-molecule junction, is marked by red rectangle.

Meeting with the imperative requirement of the field, Xu and Tao's work in 2003 realized a repeatable STM break junction (STM-BJ) method.[31] This method provided a robust and tunable experimental platform to repeatedly create metal-molecule-metal

junctions. As shown in **Figure 1.3**, this method involved using a metallic STM tip as one electrode and a metallic substrate as the other electrode. Via the control of piezoelectric transducer (PZT), the STM tip was brought close to the substrate covered by sample molecules. The feedback loop was disengaged and the tip was pushed into contact with the substrate. It was then retracted while the tunneling current was monitored. A fresh metal-metal atomic junction is formed, and on retraction this thins down to a single atom (point contact), which is finally broken upon further withdrawal. This process results in plateaus in conductance traces at multiples of the quantum unit of conductance G_0 ($2e^2/h$; 77.5μS, e is the electronic charge, and h is Planck's constant) owing to atomic rearrangements in the junction (**Figure 1.4A**). When the point contact breaks, if no molecule is trapped in the resulting break junction then the final step down of G_0 is followed by a sharp exponential decay as the tip continues to retract (**Figure 1.4E**), but if a molecule (or molecules) binds to both gold contacts, then subsequent additional plateau(s) are seen in the current–distance plot at conductances $\ll G_0$, corresponding to tunneling conductance through the molecule (**Figure 1.4B**). Eventually, as retraction continues, the metal-molecule-metal junction breaks down whereupon the current rapidly falls to a very low value consistent with tunneling through space once more. Thus the last significant step before the conductance falls to zero is the conductance across an individual molecule. By repeating this engaging-retracting cycle thousands of times, statistical analysis of thousands of similar conductance traces could reveal peaks at the positions where plateaus most frequently appear in a conductance histogram (**Figure 1.4D**). The first prominent peak in the histogram was believed to be the conductance when only one individual molecule was left in the break junction, namely, the single-

molecule conductance. This method washed out the contact variations to a certain extent, and eliminated most discrepancies in earlier measurements. Now it is the most widely used method for studying electron transport in single-molecule junctions.

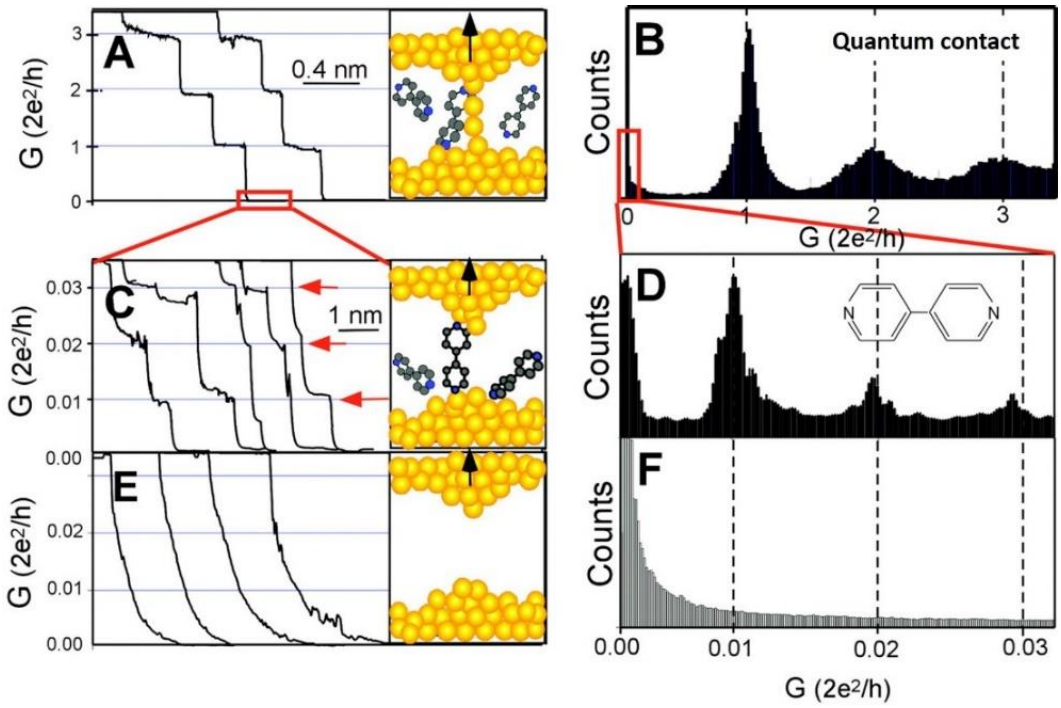

Figure 1.4 STM-BJ experimental results by Xu and Tao in 2003. Reprinted from ref. 31 with permission from AAAS.

An analogy to STM-BJ method is a conductive AFM break-junction (CAFM-BJ). CAFM-BJ uses a metal-coated AFM tip as the tip electrode and involves a laser-reflection controlled force signal detector, which enables measurements of conductance and force in parallel (**Figure 1.5B**). Notice that CAFM-BJ works the same way STM-BJ does, but adds one more detectable parameter, force, to the system. Other techniques employing the emerging STM technique were also developed at the same time. The *I(s)* (called *I(z)* in some literatures) technique introduced by Haiss et al. in 2003 also used a STM tip to form molecular junctions.[32] But the core difference is the junction formation

method. The *I(s)* method avoids the contact between two metal electrodes. The STM tip approaches the surface of analyte molecules, then retracts away while the tunneling current is measured. Schematics of the *I(s)* technique and the corresponding conductance signal are exemplified in **Figure 1.6A**. A further development using STM employs similar ideas but focuses on the time domain and has been referred to as the *I(t)* method, as exemplified in **Figure 1.6B**.[33] The STM tip is placed at a constant distance from the substrate. This distance is usually set to be less than the length of a fully extended molecule. Then characteristic vibrations in current can be monitored which behave like telegraphic noise signals (rightmost panel in **Figure 1.6B**). Current jumps have been attributed to the attachment or detachment of the molecule to or from the STM tip. The conductance can then be determined by calculating the peak value of the current jump and the applied bias.[34] Another important method, mechanically controlled break-junction (MCBJ), uses notched metal wire fixed on elastic substrate.[18, 35-37] A diagram of MCBJ is shown in **Figure 1.6C**. The substrate is usually covered with an insulator, and the metal wire is mechanically broken by bending the substrate. A single-molecule break junction is formed when only one molecule is left in the gap between two terminals of the broken metal wire. These aforementioned methods collecting signals by sandwiching a single molecule in a scheme of break junctions are called single-molecule break junction (SMBJ) techniques.

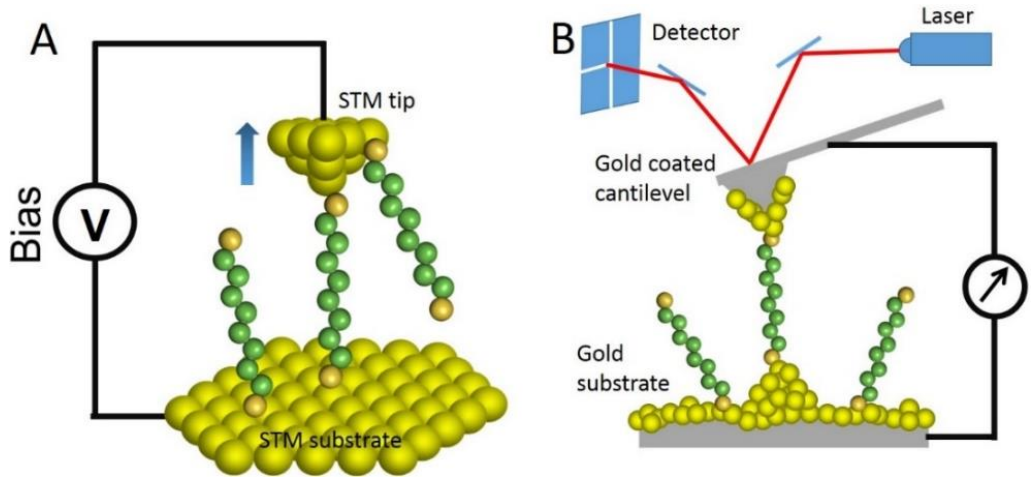

Figure 1.5 Comparison of STM-BJ (A) and CAFM-BJ (B).

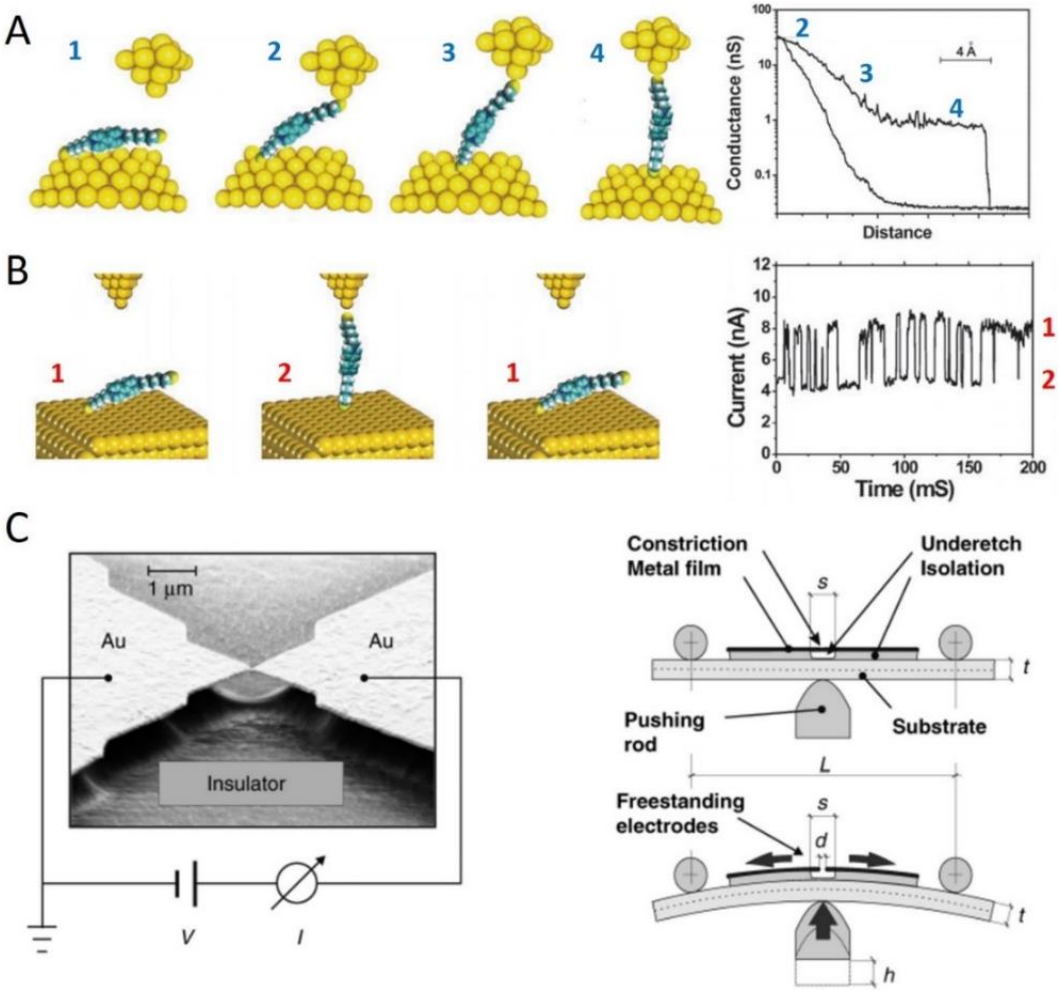

Figure 1.6 (A) *I(s)* or *I(z)* technique. (B) I(t) technique. (C) MCBJ technique. A and B are reproduced from ref. 34 with permission of The Royal Society of Chemistry. C is reprinted with permission from ref. 37. Copyright John Wiley & Sons, Inc..

To date, using these SMBJ techniques, especially the widely adopted, experimentalists have obtained extensive data, and phenomena of great interest, such as rectification,[38-40] negative differential resistance,[41-43] Kondo effect,[44-46] redox switching,[47, 48] spins-split molecular orbitals,[49] magnetoresistance,[50] thermoelectrics,[51, 52] and quantum interference,[53-55] have been observed in the past decade, which greatly boosts the development of molecular electronics.

1.4 Objectives and Outline of Dissertation

Despite the fact that much effort in using SMBJ techniques has been devoted to measure the conductance of various molecules, physical understanding of many detailed information hidden in the chaotic experimental data and some unresolved issues in the field, such as the influence of molecule-electrode contact interfaces and the creation of large current rectification, have been impeded by the lack of proper experimental controls and appropriate analysis techniques. In agreement with this view, it is believed that delicate experimental controls and advanced data analysis algorithms are not only essential to understanding charge transport through single-molecule junctions, they will also provide significant hints for future experimental and theoretical investigations. Therefore, the research presented in this dissertation aims at gaining deeper insights into charge transport properties of single-molecule junctions via incorporating delicate experimental modulations and controls based on the widely adopted STM/CAFM-BJ techniques and developing more powerful data analysis methods. In particular, my

dissertation research addresses several challenging issues in the field of ME, including 1) the role of molecule-electrode contact interfaces in determining charge transport through single-molecule junctions, 2) the structure-property relation of DNA-based molecular junctions, 3) the creation of DNA-based molecular rectifier, and 4) quantum interference effect (Fano-resonance) in molecular junctions.

In this chapter I have briefly summarized the history and motivation of the field of molecular electronics and introduced the most reliable experimental approaches, the emerging SMBJ techniques, for studying charge transport through single-molecule junctions. I have also elaborated the objectives of this dissertation. The rest of the dissertation will be organized as follows:

Chapter 2 describes the general experimental procedures of STM/CAFM-BJ measurements used in my research, including sample preparation, conductance measurement setups and I-V measurement setups. Data analysis methods used for conductance and I-V measurement results will also be introduced.

Chapter 3 describes the successful depiction of details of contact effect in modulated Au-octanedithiol-Au junctions by combining mechanical modulation of CAFM-BJ technique and force-conductance cross-correlation analysis. The investigation of the conductance change during junction elongation of the mechanical modulation process which revealed a unique contact tunneling barrier of Au-octanedithiol-Au junctions is also presented.

Chapter 4 introduces the measurements and understanding of the role of asymmetric contact interfaces formed by inconsistent anchoring groups in benzene-based molecular junctions in producing current rectification behavior. The underlying

mechanism of the observed rectification interpreted by a modified Simmons model is also introduced.

Chapter 5 describes the experimental investigation of the role of DNA's secondary structure in determining its conductance, where single-molecule conductance of a poly $d(GC)_4$ DNA duplex was electronically monitored during its structural change from B- to Z-form.

Chapter 6 demonstrates the experimental creation of the world's first DNA-based molecular rectifier by intercalating small molecules, coralyne, into a custom-designed DNA duplex. The underlying transport mechanism suggested by NEGF-DFT calculations is also introduced.

Chapter 7 describes the experimental studies of Fermi level pinning of charge-transfer resonances in molecular junctions containing the 2,2':5',2"-terthiophene:TCNE charge-transfer complex.

Chapter 8 briefly summarizes the research presented in this dissertation and remarks on the future direction of single-molecule junction studies.

CHAPTER 2

EXPERIMENTAL PROCEDURES AND ANALYSIS METHODS

In the experimental works presented in this dissertation, I employ either STM-BJ or CAFM-BJ techniques, where junctions are repeatedly formed and broken thousands of times in the course of a typical experiment. This chapter describes the general experimental protocols used to carry out these measurements, and the analysis methods I have applied to the large datasets obtained in my experiments.

2.1 STM/CAFM Break Junction Measurement Setups

2.1.1 Sample preparation

In all the works presented in this dissertation, for both STM-BJ and CAFM-BJ measurements, gold (Au) substrates and gold (Au) tips are used as the BJ electrodes. Gold substrates were prepared by evaporating ~100nm of gold onto freshly cleaved mica sheets using a thermo-evaporator under a vacuum of 10^{-7} Torr. The gold beads for Au substrate deposition was purchased from Kurt J. Lesker Company (99.999%), and mica sheets were purchased from Ted Pella, Inc. The Au surfaces were annealed in hydrogen flame for several minutes immediately before immersion in sample solutions containing analyte molecules. This annealing step cleaned the surface and allowed epitaxial reconstruction of the Au to form large terraces of Au(111). Then sample solution containing target molecules was dropped onto the freshly flamed Au surface to form the

required self-assembled monolayer for the following electrical measurements, including conductance measurements and I-V characteristics measurements.

Au tips for STM-BJ measurements were prepared by shearing gold wire with diameter of 0.25 mm (99.999%, Alfa Aesca). Freshly sheared bare Au tips were directly used for measurements that were performed in air. In order to conduct measurements in aqueous solution, the STM tips were coated with Apiezon wax to keep ionic leakage current below 1pA to avoid ionic conduction. Tips for CAFM-BJ measurements were obtained by depositing a 15nm layer of chromium and then a 35nm layer of gold (99.999%) to normal AFM tips using an ion beam coater (Gatan model 681). The spring constant of the AFM cantilever used in my experiments is 40N/m. The SPM system used for both STM-BJ and CAFM-BJ measurements is the Picoplus SPM (Molecular Imaging) with a Pico Scan 3000 Controller (Molecular Imaging).

2.1.2 Measurement protocols

Conductance measurements: The single-molecule conductance of a sample molecule was measured under a certain static bias voltage that was applied to the Au substrate with the Au tip grounded. The general procedures for conductance measurement of a molecule followed the STM/CAFM-BJ techniques detailed in Chapter **1**. In these techniques, the tip was initially driven by piezoelectric transducer (PZT) to approach the Au substrate until the current reached a preset value which implied the formation of Au-Au point contact. Then the tip retracted so that conductance vs distance trace was recorded. This process was repeated for thousands of times in a typical conductance measurement to generate thousands of conductance vs distance traces for further data

analysis, including the construction of conductance histograms and correlation analysis. Both a linear-binned preamplifier and a logarithm-binned preamplifier were used for the conductance measurements. The reason for using a log-scale preamplifier is to monitor a much wider range of conductance distribution which covers the whole junction evolution during tip retraction, from the breaking of Au-Au point contact to the rupture of the last molecular junction. Example linear-scale and log-scale conductance traces are shown in **Figure 2.1A** and **2.1B**, respectively. When CAFM-BJ technique was used, the force and conductance signals can be simultaneously measured, which helps to discover the correlation between mechanical and electrical properties of studied molecular junctions. Example force and conductance traces obtained simultaneously by CAFM-BJ technique is shown in **Figure 2.1C**.

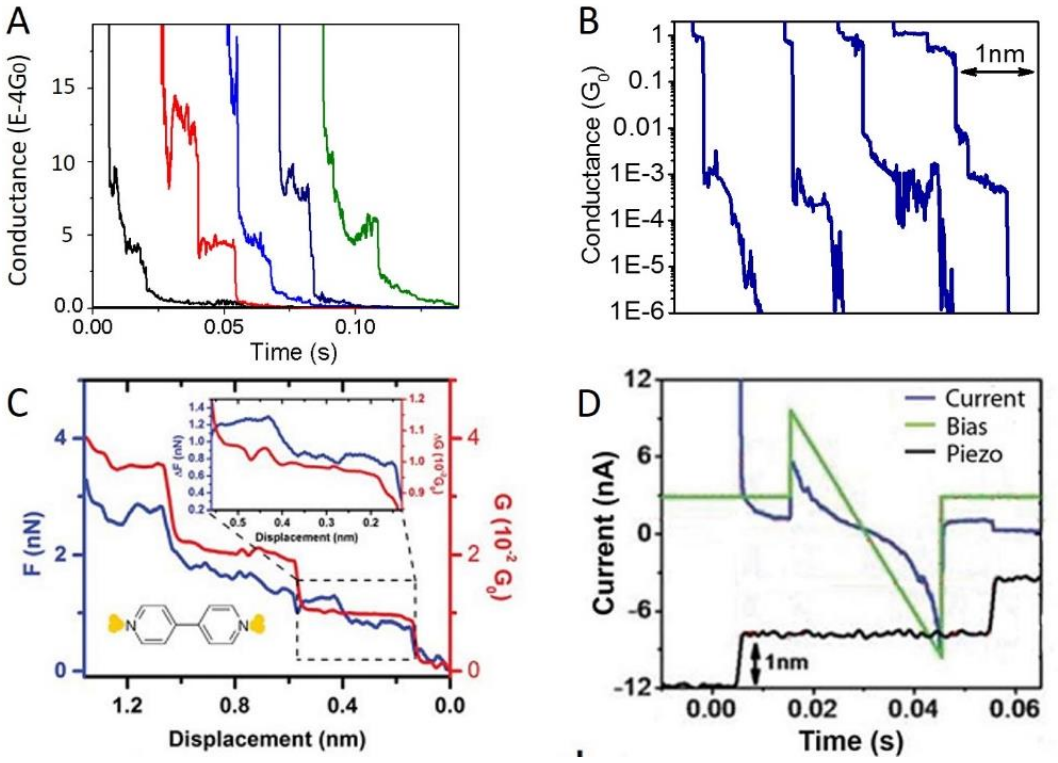

Figure 2.1 Example BJ measurement results. (A) Typical linear-scale conductance vs time traces. (B) Typical log-scale conductance vs stretching distance traces. (C) Typical force and

conductance traces simultaneously measured by CAFM-BJ technique. Reprinted from ref. 58. (D) Typical I-V curve obtained from a single-molecule junction. Reprinted from ref. 6.

I-V curve measurements: The current-voltage (I-V) characteristics of a single molecule junction is measured by applying a bias sweep from a negative (positive) bias value to a positive (negative) bias value (e.g., from -1V to 1V) when the molecular junction containing an individual molecule is stabilized by a stretch-hold modification. The method is detailed in Section **2.2** in this chapter. Example I-V curve obtained from a single-molecule junction is shown in **Figure 2.1D**. The determination of whether or not a single molecule is sandwiched in the junction is based on the single-molecule conductance value of the first and most prominent peak in the corresponding conductance histogram obtained from previous conductance measurements. It is necessary to notice that only the I-V curves extracted from single-molecule conductance plateaus are considered as I-V characteristics of single molecule junctions and further used for I-V curve analysis.

2.2 Mechanical modulations

Deep understanding of charge transport through single molecules requires delicate experimental controls of single-molecule junction system. The power of the scanning probe microscopy (STM/AFM) experimental setup comes from the fact that the piezoelectric transducer (PZT) provides precise displacement of the SPM tip, allowing for the gap between the tip and substrate to be adjusted in different fashions. In this section, the mechanical modulations I have applied in my experiments is discussed.

Continuous-stretch mode: Conventional SPM-BJ measurements usually apply a constant tip retracting speed throughout the whole measurements, and the PZT signal appears to be a straight line (blue line in **Figure 2.2A**). This measurement procedure is named as the "continuous-stretch mode" SPM-BJ. Although widely adopted, continuous-stretch mode SPM-BJ measurements often show conductance plateaus that is noisy and short-lived. This usually results in a single-molecule conductance peak with rather broad distribution and low intensity, which might wash out details important for understanding the SMBJ systems it is measuring.[56]

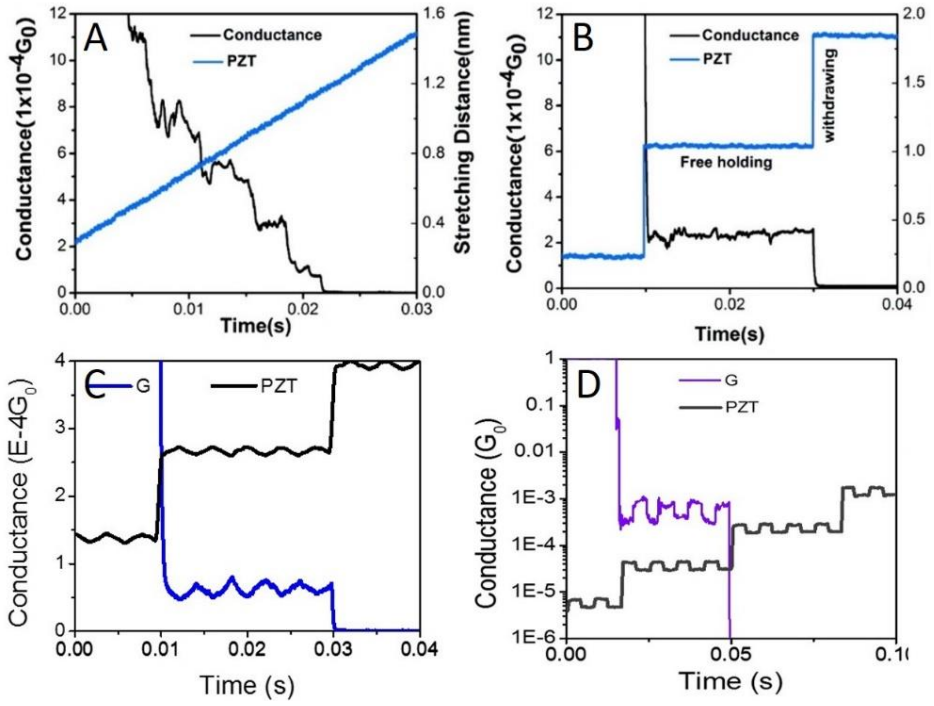

Figure 2.2 SPM-BJ measurement results under different mechanical modulations. (A) PZT movement (blue) and conductance signal (black) of continuous-stretching mode. (B) PZT movement (blue) and conductance signal (black) of stretch-holding mode. (C-D) PZT movement (black) and conductance signal (C: blue; D: purple) of nonlinear-ramp modulations. A and B are reprinted with permission from ref. 56. Copyright (2009) American Chemical Society. C is reprinted from ref. 61.

Stretch-hold mode: The peak shape of the conductance histogram is predominantly determined by the stability of the molecular junction conformation. Thus, the ability to stabilize the molecular conformation while it is measured is necessary. In my experiments, the stretch-hold modification was used which involves stair-stepping the tip retraction process so that the system pauses or holds momentarily and allows for the junction to settle into a quasi-relaxed state.[56] This modification essentially includes periodic repetition of two processes: 1) abrupt stretch of a certain distance and 2) free-holding of the junction separation for certain time. As shown in **Figure 2.2B**, measured under stretch-hold modification, the conductance plateau became much more distinct and well-defined, and the junction had a much longer lifetime during the free-hold process. This modification of the tip retraction was proven to eliminate, or at least minimize, the variations of experimental conditions, such as the fluctuation of the junction conformation.[56] In addition, while a single-molecule junction is free-held, a bias sweep can be applied to measure the I-V characteristics of the molecular junction.

Equally important is that the free-held junction serves as a perfect platform to carry additional mechanical modulations of the junction separation, which enables the discovery of more detailed information of single-molecule junction systems.

Non-linear ramp modulations: On a free-held junction achieved by setting up a constant tip-substrate separation using the stretch-hold modification, the SPM tip can also be modulated to cycle through multiple non-linear ramp modes, such as “triangle, “trapezoidal” and “wave” displacements. This could be achieved by applying an AC signal with a certain shape and frequency to the SPM PZT movement. Modulations in this manner essentially regulates the junction separation by compressing and elongating

the molecular junction periodically. Example conductance traces obtained under a "triangle" and a "trapezoidal" modulation are shown in **Figure 2.2C** and **2.2D**, respectively. I emphasize that measurement results obtained by non-linear ramp modulations carry significant information associated with the mechanical and electrical properties of the studied junction. In my experiments, "triangle or saw-tooth" and "trapezoidal" modulations have been specifically applied to measure junctions containing different molecules.

2.3 Data Analysis Methods

As, usually, neither how many molecules form the junction for any given experiment, nor the exact nature of the metal–molecule bonding are known, many measurements are made and the results are analyzed statistically to determine the most probable conductance of a single molecule. To plumb as many details as possible from the collected data, numerous statistical methods have been developed and used in my dissertation research.

2.3.1 One-dimensional (1D) and two-dimensional (2D) histogram methods

Firstly introduced in Xu and Tao's work,[31] the single-molecule conductance can be determined using a conventional one-dimensional (1D) conductance histogram constructed from many individual conductance traces. Typical conductance 1D histograms under a linear-scale and log-scale binned plot are shown in **Figure 2.3A and B**, respectively. These 1D histograms exhibit peaks, the center value of which is the most probable conductance of a single molecule. Histograms are generated by directly determining the height of each conductance jump in the conductance vs distance scans

and plotting these values in histograms of counts against conductance jump value. However, the 1D conductance histogram only involves one significant parameter: conductance. Therefore, it cannot reveal other detailed features hidden in the conductance vs distance traces (i.e. the junction length and correlation between two traces). To have a straightforward glance at junction evolution feature, two-dimensional (2D) conductance histogram is also used in the analysis of my experimental results. 2D histogram is achieved by superimposing hundreds of conductance traces that are shifted to an identical starting or ending point and then illustrating the data points with an additional coordinate binned in color code. Using this method, the average junction length prior to junction rupture can be clearly reflected. It can also illustrate interesting charge transport phenomenon, such as conductance switching, which cannot be reflected in a 1D histogram. Example 2D histograms obtained from measurements under continuous-stretch mode and non-linear ramp modulation are shown in **Figure 2.3C** and **2.3D**, respectively.

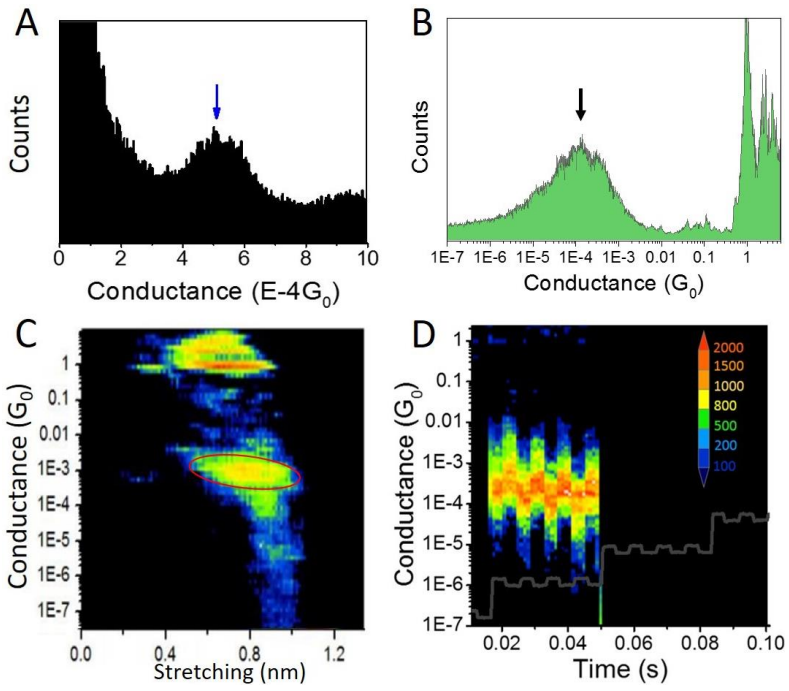

Figure 2.3 1D and 2D histograms. (A) Linear-scale conductance 1D histogram. (B) Log-scale conductance 1D histogram. (C) Log-scale conductance 2D histogram. (D) Log-scale 2D conductance histogram obtained from mechanical modulation measurements.

2.3.2 Correlation analysis

The generation of defined peaks in ‘‘all-conductance’’ histograms relies on there being a relatively flat current-plateau region before the junction is cleaved. However, two types of information that could be readily washed out using histogram methods are 1) conductance–distance curves carrying jump events which are closely related to mechanical nature of molecular junctions and 2) molecular plateaus carrying regular conductance fluctuation under non-linear ramp mechanical modulations. These fluctuations in conductance is often trivial in terms of time-scale and therefore only add to the background or noise in the 1D conductance histogram. To plumb the important information hidden in the fluctuated molecular plateaus, I have also used the recently developed correlation analysis in my dissertation research.

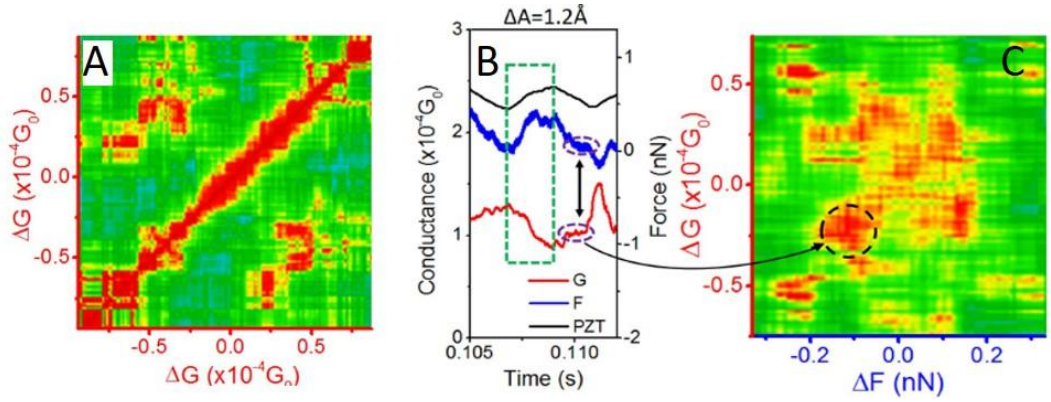

Figure 2.4 Correlation analysis. (A) Example conductance 2D auto-correlation histogram (C-2DACH). (B) Simultaneously recorded PZT, force (F) and conductance (G) signal of a single-

molecule junction. (C) Example force-conductance 2D cross-correlation histogram (FC-2DCCH). Reprinted with permission from ref. 59. Copyright (2014) American Chemical Society.

In order to unravel the relationship between specific signals in individual conductance traces, such as the relation between two conductance (force) values, a conductance (force) 2D auto-correlation histogram (C(F)-2DACH) which was recently developed by Makk et al.[57] is adopted. The 2DACH is in a class of single variable time series analysis, but is the basis of deriving multivariate analysis.[58]

When a pair of force and conductance traces are recorded, the Labview program reads the data in the order of bins. In order to correlate a conductance trace to its corresponding force trace and other traces in the data sets, data points of a trace are separated by a certain bin size. This allows comparing the conductance characteristics at a certain bin with the simultaneously measured force signal at the same bin and other bins along the entire trace. Auto-correlation A_g calculates the scaled covariance between two elements: (1) bin i of one trace histogram $g_i(l)$ compared with the mean $g_i(l)_l$ of bin i from all the trace histograms and (2) bin j of the same sample $g_j(l)$ compared with the mean $g_j(l)_l$ of bin j from all the traces. Usually i and j represent moments in time where j is a time lagged behind (or before when the lag is negative). Then the degree with which the signal and its offset are linearly dependent is calculated. The calculation equation is shown as

$$A_g(i,j) = \frac{\langle [g_i(l) - \langle g_i(l) \rangle][g_j(l) - \langle g_j(l) \rangle] \rangle_l}{\sqrt{\langle [g_i(l) - \langle g_i(l) \rangle]^2 \rangle_l \langle [g_j(l) - \langle g_j(l) \rangle]^2 \rangle_l}} \quad (2.1)$$

By adding another variable, the calculation evolves through an intermediate correlation

which does not have a lag, so it is not beneficial to plot in a 2D grid, as detailed in a recent study.[58] Cross-correlation $C_{g,f}$ reproduces the lag from auto-correlation into correlation for two variables using eqn. (2.2)

$$C_{g,f}(i,j) = \frac{\langle [g_i(l) - \langle g_i(l) \rangle][f_j(l) - \langle f_j(l) \rangle] \rangle_l}{\sqrt{\langle [g_i(l) - \langle g_i(l) \rangle]^2 \rangle_l \langle [f_j(l) - \langle f_j(l) \rangle]^2 \rangle_l}} \quad (2.2)$$

Specifically, **Eqn. (2.2)** calculates the cross-correlation between two variables, conductance and force, with the second variable offset by incrementing lag as with auto-correlation.

The calculation algorithm of **Eqn. (2.1)** for auto-correlation and **Eqn. (2.2)** for cross-correlation is set up into the Labview program. When hundreds of pairs of simultaneously measured conductance and force traces are read by the Labview program, it plots the statistical results of the calculation in a 2D grid.

Using auto-correlation method, correlation between difference conductance (force) values can be plotted in a color-binned 2D map with a degree of correlation ranging from -1 to 1. Example conductance(C)-2DACH plot is shown in **Figure 2.4A**. The strong correlated regions in a 2DACH reflect where two correlated conductance values often appear together.

To explore the correlation between two variables, especially the correlation between simultaneously measured force and conductance, Hamill et al. recently expanded the auto-correlation to a cross-correlation by adding another variable, force, to the calculations.[58, 59] Using this method, a force-conductance 2D cross-correlation analysis histogram (FC-2DCCH) can be constructed. FC-2DCCH reveals regions where a force value and a conductance value are closely related to each other. Namely, FC-2DCCH

analysis helps to bridge the mechanical properties of a single-molecule junction with its charge transport properties. For example, as shown in **Figure 2.4 C**, the FC-2DCCH shows strong correlated regions that correspond to small plateaus that appear in both force and conductance traces simultaneously.

CHAPTER 3

CONTACT EFFECT IN AU-OCTANEDITHIOL-AU SINGLE MOLECULE JUNCTIONS

- [59] K. Wang, J. Hamill, J. Zhou, B.Q. Xu, J. Am. Chem. Soc., 2014, 136, 17406–17409. Reprinted here with permission of publisher.
- [60] K. Wang, B.Q. Xu, Phys. Chem. Chem. Phys., 2016, 18, 9569-9576. Reprinted here with permission of publisher.

3.1 Mapping Contact Effect by Force-Conductance Cross-Correlation

3.1.1 Abstract

We have measured the force and conductance of Au-octanedithiol-Au junctions using a modified conducting atomic force microscopy break junction technique with sawtooth modulations. Force−conductance two-dimensional cross-correlation histogram (FC-2DCCH) analysis for the single-molecule plateaus is demonstrated. Interestingly, four strong correlated regions appear in FC-2DCCHs consistently when modulations with different amplitudes are applied, in sharp contrast to the results under no modulation. These regions reflect the conductance and force changes during the transition of two molecule/electrode contact configurations. As the modulation amplitude increases, intermediate transition states of the contact configurations are discerned and further confirmed by comparing individual traces. This study unravels the relation between force and conductance hidden in the data of a modulated single-molecule break junction system and provides a fresh understanding of electron transport properties at molecule/electrode interfaces.

3.1.2 Introduction

The single-molecule break junction (SMBJ) technique has been performed as a reliable experimental platform, creating electrode-molecule-electrode structures.[4, 8, 31, 34, 61, 62] Studies using SMBJ focus on the charge transport properties, namely, the conductance, of molecular junctions.[31, 63-65] Precise control of the atomic structure, however, is not well achieved. Large fluctuations in the conductance measurements of alkane molecules have been puzzling and are not yet fully understood.[17, 34] For instance, a

Au-octanedithiol (C8DT)-Au junction was measured to have >1 order difference in conductance.[66-69] Such uncertainty in conductance has also been observed for other molecules in the alkane family.[66, 67, 69] Theoretical simulations proposed the variation at the molecule/electrode contact interfaces as the cause for the broad distribution in conductance.[4, 67, 70-72] Equally important is that a series of changes in contact configurations along the evolution of a single molecule junction prior to rupture could also induce significant conductance change, especially for Au-thiol (Au-S) contact.[73-75] Thus, to incorporate science derived from a SMBJ, a better understanding of the molecule/electrode interfaces is key.

Sawtooth modulation of piezo transducer (PZT) movement on a stabilized molecular junction has been proven to be able to isolate the contact parts for detailed study, and individual traces measured under such modulation show a close kinship between force and conductance.[76, 77] However, conventional 1D and 2D histograms are not ideal tools to discover significant information from these modulated traces, and the lack of a proper method to interpret the modulated data hinders the physical understanding of contact effect.[76] Recent applications of correlation analysis on conductance traces showed more detailed features beyond conventional histograms and provided a new understanding of molecular junctions.[57, 78, 79] A more recent promotion of the correlation analysis involved a multivariate time series analysis by adding a second, variable force to the analysis and allowed the cross-correlation of force and conductance.[58, 80] This newly emerging analysis offers the possibility to connect force plateaus with conductance plateaus measured in unison, and has discerned miniature yet significant relations between force and conductance hidden in the data.[58] Therefore, it is

expected that a force-conductance two-dimensional cross-correlation histogram (FC-2DCCH) could unravel the hidden yet important subtleties in the sawtooth modulated data and further extend our knowledge of the role of contact interface in a molecular junction.

Here we measure the conductance and force of Au-C8DT-Au junctions under sawtooth modulations (**Figure 3.1A**) and demonstrate FC-2DCCHs for the modulated single-molecule plateaus. Three modulation amplitudes (ΔA= 0.8, 1.0, and 1.2 Å) are tested, and the data set collected under no modulation is also studied for comparison. The resulting FC-2DCCHs show strongly correlated regions of force and conductance for all three modulation amplitudes, which sharply contrasts with non-modulated data. The evolution of FC-2DCCHs with increasing modulation amplitude for the first time distinguishes the subtle intermediate states of contact configurations. This work adds another dimension to the conventional statistical methods and provides critical hints for further theoretical simulations.

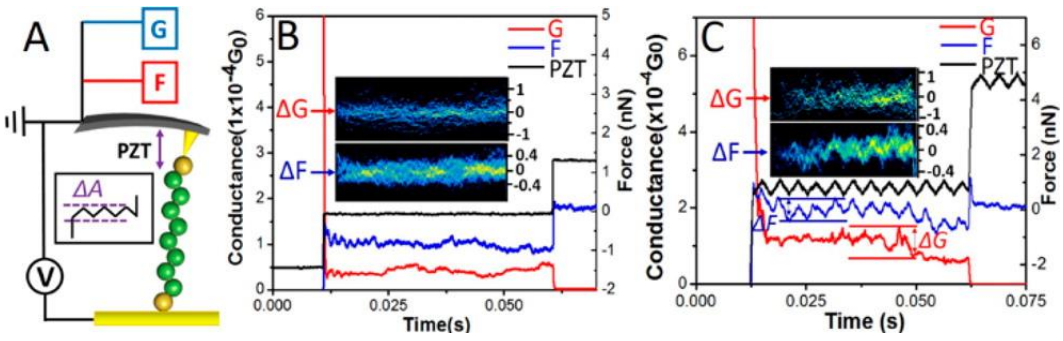

Figure 3.1 (A) Schematic of the modified conducting atomic force microscopy break junction technique and the sawtooth mechanical modulation signal (black box). In the C8DT molecule, carbon atoms and thiol groups are shown in dark green and dark yellow spheres, respectively. Examples of individual traces without modulation (B) and under modulation ΔA= 0.8 Å (C). The inset in B shows the overlay of 67 non-modulated conductance and force traces. The inset in C

shows the overlay of 60 modulated conductance and force traces. The units of the insets in B and C are $1\times10^{-4}G_0$ for conductance and 1 nN for force. Reprinted with permission from ref. 59. Copyright (2014) American Chemical Society.

3.1.3 Experimental Details

Chemicals and materials preparation 1,8-octanedithiol(C8DT) were purchased from Aldrich. C8DT molecule was chosen because of its simple yet rigid structure and because it was well studied experimentally and theoretically. This makes C8DT a good candidate for investigating the contact effect in molecular junctions. Au (111) substrate was prepared by annealing Au surface in a hydrogen flame immediately before immersion in sample solutions. C8DT self-assembly monolayers were formed on the Au (111) substrate when 1mM C8DT deionized (DI) water solution was dropped on the substrate and incubated for 3hrs. The Au substrate was then rinsed with deionized water for three times and put in pure toluene solution after being dried with argon. After these treatments, the sample was used for CAFM-BJ measurements.

Experimental setup The SPM system is the Picoplus SPM (Molecular Imaging) with a Pico Scan 3000 Controller (Molecular Imaging). The CAFM tip was made of Si coated with a 15 nm layer of chromium and then a 35 nm layer of gold (99.999%) using an ion beam coater (Gatan model 681). The spring constant of the AFM cantilever was 40 N/m. The modified CAFMBJ and modulations are realized by controlling the movement of the piezo transducer (PZT), and experimental data was acquired and processed using a homemade Labview programs.[56, 77] In contrast with conventional SPM-BJ technique, we divided the tip retracting process into two segments: continuous stretching and free-holding. After abruptly stretching for 1nm, the molecular junctions are kept free-holding.

Modulations of a "saw-tooth" PZT signal (240Hz) were applied on the free-holding process to regulate the separation between the tip and substrate. This modulation signal adjusts the separation by a periodic cycle of elongation and compression of PZT movement. Three different modulation amplitudes ΔA (0.8, 1.0, and 1.2 Å) were tested in this study. These three modulation amplitudes were chosen because they have been proven to be large enough to perturb the contact configuration but still maintain the junction intact.[76, 77] All the measurements were performed under a bias voltage of 0.3V at room temperature (298K).

3.1.4 Results and Discussions

We use the modified CAFM-BJ technique to measure the force and conductance in parallel.[56] This technique involves a periodic freeholding process while the AFM tip is retracted away from the substrate.[56] The free-holding process stabilizes a junction and greatly minimizes its dynamic movement. In our study, the freeholding is set to occur after every retraction of 1 nm. With the lifetime of the junction extended by the free-holding, proper mechanical modulations can be carried out without hurting the integrity of a junction.[77] As shown in **Figure 3.1A**, the sawtooth modulation manipulates the tip/substrate separation by cycling an elongation followed by a compression at a frequency of 240Hz, while the junction is free-held. This ensures that the changes in conductance and force are predominantly caused by the mechanical modulation instead of the dynamic fluctuation of the junction. The modulation manipulates the softest part of the junction. In our system, C8DT molecules can be regarded as a rigid body since the C-C bond is much stronger than the S-Au and Au-Au bonds at the contacts.[69, 81] Thus, the

softest part in our system is the molecule/electrode contacts, which should be the source of most changes induced by the modulations. Typical non-modulated and modulated traces are shown in **Figure 3.1B, C**. We see that the force and conductance traces without modulation reveal no obvious feature other than slight variations attributed to the thermal vibration of the junctions.[81] Traces measured under a modulation show regular force fluctuation in accordance with the PZT signal and conductance fluctuations in opposite phase to the PZT signal. This phenomenon is consistent with a previous report,[77] and it is easy to understand that conductance decreases during the increase of PZT signal from the valley to the peak, which extends the junction distance and lowers the efficiency of electron transport.[82] We also notice that modulation does not necessarily induce a conductance change.

We first analyze the data sets by plotting conductance (force) 1D and conductance (force) vs time 2D histograms. Simultaneously measured conductance and force traces with significant features are selected for the data analysis. The conductance 1D histogram for the non-modulated data shows two pronounced peaks at around $2.5\times10^{-4}G_0$ and $0.5\times10^{-4}G_0$ which coincide with the two major bands (blue arrows) in the conductance vs time 2D plot. These two conductance values match well with previously reported high and medium conductance sets for Au-C8DT-Au junction.[66, 67] We ascribe those single-molecule conductance values lower than these two but previously reported to be less populated in our data. The force 1D histogram reveals a dominant peak at around 1.5nN, which matches the rupture force of the junction via Au-Au breaking.[31, 78, 83] The successful determination of different conductance sets and the junction rupture force rationalizes our trace selecting method. Under modulation ΔA= 0.8 Å, both conductance

(force) 1D and 2D histograms reveal no distinguishable detail. This indicates that the1D and 2D histograms wash out the significant features in the modulated data and fail to zoom into the miniatures.

As the SMBJ system was initially built to study single-molecule properties, data analysis approaches to interpret the most repeated features and statistically significant information measured while a single molecule is sandwiched between the electrodes are necessary. To downscale the analysis to single molecule level, we clip the traces to single-molecule plateaus by excluding those conductance traces without a plateau within the single-molecule conductance range. We then focus on the fluctuation signals (ΔG and ΔF) induced by the mechanical modulations on these single molecule plateaus. Each single-molecule plateau is offset to zero by subtracting the average value of the plateau, and correlation analysis using many such plateaus could reveal statistically significant information downscaled to the single-molecule level (see the insets of **Figure 3.1B and C**).

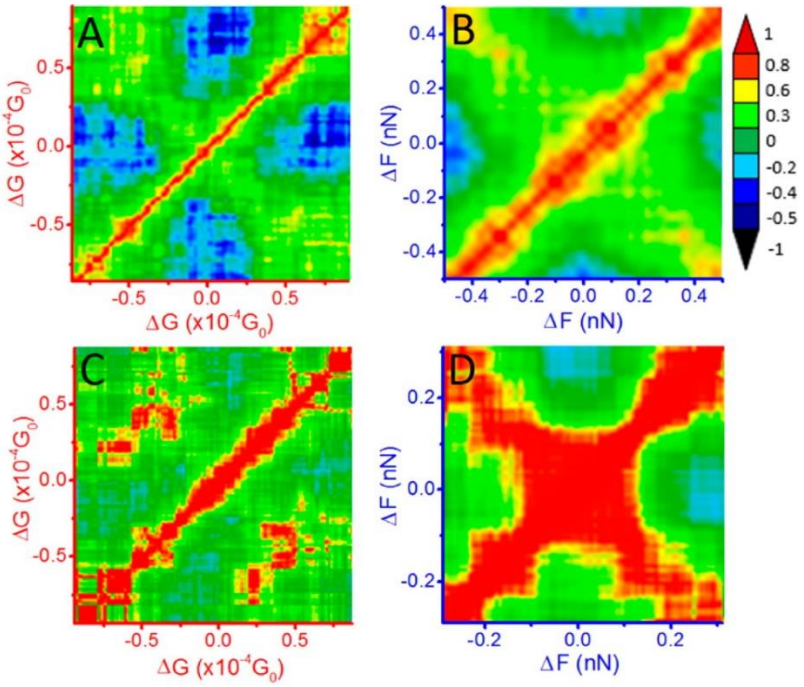

Figure 3.2 Two-dimensional autocorrelation histogram (2DACH) for non-modulated data (67 traces) and modulated data (ΔA = 1.2 Å, 69 traces). A and B show the C- and F 2DACH for non-modulated plateaus, respectively. C and D show the C- and F-2DACH for modulated plateaus (ΔA= 1.2 Å), respectively. The color bar is the same for all the panels. Reprinted with permission from ref. 59. Copyright (2014) American Chemical Society.

We present the two-dimensional autocorrelation histogram (2DACH) analysis for force (F) and conductance (C) to explore the relation between two ΔG's or ΔF's. By interpreting a single trace in terms of bins, 2DACH essentially describes the correlation degree of data points taken at every bin location. Bin sizes are $2\times10^{-6}G_0$ for conductance and 0.01 nN for force. The correlation degree ranges from −1 to 1 and is plotted in color code (**Figure 3.2**). We observe strongly correlated regions distributed along the diagonal line (from bottom left to top right) in each panel of **Figure 3.2**. This diagonal line reflects the degree to which a signal correlates to itself, which is supposed to be 1.[57, 78] Under no modulation, both C- and F-2DACH show four anti-correlated regions (blue regions), which indicate a rather low possibility of two ΔG's or ΔF's appearing together on the plateaus. These regions relate to where $\Delta G=0G_0$ correlates with the $\Delta G\approx\pm0.3\times10^{-4}G_0$, and where $\Delta F=0G_0$ anti-correlates with $\Delta F\approx\pm0.35$nN, and spread far and wide away from the center. We attribute this phenomenon to the few data points beyond $\Delta G=\pm 0.3\times10^{-4}G_0$ and ΔF of ±0.35nN. Overall, 2DACHs reveal no obvious strong correlated region for non-modulated plateaus. In contrast, under the modulation of ΔA=1.2Å, noticeable features in the C-2DACH are the strong correlated regions (red) locating at $(0.48\times10^{-4}G_0,\ -0.49\times10^{-4}G_0)$. This specifies that the increase in conductance by

$0.48\times10^{-4}G_0$ usually emerged with a concurrent conductance decrease by $0.49\times10^{-4}G_0$. It is possible that these two values correspond to two different contact configurations, which frequently took place on the same plateau. Given this effect, we believe the possible change in contact configuration is predominantly induced by the mechanical modulations. Interestingly, the F-2DACH for modulated data shows another strong correlated diagonal line. Similar phenomena are seen for other modulation amplitudes as well. This newly emerged diagonal line suggests a linear relation that a certain amount of increase in force usually correlated with a force decrease by the same amount on the identical plateau. Since the selected force traces always show linear and regular sawtooth patterns, the average behavior of many such force traces should illustrate a similar degree of increase and decrease at a plateau, and the increase and decrease always correlate with each other. Thus, it is reasonable that F-2DACH produces another diagonal line. This autocorrelation analysis of the modulated data has revealed new details never observed before. Unfortunately, it still fails to bridge the force change with conductance change induced by the mechanical modulations.

The core interest of this study lies in the relationship between a ΔG and a ΔF caused by the introduction of mechanical modulations. FC-2DCCH analysis serves as a powerful tool to achieve this goal by calculating the correlation degree between a force signal and the corresponding conductance signal. The same sample traces and bin sizes adopted in 2DACH are also used for FC-2DCCH. We plot the FC-2DCCHs for all data sets in **Figure 3.3**. For non-modulated plateaus, the FC-2DCCH shows neither strong nor anti-correlation areas, but some weakly correlated regions dispersed around the center within a range of $\pm0.25\times10^{-4}G_0$ in conductance and $\pm$0.3 nN in force (yellow in **Figure**

3.3A). These fluctuations in conductance and force match well with the fluctuations reported in previous measurements.[77] Noting that the junction was free-held while being measured, this fluctuation is not caused by the change of junction separation but by the thermal vibration of the molecule or possible relaxation of the Au-S binding site at a constant junction distance of 1 nm.[77, 84] Simulations have suggested that thermal motion of a junction can cause the significant conductance change.[73, 81, 85]

However, FC-2DCCH plots show dramatic changes for the modulated plateaus. Multiple strongly correlated regions (red) can be seen. Interestingly, four specific regions (solid circles) appear consistently for all modulation amplitudes. At modulation ΔA= 0.8 Å, the four regions locate at ~ ($\pm 0.48\times10^{-4}G_0$, $\pm$0.18nN). They slightly increase to ~ ($\pm 0.55\times10^{-4}G_0$, $\pm$0.26 nN) as the modulation amplitude rises to 1.2 Å. The slight change in conductance with increasing modulation amplitude is consistent with a previous report, which suggested that the increase of modulation amplitude from 0.8 to 1.2 Å would not change the conductance much.[76] Thus, we believe the increase of ΔA from 0.8 to 1.2 Å has little impact on relevant contact configurations but linearly increases the force. The conductance values of these four regions also coincide with those observed in C-2DACH (**Figure 3.2C**). Counterintuitively, a positive force at ~0.2 nN strongly correlates with both positive and negative conductance. The reason is similar to that for the second diagonal line in **Figure 3.2D**. A positive ΔF caused by the elongation of the junction induces a conductance decrease, namely a negative ΔG in a FC-2DCCH. However, on the identical plateau, the sawtooth pattern force signal could always occur with both a conductance increase and decrease. A positive force may correlate with any signals, including conductance increase and decrease, that most often occurred with it. Therefore,

these correlated regions should distribute in a centrosymmetric manner, as the FC-2DCCHs show. So, the key lies in the net amplitude of ΔG and ΔF instead of their signs. Another interesting feature is that the strong correlated spots related with negative ΔF's usually have a higher intensity than those correlating to positive ΔF's, indicating a stronger correlation between force and conductance when the junction is "compressed". It is necessary to note that the compression effect mainly comes from the molecular angle changes caused by system drifts and contact Au atom motion.[86] We suggest the changes from $\sim 0.5\times10^{-4}G_0$ to $-0.5\times10^{-4}G_0$ in conductance and from −0.2 to 0.2 nN in force are related to the switch between two junction conformations which could differentiate in Au-S bonding site, junction length, or molecular angle. Given the little conductance change with increasing modulation amplitude, we believe this switch is independent of modulation amplitudes used in our experiments. Au-S bonding configuration has been reported to be able to alternate among different configurations with the length change of the molecular junction.[67, 70, 72] A simulation study[73] highly resembling our system illustrated a possible Au-S contact configuration change with a molecular angle tilt. We believe that this force-induced change in conductance could be due to the change in the coupling energy between thiol and Au. Such coupling energy change will induce a small change in the conductance value, as shown in the 2DCCHs. However, if a large coupling energy change is induced by a large enough force, the transition from one configuration to another configuration could occur.

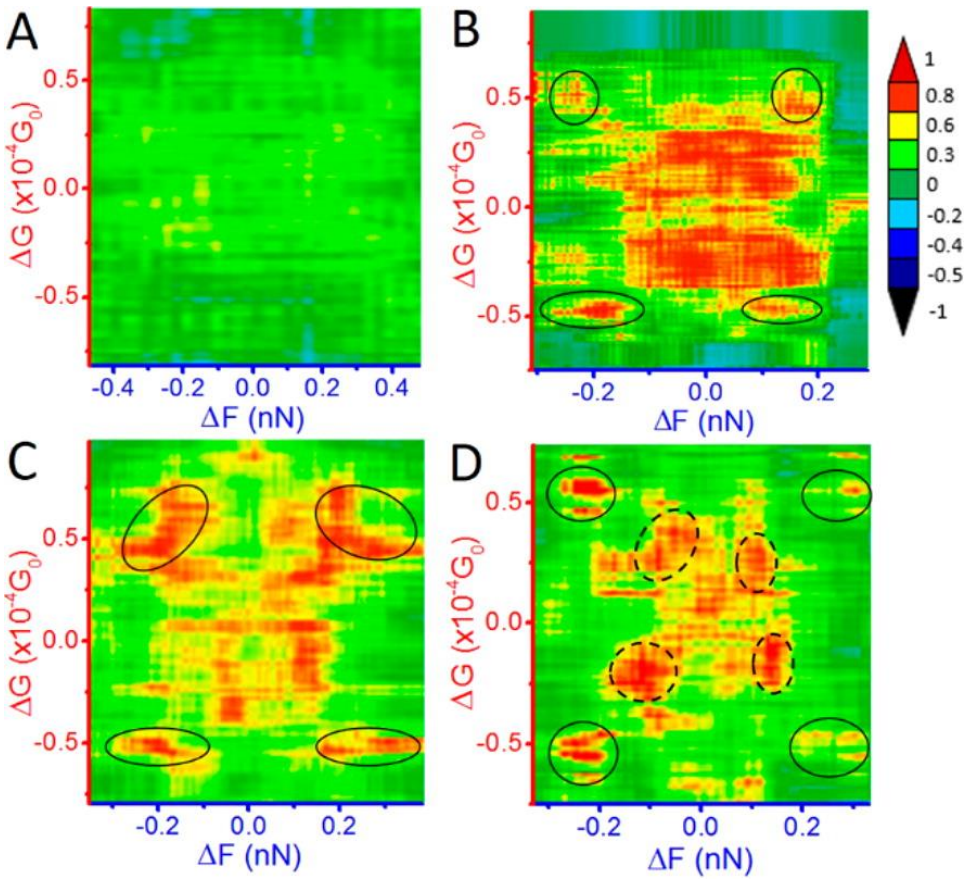

Figure 3.3 Force−conductance two-dimensional cross-correlation histogram (FC-2DCCH) for non-modulated data (A, 67 traces) and modulated data (B, ΔA= 0.8 Å, 60 traces; C, ΔA= 1.0 Å, 76 traces; D, ΔA= 1.2 Å, 69 traces). Reprinted with permission from ref. 59. Copyright (2014) American Chemical Society.

Noticeable strongly correlated regions distributed around the center show obvious shape changes, from scattered blurred area for ΔA= 0.8 Å to distinct spots for ΔA= 1.2 Å. It has to be noted that the scattered center correlation areas for the modulated data are mainly caused by the mechanical modulation, which contrasts with the weak correlated areas also spreading around the center in the non-modulated case. The discrete regions (dashed circles in **Figure 3.3D**) correspond to a smaller force and conductance change

than the solid circled regions. We suggest that these discrete regions are related to intermediate states through which the junction evolves. In **Figure 3.4**, a careful check of detailed features in individual plateaus under ΔA= 0.8 and 1.2 Å reveals an exponential increase (decrease) in conductance with the decrease (increase) of junction separation, suggesting a change in tunneling barrier length. Given there is no increase in the number of carbon unit of the molecule, this change is essentially contributed by the extra barrier originating from contact interfaces. More importantly, under ΔA= 1.2 Å, we see minor plateaus of both force and conductance (purple dashed circles), which generate strongly correlated regions in FC-2DCCH. This effect occurs for ΔA= 1.2 Å more often, which confirms the existence of the intermediate states and also implies they are more stabilized under ΔA= 1.2 Å. It is noteworthy that some strongly correlated regions that deviated from the regions discussed above are not clear to us yet, and further investigation is needed.

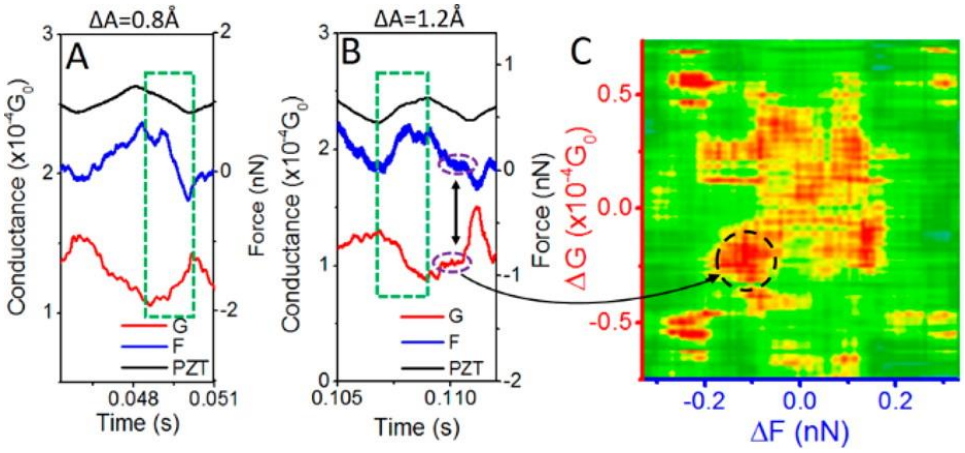

Figure 3.4 (A, B) Representative zoom-in signal (green dashed square) for ΔA= 0.8 and 1.2 Å, respectively. (C) FC-2DCCH for ΔA= 1.2 Å. In B, the purple dashed circles represent the intermediate force and conductance plateaus which could form the region in the black dashed

circle in C. Reprinted with permission from ref. 59. Copyright (2014) American Chemical Society.

3.1.5 Conclusion

In conclusion, we have measured the force and conductance of Au-C8DT-Au junction using the modified CAFMBJ under sawtooth modulations, and FC-2DCCHs for single-molecule plateaus were demonstrated. The FC-2DCCHs yielded intriguing features: specific changes in conductance closely correlated with force changes induced by the contact configuration switch. Intermediate stabilized junction states during the switch were also discerned. These features were hidden in the data when analyzed by conventional 1D and 2D histogram methods. This work thus for the first time maps the relation between conductance and force involved in a contact configuration transition. We believe that refined experimental controls along with the multivariate data analysis approach can bring us more latent yet significant details in single-molecule junctions.

3.2 Experimental Determination and a Practical Barrier Model for Electron Tunneling through Contact Interfaces

3.2.1 Abstract

An advanced understanding of the molecule–electrode contact interfaces of single-molecule junctions is a necessity for real world application of future single-molecule devices. This study aims to elucidate the change in the contact tunneling barrier induced by junction extension and how this change affects the resulting junction conductance. The contact barrier of Au–octanedithiol/octanediamine–Au junctions was studied under triangle (TRI) mechanical modulations using the modified scanning

tunneling microscopy (STM) break junction technique. The experimental results reveal that as the junction separation extends, the contact barrier of octanedithiol follows a unique trend, a linear increase followed by a plateau in barrier height, which is in contrast to that of octanediamine, a nearly rectangle barrier. We propose a modified contact barrier model for the unique barrier shape of octanedithiol, based on which the calculation agrees well with the experimental data. This study shows unprecedented experimental features of the molecule–electrode contact barrier of single-molecule junctions and provides new insights into the nature of contact effect in determining electron transport through single-molecule junctions.

3.2.2 Introduction

Despite the continued progress in molecular electronics over the past few decades, the desired application of molecular-scale electronic devices requires significant advances in our understanding of charge transport through a single-molecule junction system, the building block towards an electronic component using an individual molecule as a functional unit.[2, 8, 62] In a single-molecule junction, the structure of an individual molecule contacting two metallic electrodes, probably the most elusive factor that influences the charge transport properties of a molecular junction lies in the molecule–electrode contact interfaces.[4, 87] The physical nature of the molecule–electrode interface in terms of electron transport is an additional tunneling barrier apart from the tunneling barrier formed by the molecular core. Therefore, changes in contact configurations essentially make contribution to the molecule–electrode coupling, namely the contact tunneling barrier. To understand the impact of the contact interface effect, given the

difficulty in the precise experimental control of junction conformations, theoretical simulations have been used to assume possible contact geometries and atomic bonding configurations, and to explore how they determine the current through a junction.[67, 70-72] These studies have highlighted the considerable contribution from molecule–electrode interfaces, especially for N-alkanedithiol junctions. Multiple contact configurations have been theoretically proposed to be responsible for different single-molecule conductance sets of alkanedithiol molecules, and molecular dynamic simulations have shown a clear transition among different contact configurations during junction stretching.[70, 73] This fact necessitates more detailed experimental investigation and deeper insight into the role of contacts of alkanedithiol molecular junctions, particularly how it contributes to junction conductance under junction extension.

Considering the relative low bias (<1 V) applied in real conductance measurements with respect to the rather large HOMO–LUMO gap (>5 eV) of alkane molecules, the dominant charge transport mechanism in alkanedithiol junctions follows coherent and non-resonant tunneling.[88] For such a case, a rectangular-shaped tunneling barrier where conductance decays exponentially with the barrier length (here the length of molecular core) has been suggested.[89-91] The transmission coefficient T_{mol} of the molecular core can then be put as[92, 93]

$$T_{mol} = exp(-\beta_{mol} L_{mol}) = exp\left(-1.025 L_{mol}\sqrt{\emptyset_{mol}}\right), \quad (3.1)$$

where β_{mol}, $\emptyset_{mol}$, and L_{mol} represent the decay constant, tunneling barrier height and barrier length of the molecular core, respectively. Based on the Landauer–Buttiker formalism and taking the contribution of contacts into consideration, the overall conductance of a molecular junction can be written as[94]

$$G = \left(\frac{2e^2}{h}\right) T_{mol} \times T_C \quad (3.2)$$

Note that T_C represents the overall transmission coefficient contributed by both the left contact and the right contact.

Using a modified scanning tunneling microscopy (STM) break junction technique, a mechanical modulation on a stabilized molecular junction can manipulate the junction conformation and hence tune the resulting junction conductance in a certain manner.[6, 59, 77] More importantly, critical parameters, such as the contact decay constant β_C, can be obtained by fitting the experimental data to proposed theoretical models.[92, 93] This offers us a chance to study the contact effect while single-molecule conductance varies with junction extension.

In this work, we study the contact tunneling barrier of 1,8-octanedithiol (C8DT) in the Au–molecule–Au junction system using a modified STM break junction technique which is detailed elsewhere (**Figure 3.5A**).[31, 56] 1,8-Octanediamine (C8DA) and 1,6-hexanedithol (C6DT) were also measured as complementary tests. Triangle (TRI) modulation with different modulation amplitudes was applied onto free-held single-molecule junctions to regulate junction separation. The experimental results showed that as the junction extended, the contact tunneling barrier of C8DT molecular junctions followed a unique trend which contrasts with the nearly rectangle barrier that C8DA followed. We introduce a modified contact tunneling barrier model to describe the observed phenomena of the C8DT junction. Theoretical calculations based on this modified model agree well with the experimental data. This work demonstrates the direct experimental evidence of the contact tunneling barrier of octanedithiol molecular

junctions, and provides new insights into the role of molecule–electrode interfaces in a single-molecule junction system.

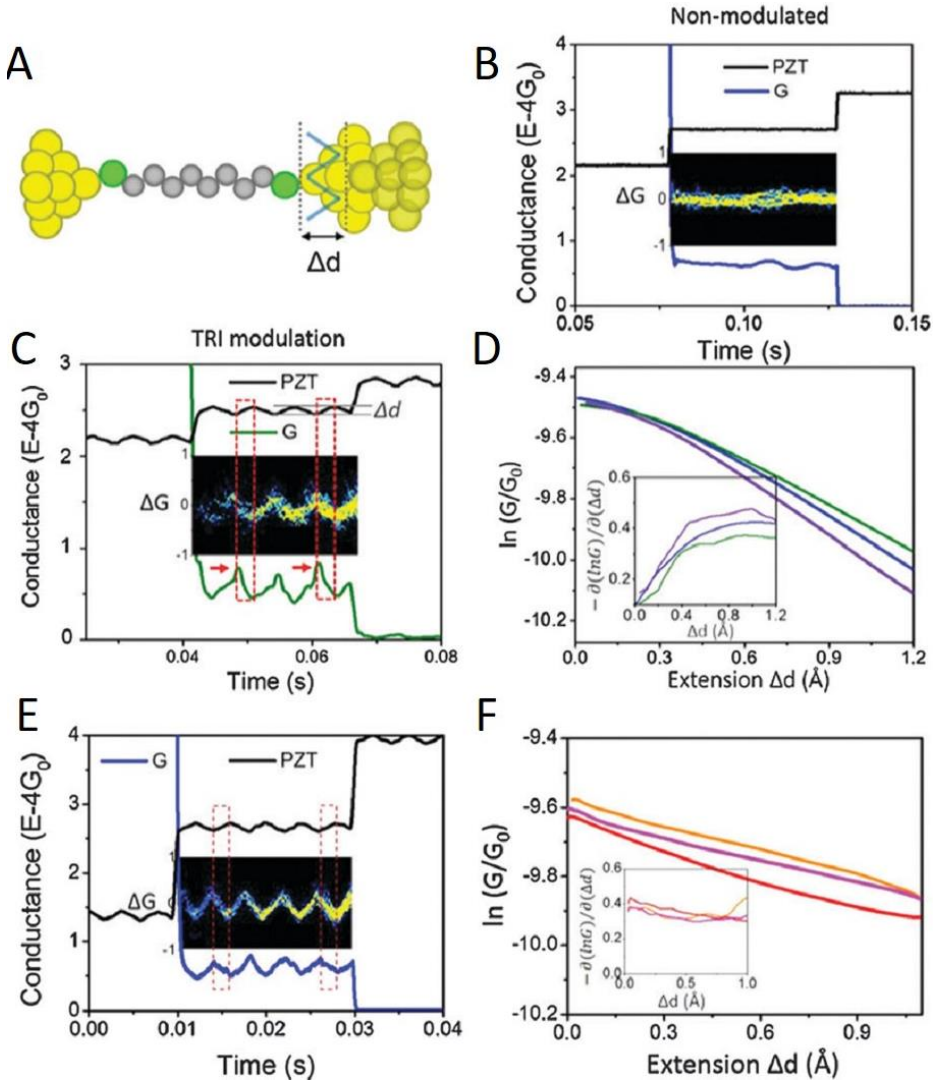

Figure 3.5 (A) Schematic illustration of TRI modulation used in this work. (B) Example of conductance trace (blue) and PZT movement (black) for a stretch-hold plateau without modulation. The inset displays the overlay of around 70 single-molecule conductance plateaus. (C) Example of conductance trace (green) and a PZT movement signal (black) of a C8DT stretch-hold plateau with a triangle modulation (Δd = 1.2 Å). The inset displays the overlay of 70 single-molecule conductance plateaus. The red dash-squared region represents a typical conductance decrease caused by junction extension. Note that the red arrow labels the G_{mol} value prior to

junction extension, which was induced by TRI modulation. (D) Example of $lnG\ vs\ \Delta d$ curves for the conductance decrease regions and the corresponding contact decay constant $\beta_C\ vs\ \Delta d$ curves (inset) derived using eqn. (3.3). (e) Example of conductance trace (blue) and a PZT movement signal (black) of a C8DA stretch-hold plateau with a triangle modulation (Δd = 1.2 Å). The inset displays the overlay of 82 single-molecule conductance plateaus. Note that in (B), (C) and (E) insets, the Δd is in unit of $10^{-4}G_0$. The vertical unit of the (D) and (F) inset is $Å^{-1}$. Reprinted from ref. 60.

3.2.3. Experimental Details

Chemicals and sample preparation 1,8-Octanedithiol (C8DT), 1.8-octanediamine (C8DA) and 1,6-hexanedithiol (C6DT) were purchased from Sigma Aldrich. Au substrates were prepared by evaporating B100 nm of gold onto freshly cleaved mica sheets using an evaporator under a vacuum of 10^{-7} Torr. The Gold beads for Au substrate deposition were from Kurt J. Lesker company (99.999%), and mica sheet was from Ted Pella, Inc. The surface of the Au substrate was annealed by hydrogen flame just before immersion in sample solutions containing target molecules. This annealing step cleaned the surface and allowed epitaxial reconstruction of the Au to form large terraces of Au(111). Au surfaces were annealed in a hydrogen flame to clean the surface and allow epitaxial reconstruction of the Au to form large terraces of Au(111) immediately before immersion in sample molecule solution. The self-assembly monolayer of the sample molecule was formed on the Au(111) substrate when 1 mM molecule deionized (DI) water solution was dropped on the substrate and incubated for 3 h. The Au substrate was then rinsed with deionized water for three times and put in pure toluene solution after

drying with argon gas. After these treatments, the sample was immediately used to perform STM break junction measurements.

Electrical measurement setup The STM system is the Picoplus SPM (Molecular Imaging) with a Pico Scan 3000 Controller (Molecular Imaging). The modified STM break junction technique and TRI modulations are realized by controlling the movement of the piezo transducer (PZT) in a stretch-hold mode. In this technique, we divided the tip retracting process into two segments: abrupt stretching and free holding. After abruptly stretching for a certain distance (0.6 nm for C8DT/C8DA and 0.8 nm for C6DT), the molecular junctions are kept free holding. This stretch-hold process was repeated until electrode separation reached 20 nm where no molecule was sandwiched in the junction. The free-holding process greatly minimized the fluctuations of contact conformations caused by continuous tip retracting and extended the lifetime of the junctions. It also allows further modulations to be applied. A triangle-shaped modulation of PZT movement was applied on the free-held plateaus to regulate the separation between the tip and the substrate. Three modulation amplitudes (Δd = 0.6 Å, 1.2 Å and 1.5 Å) were chosen for C8DT because they were tested to be large enough to perturb the contacts but still maintain the integrity of the junction. Modulation amplitudes of Δd = 1.2Å and 0.8Å were used for C8DA and C6DT, respectively. The experimental data were acquired and processed using a homemade Labview program. All conductance measurements in this study were performed under a bias voltage of 0.3 V, which was applied on the substrate with the STM tip grounded

3.2.4 Results and Discussions

In this study, the applied TRI modulation essentially regulates junction separation in a manner of periodic elongation followed by compression (black line in **Figure 3.5C**). We emphasize that TRI modulation mainly manipulates the softest part of a molecular junction.[59] In a Au–C8DT/C8DA/C6DT–Au junction, the softest part has been suggested to be the molecule–electrode contacts since the intramolecular C–C bond is much stronger than the thiol–Au, amine–Au bond or the Au–Au bond at the contact interfaces.[59, 77] For the junction systems studied in this paper, we define the combination of the carbon chain-anchoring group bond and the anchoring group-electrode bond in its entirety as molecule–electrode interfaces. From a mechanical point of view, a recent work also confirmed that under junction separation fluctuation, the strain mostly comes from the molecule–electrode interfaces in alkane molecular junctions.[95] Thus, the conductance change caused by the applied TRI modulation should mostly come from molecule–electrode contacts.[59] It is worth noting that four sets of C8DT/C8DA single-molecule conductance have been observed in previous stretch-hold mode conductance measurements.[56] In this work, under each modulation amplitude, we only focus on conductance groups with highest appearance probabilities, namely, the single-molecule conductance plateaus possessing a conductance value (typically considered 'medium' conductance) within the range of $5\sim10\times10^{-5}G_0$ for C8DT and $2.5\sim5\times10^{-5}G_0$ for C8DA.[56] This is because the most probable conductance groups usually possess the most dominant molecular junction configurations and therefore have greater statistical significance. Using the home-made Labview program, the average conductance value of a modulated plateau (as those shown in green in **Figure 3.5C and E**) was calculated, and those within

the defined range of most probable single-molecule conductance were selected as sample single-molecule conductance plateaus. It is necessary to note that for C8DT and C8DA, the single-molecule plateau of most conductance traces occurred when the tip finished the second abrupt stretching from the substrate, creating a junction separation of ~1.2 nm. The abrupt stretching of 0.8nm, about the full length of the hexane (C6) molecule, was adopted for C6DT, where the single-molecule plateau occurred after one abrupt stretching. Under this experimental setup, junction separation is around the full length of the sample molecule, suggesting that the molecules mostly possessed an orientation perpendicular to the substrate surface when the TRI mechanical modulations were applied. This setup greatly diminished the influence of conductance change caused by molecular angle tilting with respect to the substrate and also ruled out the impact of gauge effect, leaving the conductance change mainly due to the variation of the molecule–electrode interface.[73]

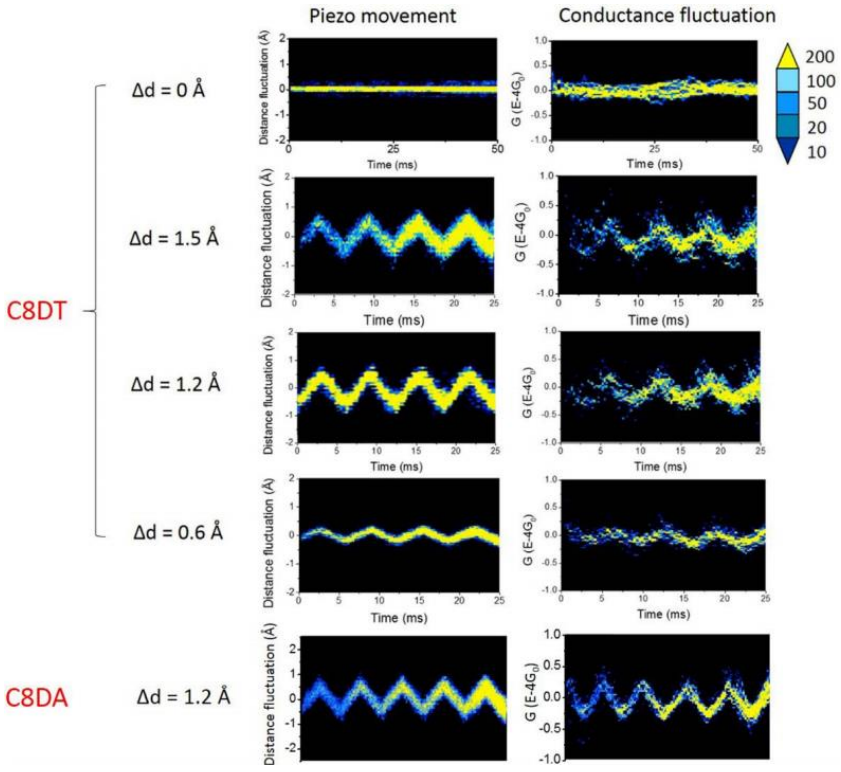

Figure 3.6 Two-dimensional (2D) illustration of the overlay of piezo signal and conductance signal of around 70~80 conductance plateaus for C8DT and C8DA at each modulation amplitude with regular conductance fluctuation. Reprinted from the supporting information of ref. 60.

When the TRI modulation was applied on a free-held single-molecule junction, regular conductance fluctuation in the opposite phase with the PZT movement signal was observed, which is in sharp contrast to the featureless conductance plateau when no modulation was applied. **Figure 3.5B, C and E** show the typical non-modulated conductance trace, modulated C8DT conductance trace and modulated C8DA conductance traces, respectively. The 2D illustration of the overlay of conductance traces used for further analysis under different modulation amplitudes is shown in **Figure 3.6**. We find that the regular conductance fluctuation only occurred when TRI modulations were applied. This proves that the conductance change is predominantly caused by the junction separation regulation rather than other factors such as thermal vibration and mechanical noise. It was also found that for C8DT, the TRI modulation could induce conductance switching from one single-molecule conductance set to another, and the switching probability increases with the increase of the modulation amplitude. Since conductance switching is not representative for most conductance changes induced by junction extension and it may introduce statistical errors, we rule out conductance traces with conductance switching events in further statistical analysis. Given the fact that mechanical modulation did not necessarily induce a conductance change in the plateau, we also rule out the segment of a conductance plateau with a non-obvious conductance change under TRI modulations. Here we focus on the conductance decrease regions of regular conductance fluctuations (red dash-square in **Figure 3.5C and E**). This decrease

in conductance occurred when the junction was further extended by a distance of Δd. We treat the conductance value right before the action of junction extension as a reference conductance G_{mol}. The value of G_{mol} is contributed by the junction at the very moment right before the junction was further extended. So, based on **Eqn. (3.2)**, $G_{mol} = AT_{mol} \times T_{C0} = Aexp(-\beta_{mol}L_{mol})exp(-\beta_{C0}L_{C0})$, where A is a constant. Note that T_{C0} represents the already existing contact transmission coefficient at the moment prior to junction extension, and β_{C0} and L_{C0} are the already existing contact decay constant and contact barrier width, respectively. The conductance decrease initiated from G_{mol} can then be attributed to the extra contact barrier caused by the mechanical extension of the junction. Therefore, during further junction extension, the value of G_{mol} should remain unchanged. For the junction extension-induced conductance decrease region, we obtain $\mathrm{G} = G_{mol} \times T_C = G_{mol} \times exp(-\beta_C \Delta d) = G_{mol} \times exp\left(-1.025\Delta d\sqrt{\emptyset_C}\right)$, where β_C is the contact decay constant and Δd is the extension distance amplitude. Based on this understanding, the extra contact barrier heigh $\emptyset_C$ and contact decay constant β_C can be derived as

$$\emptyset_C = \left(\frac{1}{1.025}\right)^2 \times \left(\frac{\partial lnG}{\partial \Delta d}\right)^2 \; and \; \beta_C = -\frac{\partial lnG}{\partial \Delta d} \tag{3.3}$$

We first analyze the conductance decrease region by plotting them in the $lnG \; vs \; \Delta d$ fashion. Typical $lnG \; vs \; \Delta d$ curves of C8DT and C8DA junctions are shown in **Figure 3.5D and E**, respectively. We see that the $lnG \; vs \; \Delta d$ relation of a single C8DA junction nearly follows a straight line as the junction extends. Yet, the $lnG \; vs \; \Delta d$ relation of C8DT deviates from the linear relation, particularly for a short distance at the beginning of the junction extension. This difference in the $lnG \; vs \; \Delta d$ relation of C8DT and C8DA is more obvious when taking the negative differential of the $lnG \; vs \; \Delta d$ relation which leads to the contact decay constant β_C (see the insets of **Figure 3.5D and**

E). Interestingly, the contact decay constant β_C of C8DT displays an ascending region followed by a plateau region, which is in sharp contrast to the nearly constant β_C value of C8DA across the entire extension distance. This phenomenon was observed for most measured conductance traces but varies slightly from individual trace to individual trace. As the molecule–electrode interface elongates, the variable contact decay constant is inherently caused by a contact tunneling barrier with a non-constant barrier height. It can, then, be inferred that when the junction extends, the contact tunneling barrier of the Au–C8DT–Au junction does not obey a rectangle shape as the contact barrier of the C8DA junction and the tunneling barrier of alkane molecular core do.[66, 67] We emphasize that the fundamental of the STM break junction method is built on statistical analysis which aims to discover the most probable behavior of many molecular junctions, and the definition of the electron transport properties of a molecular junction. Thus, to probe the average change in the contact barrier and the contact decay constant as junction separation extends, we then derive the contact barrier height $\emptyset_C \; vs \; \Delta d$ relation and $\beta_C \; vs \; \Delta d$ relation at a discrete extension distance using **Eqn. (3.3)**, and the results are shown in **Figure 3.7**. At each extension distance, the data point in **Figure 3.7** was obtained by taking the most probable value of those contributed from many conductance decrease events. We see that the contact barrier of C8DA remains nearly constant despite a slight fluctuation. However, the contact barrier $\emptyset_C$ of C8DT follows an evolutionary trend that first roughly increases linearly with the extension of the junction and then reaches a plateau value after a threshold extension distance of around 0.5 Å (**Figure 3.7A**). This trend for C8DT was confirmed by measurements using three different modulation amplitudes (Δd= 0.6, 1.2, 1.5Å), which rules out the modulation-induced

error. The plateau height of the C8DT contact barrier is ~0.16 eV. This is far smaller than the tunneling barrier height (~1 eV) between the Fermi level of the electrode and the frontier molecular orbitals of the alkane molecular core but slightly greater than the contact barrier height of C8DA (~0.14 eV). The contact decay constant β_C displays a similar variation trend as the contact barrier shows (**Figure 3.7B**). The plateau value for β_C of C8DT is around 0.4 Å^{-1} which is much smaller than the decay constant of the alkane molecular core studied in previous studies[66, 67](0.8~1 Å^{-1}) but slightly larger than that of C8DA (0.35 Å^{-1}). The much lower contact barrier height and smaller decay constant further suggest that this decrease in conductance is not contributed by the alkane molecular core.

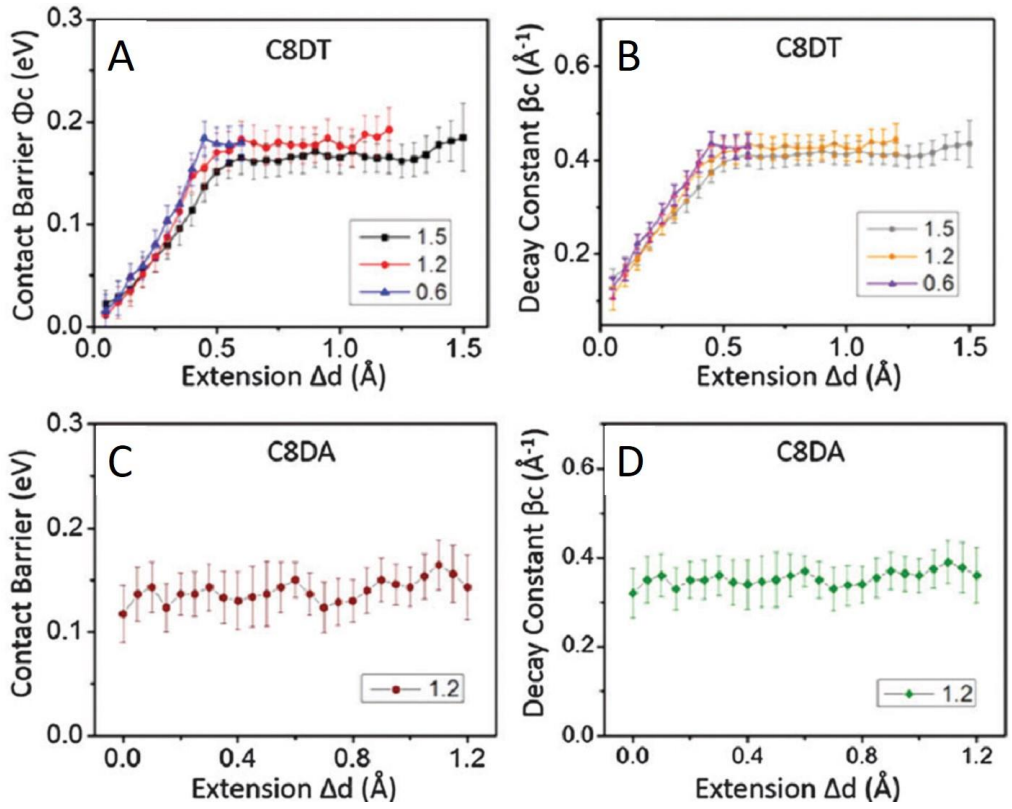

Figure 3.7 (A) C8DT contact barrier height $\emptyset_C$ vs. extension distance Δd plot. (B) C8DT contact decay constant β_C vs. extension distance Δd plot. (C) C8DA contact barrier height $\emptyset_C$ vs.

extension distance Δd plot. (D) C8DA contact decay constant β_C vs. extension distance Δd plot. Note that three modulation amplitudes (Δd = 0.6, 1.2, 1.5 Å) were applied for C8DT, and the modulation amplitude of Δd = 1.2 Å was applied for C8DA. For each modulation amplitudes, the data points in each plot are obtained by averaging around 100 regular conductance decrease regions. The error bar for each data point represents the standard deviation of the statistical analysis. Reprinted from ref. 60.

Comparing the C8DA and C8DT contact barriers, we find that the contact barrier of C8DA leads to more conductance reduction compared to C8DT despite the fact that its barrier height is smaller than the plateau region of the C8DT contact barrier. Indeed, under Δd = 1.2 Å, the average decrease in conductance caused by the C8DA contact barrier is ~$4.7\times10^{-5}G_0$, while the decrease in conductance induced by the C8DT contact barrier is ~$3.5\times10^{-5}G_0$. Given the identical molecular core of C8DT and C8DA, the difference in contact tunnelling barriers must arise from the difference between Au–thiol and Au–amine bonds, namely the coupling nature of molecule–electrode interfaces. The nearly unchanged contact barrier of C8DA under junction extension is surprising but could be reasonable when taking the overly strong Fermipinning effect of the Au–amine bond into account,[96, 97] although Au–thiol usually has stronger binding energy than Au–amine in the stationary state.[98-100] More importantly, it was recently found that under the STM-BJ setup, the most probable Au–thiol contact configuration of the alkanedithiol molecular junction possesses top-bridge configuration, which is different from the hollow–hollow configuration in which the most probable Au–amine bond holds.[95] However, full understanding of this experimental feature requires thorough theoretical simulations considering all possible factors, which is out of scope of this paper. In

addition, it is worth noting that the contact decay constant of the C8DT/C8DA molecule determined in the present work is quite comparable to the decay constant of the molecular core of some conjugated molecules (0.3~0.5 $Å^{-1}$),[101-104] despite the fact that it is muchsmaller than the molecular core decay constant of most saturated molecules (0.7~1.1 $Å^{-1}$).[105-109]

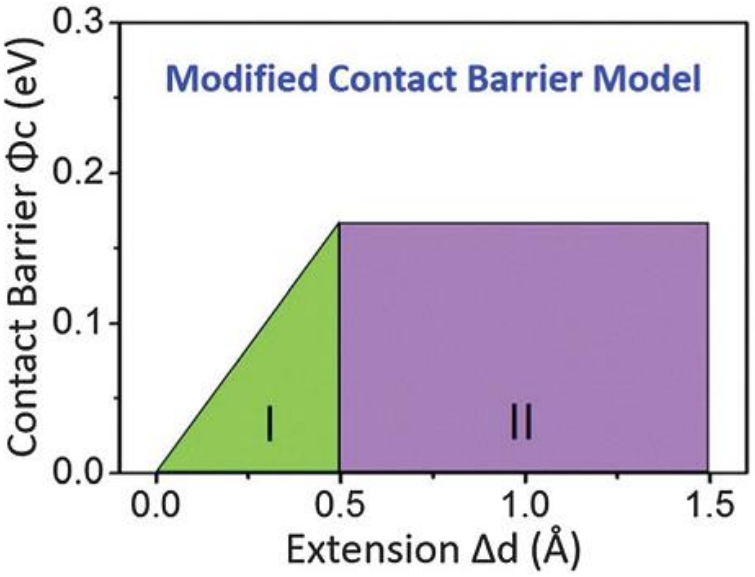

Figure 3.8 A proposed contact barrier model that has two regions (I and II) with different barrier profiles. Reprinted from ref. 60.

What is of most interest is the non-rectangle tunneling barrier of C8DT junction contacts. Previous theoretical studies have proposed multiple non-rectangle barrier shapes by taking different effects, mainly the image charge effect, into account.[90, 110-112] To understand these experimental phenomena, we propose a modified contact barrier model that applies to the range of modulation amplitudes used in this study (**Figure 3.8**). As **Figure 3.7A** suggests, this model assumes a linear increase of the contact barrier height within the extension distance region I ($0 < \Delta d < 0.5$ Å) followed by a constant barrier

height within extension region II ($0.5 < \Delta d < 1.5$ Å). To obtain the necessary parameters, for example, the slope of the linear increase region and the accurate height value for the barrier plateaus, a linear fit to the data points shown in **Figure 3.7A** was applied. For the data of modulation amplitude Δd = 0.6 Å, linear fitting is only performed for region I due to the lack of data points in the barrier plateau region. The fitting results reveal an important relation between the contact barrier and the extension distance. **Table 3.1** shows the parameters extrapolated from this fitting. Using these parameters, a modified equation for the contact barrier transmission coefficient T_C can be derived as

$$T_C = exp\left(-1.025 \int_0^{\Delta d} \sqrt{\emptyset_C(\Delta d)}\, d(\Delta d)\right)$$

$$= exp\left[-1.025 \times \left(\int_0^{0.5} \sqrt{\emptyset_{CI}(\Delta d)}\, d(\Delta d) + \int_{0.5}^{1.5} \sqrt{\emptyset_{CII}(\Delta d)}\, d(\Delta d)\right)\right] \quad (3.4)$$

The conductance can then be calculated in the form of $G = G_{mol} \times T_C$. Here we use the G_{mol} of $9\times10^{-5}G_0$ which is the most probable conductance prior to the junction extension observed in our experiments. Using **Eqn. (3.4)** and the parameters shown in **Table 3.1**, the calculated conductance decrease curve induced by a mechanical extension of 1.5 Å is plotted in **Figure 3.9A**. For clarity, the two regions are plotted in different colors (green for region I and purple for region II). We note that the overall conductance decrease calculated using **Eqn. (3.4)** is around $3.71\times10^{-5}G_0$. This value is very close to the experimentally observed conductance reduction ($3.76(\pm0.09)\times10^{-5}G_0$).

Table 3.1. Contact barrier parameters determined by linear fitting

Δd (Å)	$\emptyset_{CI}(eV) = a + b\Delta d \ (0 < \Delta d < 0.5\text{Å})$		$\emptyset_{CII}(eV)(0.5 < \Delta d < 1.5\text{Å})$
	a	b	
0.6	0.0018	0.41	---
1.2	0.0022	0.39	0.176

1.5	0.0034	0.31	0.165

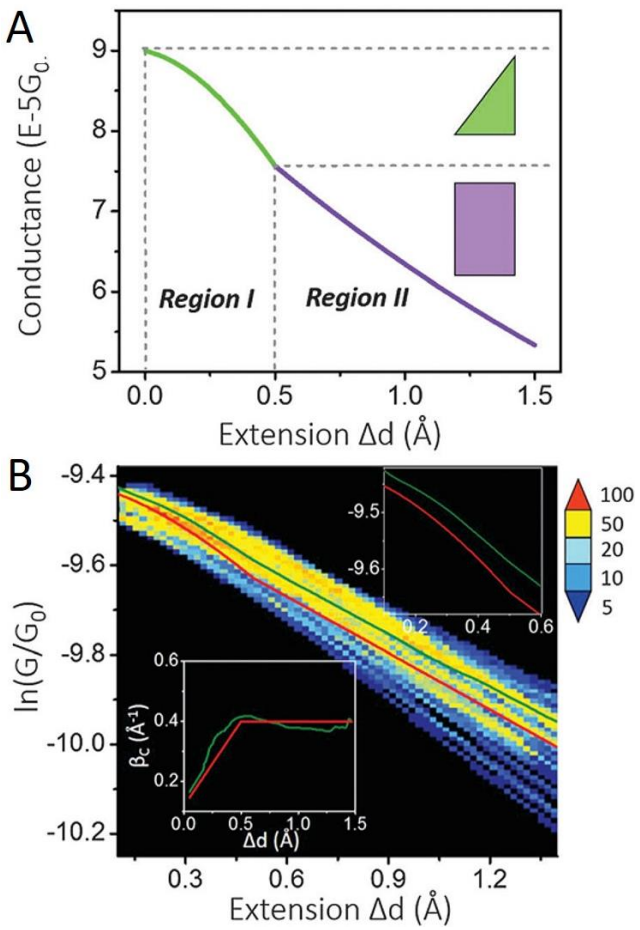

Figure 3.9 (A) Calculated conductance decrease curve with G_{mol}= 9×10^{-5}G$_0$. (B) Experimental two-dimensional (2D) $lnG\ vs\ \Delta d$ relation and the averaged curve (green) over 68 experimental curves that has a G_{mol} of around 9($\pm$1) ×10^{-5}G$_0$, and the calculated $lnG\ vs\ \Delta d$ curve (red). The upper-right inset shows the zoom-in view of region I which has the non-linear relation of $lnG\ vs\ \Delta d$. The lower-left inset displays $\beta_C\ vs\ \Delta d$ relation of the experimental average curve (green) and the theory-predicted curve (red). Reprinted from ref. 60.

To compare with the experimental data, the calculated conductance curve is also shown in the form of $lnG\ vs\ \Delta d$ (red curve in **Figure 3.9B**). The 2D illustration of raw

experimental $lnG\ vs\ \Delta d$ curves (68 conductance decrease curves) with an initial conductance G_{mol} of $9(\pm 1) \times 10^{-5} G_0$ and their average curve (green curve in **Figure 3.9B**) was also plotted. We see that the distribution of the raw experimental curves starts within a converged region which is associated with the non-rectangle segment of the contact barrier and then spreads out linearly as the extension distance increases over 0.5 Å. The upper-right inset of **Figure 3.9B** shows the magnified view of the non-linear $lnG\ vs\ \Delta d$ relation of the calculated curve (red) and the experimental average curve (green). It can also be seen from the lower-left inset of **Figure 3.9B** that the experimental $\beta_C\ vs\ \Delta d$ curve (green) matches well with the curve (red) predicted by the proposed modified contact barrier model.

Research studies focusing on the mechanical extension-induced change in the charge transport properties of single-molecule break junctions have been reported both experimentally and theoretically.[93, 113-116] Due to junction extension, specific changes in conductance have been attributed to different reasons: the increase in extension-induced conductance was attributed to the molecular orbital alignment change across the junction for the benzenedithiol molecule[116] and the change in the π-conjugation degree for 1,4-anthracenedione and 1,4-anthracenediol molecules.[113] It is also evident that for the Au–S contact, the contact bonding geometry can alter and switch among different contact configurations under junction pulling, which inherently changes the coupling strength between the molecule and the electrode and further varies the tunneling barrier across the molecule–electrode interfaces.[66, 67, 70, 73] A previous (density functional theory) DFT molecular dynamic study has highlighted the sensitivity of contact interfaces to the extra

junction pulling after a octanedithiol molecule was fully straightened resulting in a subtle yet non-trivial change in current transmission through the entire junction.[73]

Experimental techniques, like used in this work, that are capable of plumbing latent but important details involved in a non-equilibrium sample Au–molecule–Au junction help in gaining deeper understanding via interpreting important parameters. As discussed above, under the used experimental setup, the experimental results reveal an interesting change in the contact barrier of the Au–C8DT–Au junction, particularly for the initial 0.5 Å of stretching. This non-rectangle tunneling barrier is analogous to the rounded edge of the Simmons model barrier after considering the image charge effect.[90, 112] However, as reported very recently, the image charge effect was usually overestimated by a factor of 2 in previous theoretical calculations.[112] By making the correction of overrating, the resulting conductance decay clearly showed a sub-exponential dependence of conductance over distance as what we observed in **Figure 3.5d**.[112] A major difference in our work and previous theoretical studies lies in that previous studies took the entire junction including the molecular core and molecule–electrode interfaces, but the present study mainly focuses on the molecule–electrode contact parts. However, this resemblance between the observed non-rectangle barrier and the previous theoretical calculations still suggests the image charge effect as one of the possible reasons that lead to the observed contact barrier shape of the C8DT junction as the image charge effect indeed arises at the molecule–electrode interfaces, although a thorough understanding of the observed non-rectangle contact barrier requires advanced theoretical simulations.

As hinted recently that the most probable Au–thiol contact configuration under the STMBJ setup is ‘top-bridge’ configuration for the Au–C8DT–Au junction,[95] the

results shown in this work provide details about how the C8DT contact tunneling barrier evolves when the contact configuration migrates from 'top-bridge' towards a configuration with lower conductance. The unprecedented shape difference of the contact tunneling barrier across Au–thiol and Au–amine interfaces again highlights the significant influence of the coupling nature of electrode-anchor groups. Our study demonstrated the direct experimental evidence of the contact tunneling barrier of single-molecule junctions using the modified STM break junction technique, and the results confirmed previous theoretical assumptions and offer more details.

Given the highly consistent charge transport properties of alkane-family molecules, one can assume that the contact barrier of C8DT should also apply to other alkanedithiol molecules with a similar length when they are measured using the same techniques. To test this hypothesis, we then measure the C6DT molecule following the method used for C8DT. As expected, the contact decay constant and the contact barrier of C6DT follow the same trend as C8DT does, and the values of β_C and $\emptyset_C$ are quite close to those of C8DT. However, it is necessary to note that the length change of the carbon chain would not be trivial for longer alkane molecules, because they are more flexible and easier to be stretched than short molecules, and then the source of the change in conductance in such a modulated junction system becomes more complex.[95] Hence, the tunneling barrier model reported here may not be a good fit to longer alkanedithiol molecules (C_NDT (N>10)). In addition, we do not claim that the non-rectangle contact barrier shown in this work holds for molecular junctions with the Au–thiol bond as the molecule–electrode interface but with different molecular cores. The change may come from the physical nature of the molecular core. For example, the different sets of single-

molecule conductance of alkanedithiol molecules are usually undistinguishable when changing the molecular core to DNA molecules but still keeping Au–thiol contacts, which means the role of contact effect could be trivial for some cases.[104, 117] Nevertheless, an important message that can be sent is that a non-rectangle contact barrier should be carefully considered for short alkanedithiol junction systems in future theoretical and experimental research studies. This work is an important addition to the complete picture of molecule–electrode contact effects, particularly for the alkane molecular junctions, which have been widely studied yet still not fully understood.

3.2.5 Conclusion

Using the modified STM break junction technique, the molecule–electrode contact barrier of Au–C8DT/C8DA–Au junctions has been studied under mechanical extension with different TRI modulation amplitudes. The experimental results revealed an interesting evolutionary trend of the contact barrier height of C8DT: a linear increase followed by a plateau, which contrasts with that of C8DA. A modified contact barrier model was proposed to interpret the observed phenomena, and the calculated results based on this model agree well with the experimental data. This work demonstrates the direct measurement of the contact tunneling barrier of single-molecule junctions and provides new understanding into the nature of the molecule–electrode contact in molecular junction systems.

CHAPTER 4

RECTIFICATION OF SINGLE-MOLECULE JUNCTION CAUSED BY ASYMMETRIC CONTACTS

❖ [100] K. Wang, J. Zhou, J. Hamill, B.Q. Xu, J. Chem. Phys., 2014, 141, 054712. Reprinted here with permission of publisher.

4.1 Abstract

The contact effects of single-molecule break junctions on rectification behaviors were experimentally explored by a systematic control of anchoring groups of 1,4-disubstituted benzene molecular junctions. Single-molecule conductance and I-V characteristic measurements reveal a strong correlation between rectifying effects and the asymmetry in contacts. Analysis using energy band models and I-V calculations suggested that the rectification behavior is mainly caused by asymmetric coupling strengths at the two contact interfaces. Fitting of the rectification ratio by a modified Simmons model we developed suggests asymmetry in potential drop across the asymmetric anchoring groups as the mechanism of rectifying I-V behavior. This study provides direct experimental evidence and sheds light on the mechanisms of rectification behavior induced simply by contact asymmetry, which serves as an aid to interpret future single-molecule electronic behavior involved with asymmetric contact conformation.

4.2 Introduction

The original considerations of molecular electronics were to search for molecule candidates with rectification behaviors. The experimental attempts of a single-molecule rectifier will pave steps towards future functional molecular electronic devices. Since first proposed by Aviram and Ratner,[5] molecular rectifier has gained considerable attention in both experimental designs[118-121] and theoretical simulations.[122, 123] One of the most promising candidates stems from a molecular heterojunction which describes a molecular junction with asymmetric conformation. The asymmetric conformation of a molecular junction was believed to lead to asymmetric electronic behavior such as asymmetric I-V

characteristics, a marked feature for future applications as a molecular diode. Within an Au-molecule-Au junction system, the conformational asymmetry could mainly come from two sources: (1) the molecular core and (2) the contacts that bridge the molecule with two electrodes. Compared with steady experimental and theoretical progress on studying molecules with asymmetric molecular core, investigations on the contact effect have not yet come up with a credible response. Although theories predicting the importance of contact interfaces in determining the electron transport properties of molecular wires,[71, 123-125] there have been few experimental attempts to investigate the influences of contact effect on the rectification behavior within a single-molecule break junction. Thus, difficulties exist to draw any conclusion before having thorough understanding of each factor contributing to the final electronic behavior of a molecular junction.

In this work, we demonstrate a comprehensive investigation on the electronic behavior of molecular junctions with controls on anchoring groups. Using a scanning probe microscopy break junction (SPM-BJ) technique,[31] electrical measurements were conducted on molecules with a central benzene ring (B), and alternating anchoring groups of thiol (–SH) and amine ($–NH_2$) in an Au-molecule-Au system. The experimental results indicated a strong correlation between contact circumstance and electronic properties. Rectification behavior was observed when an asymmetric anchoring group was introduced into the junction. Upon theoretical calculations and models, we ascribe the rectification behavior to an asymmetric shift of frontier molecular orbital (FMO) with respect to Fermi levels of the electrodes or an asymmetric potential drop, which essentially roots in the asymmetry of coupling strength at the two contacts. This study

provides direct experimental evidence and sheds light on the mechanisms of rectification behavior induced simply by contact asymmetry, which will help to interpret future single-molecule electronic behavior involved with asymmetric contact conformation.

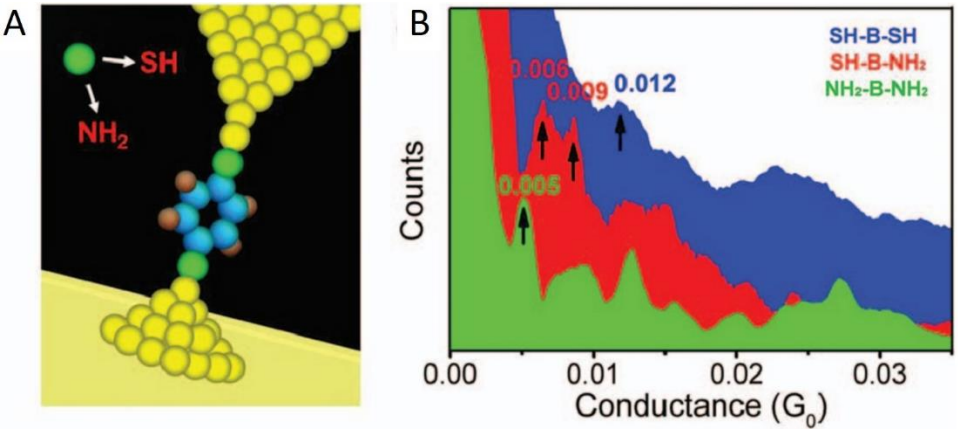

Figure 4.1 (A) Schematic of SPMBJ technique: molecules with a central benzene ring (carbon atoms as blue spheres and hydrogen atoms as brown spheres) and alternating anchoring groups (green spheres) of thiol (–SH) and amine (–NH_2) in an Au-molecule Au system. (B) Conductance histograms obtained by wiring SH-B-SH (blue), SH-B-NH_2 (red), and NH_2-B-NH_2 molecules to Au electrodes under 0.3 V, respectively. The counts value for each histogram is shifted vertically to show the relative position of conductance peaks for different molecules. Reprinted from ref. 100, with the permission of AIP Publishing.

4.3 Experimental Details

Choice of sample molecules Molecules 1,4-benzenedithiol (SH-B-SH), 1,4-benzenediamine (NH_2-B-NH_2), and 4-aminothiolphenol (SH-B-NH_2) were tested separately in the Au-molecule-Au (Au substrate and Au scanning tunneling microscopy (STM) tip) system upon modified SPM break junction (SPM-BJ) technique (**Figure 4.1A**). The molecules with benzene ring backbone were chosen because of the smaller energy gap and high degree of π-conjugation which cause higher electronic

transmissions.[126, 127] According to Landauer's formalism, the expression of the final transmission efficiency (for simplicity, $T = T_{LC} \times T_{mol} \times T_{RC}$, where T_{mol}, T_{LC}, and T_{RC}, respectively, represent transmission efficiencies of molecular core, left contact, and right contact) within a molecular junction incorporates both contact coefficients.[25, 92, 94] Therefore, the influence of contacts on electron transport properties of benzene conjugated molecular junctions could be more pronounced since the simple and symmetric central molecular backbone excludes most distortions from molecular structure itself. Thus, the change of electronic properties primarily roots in the contact parts. These features make 1,4-disubstituted benzene molecules one of the best candidates for contact effect study.

Chemicals and sample preparation 1,4-benzenediamine (purity, 97%) and 4 aminothiolphenol (purity, 97%) were purchased from Aldrich. 1,4-benzenedithiol (purity, 97%) was purchased from Alfa Aesar. For Au substrate deposition, the gold beads come from Kurt J. Lesker company (99.999%), and mica sheets (Grade V1) were from Ted Pella, Inc. Au substrates were prepared by evaporating ~100 nm of gold onto freshly cleaved mica sheets using thermal evaporation in a vacuum of 10^{-7} Torr. The surfaces of Au substrates were annealed by hydrogen flame just before immersion in sample solutions. This annealing step cleaned the surface and allowed epitaxial reconstruction of the Au to form large terraces of Au (111). All molecules were prepared as 1 mM solutions in toluene. Each sample solution was put into a liquid cell and a self-assembled monolayer (SAM) was formed on an Au substrate after 6h exposure. Then the coated samples were fixed in the STM system for the characterization. A 0.25 mm diameter gold wire (purity, 99.999%, Alfa Aesar) was sharply cut and then coated with wax as STM

tips before each experiment. A STM scanner with 1000 nA/V preamplifier was applied for all measurements.

Single-molecule conductance and I-V characteristic measurements The measurements of single-molecule conductance were performed using a SPMBJ technique. Under a constant 0.3 V bias, the STM tip was driven by piezoelectric transducer (PZT) continuously towards and away from Au substrate to form and break molecular junctions. Conductance traces were repeatedly recorded during the retracting process where the STM tip was pulled away from Au substrate. For each measurement, around 1000 traces were collected for the construction of a conductance histogram. In the final conductance histogram, the most prominent peak was the most probable conductance of corresponding molecular junction. In addition, I-V curves of each molecular junction were measured using a modified SPM- BJ technique,[56] where the tip retracting process was divided into multiple periodic processes each of which contained two parts: abrupt stretching and free holding. Using a homemade Labview program, with the constant 0.3 V nulled by a reverse bias, an I-V sweep from –1 V to 1 V was applied on each free holding process. Thus I-V curves of single molecular junction could be collected whenever one molecule was wired between the tip and substrate. In all experiments, the bias was consistently applied on the Au substrate with the STM tip grounded. In total two groups of molecular junctions employing different molecules were characterized: (i) symmetric molecular junctions, Au-SH-B-SH-Au and Au-NH_2-B-NH_2-Au; (ii) molecular junctions with asymmetric anchoring groups, Au-SH-B-NH_2-Au or Au-NH_2-B-SH-Au. Here, the molecular junction was represented in the form of substrate-molecule-tip and this applies to all junctions subsequently referred to in this work.

4.4 Results and Discussions

4.4.1 Single-molecule conductance measurements

We carried out the single-molecule conductance measurements by separately wiring three molecules in the Au-molecule-Au junction system and creating conductance histograms from the resulting data (see **Figure 4.1B**). Noticeably, the Au-NH_2-B-NH_2-Au conductance histogram (green, 726 in ~1300 traces) shows thin but pronounced peaks. The value of the first peak ($0.005G_0$) is close to other previously reported values.[98, 128] In the histogram of Au-SH-B-SH-Au (blue, 806 in~1300 traces), a set of dominant conductance peaks is identified. The conductance value was $0.012G_0$ also coinciding with reported values.[129] Interestingly, compared with Au-NH_2-B-NH_2-Au, the conductance value of the Au-SH-B-SH-Au is much higher and the distributions of conductance peaks become broader although they have identical electrodes and the central molecular core. This shape difference of the histograms is therefore attributed to the different anchoring groups. It was reported that the local amine-Au bonding geometry is remarkably well-defined, with the amine group only binding to undercoordinated Au sites.[128] While, as justified in other discussions,[63, 77] the stronger but more flexible Au–SH bonds may bring perturbations into the junction and consequently result in a wide distribution in molecular conductance. In contrast with the above two molecules, the conductance histogram (red, 711 in~1300 traces) reveals two separate single-molecule conductance peak values ($0.006G_0$ and $0.009G_0$) when SH-B-NH_2 was wired to the system. Both conductance values are located between those of Au-NH_2-B-NH_2-Au and Au-SH-B-SH-Au. We believe this is due to the relatively stronger Au–SH bond within the junction that breaks the symmetry and produces two junction conformations with –SH

bonding to either the Au substrate or Au tip. The formation of two separate conductance peaks should be attributed to asymmetric electronic properties of the two molecular junctions.

4.4.2 I-V characteristics for different molecular junctions

To further probe the influences of asymmetric contacts under a bias sweep (−1 V to 1 V), single molecular I-V characteristics were measured for all molecules. Typical I-V curves for each molecular junction are plotted in **Figure 4.2**. For symmetric molecular junctions Au SH-B-SH-Au and Au-NH_2-B-NH_2-Au, their I-V curves are also symmetric (**Figure 4.2A and 4.2B**). But molecular junction Au-SH-B-SH-Au produced much higher current (∼2500 nA) at +1/−1V than Au-NH_2-B-NH_2-Au (∼700 nA) does. This is in accordance with the conductance measurement results at 0.3 V. In sharp contrast, when molecule SH-B-NH_2 is bridged between Au electrodes, the I-V curves reveal pronounced rectification behavior. Interestingly, the rectified I-V curves illustrate higher current under either negative bias or positive bias despite that only one type of molecule was in the junction. This implies that the molecular junction alternates between two possible conformations on the basis of whether –SH anchoring group is wired to either Au tip or Au substrate. Thus at 0.3 V, two different current values can both be observed. This explains the fact that two single-molecule conductance sets were observed in the conductance histograms (**Figure 4.1B**, red). Noticeably, for rectified I-V curves, the higher current goes up to∼2500 nA which is similar to the ending current of Au-SH-B-SH-Au and the lower current ends at∼1000 nA which is similar to that of Au-NH_2-B-SH-Au, suggesting that SH-B-NH_2 bridged between Au electrodes is a hybrid system of Au-SH-B-SH-Au and Au-NH_2-B-NH_2-Au molecular junctions.

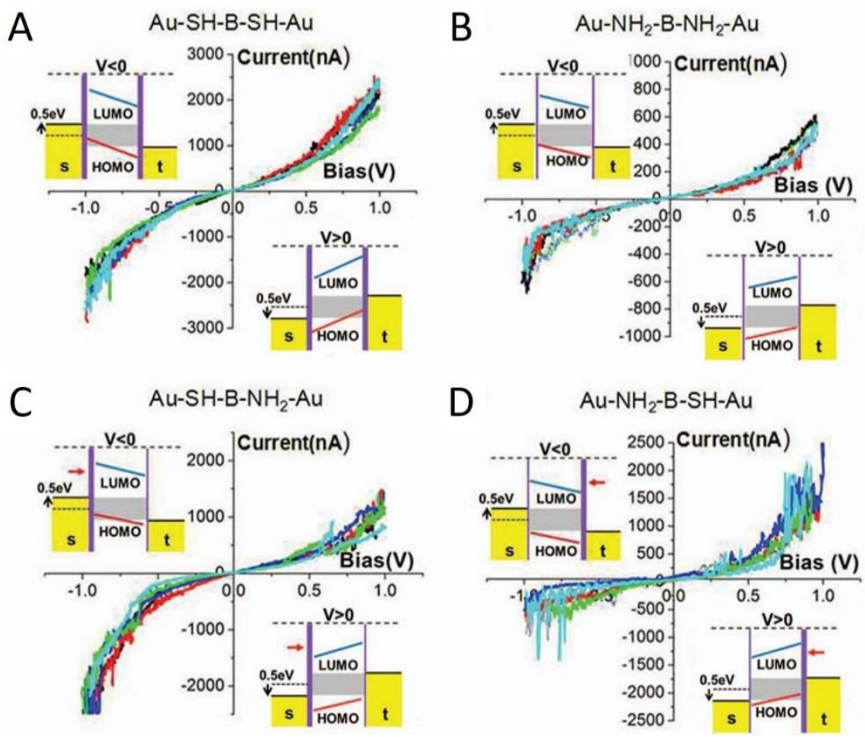

Figure 4.2 (A-D) The I-V characteristics (5 representative curves for each) and the corresponding energy band diagrams for each molecular junction. The red arrows in the energy band diagrams point at the contact with a relatively stronger coupling strength. Reprinted from ref. 100, with the permission of AIP Publishing.

4.4.3 Differential conductance (dI/dV)

To understand the I-V characteristics, differential conductance (dI/dV) profiles are constructed to illustrate the local density of states (LDOS) change introduced with different contact conformation (**Figure 4.3**). The dI/dV curves were calculated using the smoothed I-V curves of the raw I-V curves shown in **Figure 4.2**. The smoothing greatly reduced the fluctuation on the I-V curves but still maintained the global trend of the rectifying effect. This could avoid most of the insignificant information caused by those fluctuations in dI/dV plots. The peaks in a dI/dV plot have been suggested to imply extra

conduction states.[85] In agreement with I-V characteristics, the dI/dV plots reveal symmetric profiles for symmetric junctions Au-SH-B-SH-Au and Au-NH_2-B-NH_2-Au. The symmetry in peak height and position in dI/dV profile of Au-SH-B-SH-Au also indicate a similar LDOS increase under both positive and negative bias. There is no obvious peak in the dI/dV profiles of Au-NH_2-B-NH_2-Au, indicating trivial changes in LDOS within the applied bias range. However, for Au-SH-B-NH_2-Au and Au-NH_2-B SH-Au, pronounced asymmetry in peak height under different bias polarities is observed although the peak position is nearly symmetric. According to dI/dV profiles, much more LDOS are activated under the bias regime where higher current takes place than the lower current side. Interestingly, the asymmetry of LDOS starts at around 0.4 V for I-V curves with higher current at negative bias, which is much earlier than those (0.6 V) with higher current under positive bias. It has to be noted that the inevitable peaks induced by the noise on I-V curves may still exist in dI/dV plot for those rough I-V curves even after smoothing. But the most peaks in dI/dV should be related to the increase in conduction states.

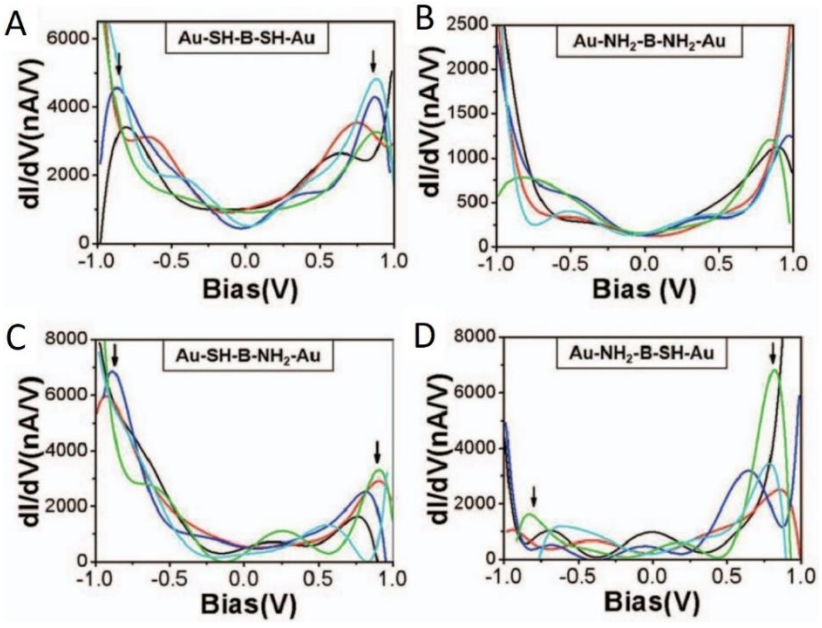

Figure 4.3 (A-D) Differential conductance (dI/dV) profiles for each molecular junction. The arrows in the profiles represent the peak position observed from the dI/dV profiles. Reprinted from ref. 100, with the permission of AIP Publishing.

4.4.4 Energy band model

To gain insights into the mechanisms causing molecular rectification behavior, multiple theoretical mechanisms have been developed, such as the models of Williams,[130] Baranger,[131] Ford,[132] and Whitesides et al..[133] In an asymmetric contact system like ours, the decisive factor rests with the coupling strength between the terminal of the molecules and the electrodes. When an asymmetric component is introduced, the coupling strength at either contact is also asymmetric. As an analogy to the two-barrier model commonly used in the rectification study of asymmetric molecules,[132] the contact with a stronger coupling between the molecule and electrode resembles a narrower barrier through which electrons tunnel across more easily. Oppositely, the contact with a weaker coupling performs like a broader barrier requiring higher energy to access the electron transport. Based on a model recently proposed by Zhao et al.,[134] stronger coupling signifies a closer affinity between the FMO and Fermi levels of the electrodes. In this model, the FMO tends to shift with the Fermi level of the strongly coupled electrode as a whole, when a bias is applied. Thus, at the strongly coupled contact, the absolute difference between FMO of the molecule and Fermi level of the electrode nearly remains constant during the shift. However, at the weaker contact, the FMO shifts independently creating a lag with the movement of Fermi level of the electrode, which either increases or decreases the difference between FMO and Fermi level of the electrode under zero bias. Then, for the weak contact, this difference will increase whenever Fermi level of the electrode shifts up

and it decreases whenever Fermi level of the electrode shifts down. The dominating FMO has been proven to be HOMO orbital for molecules used in our experiments.[99, 128] It has to be noted that LUMO orbitals are far out of the bias window in our experiments on account of the HOMO-LUMO gap (4–5 eV) for these molecules.

To explain the experimental results, coupling strength introduced with various contact conformations needs to be clarified. Binding energies of contact bonds in our study have been calculated to be 0.37 eV for Au–NH_2 and 1.60 eV for Au–SH.[98, 99, 135] It is believed that a higher binding energy implies a stronger coupling between the molecule and the electrode,[98, 99] indicating a much stronger coupling for Au–SH than for Au–NH_2. Theoretical calculations[71, 128] suggested that factors like the local bonding length and junction elongation and tilt would not be the major effect within our bias window, which rules out the concerns on the related influence caused by these factors.

We plot the energy band diagram for each molecular junction as the inset in **Figure 4.2**. For Au-SH-B-SH-Au and Au-NH_2-B-NH_2-Au junctions, the coupling strength at both contacts was identical. As Fermi levels of the electrodes shift under a bias sweep, the relative difference between MOs and electrodes remains nearly constant at either contact. Hence, similar delocalized states would be obtained under both bias polarities. Namely, a symmetric I-V characteristic should be observed, which agrees with experimental I-V curves (**Figure 4.2A and 4.2B**). For junctions with asymmetric anchoring groups like Au-SH B-NH_2-Au or Au-NH_2-B-SH-Au, the coupling strength of Au-SH is much stronger than that of Au-NH2, delocalizing more states when the Fermi level of the strongly coupled electrode shifts up. Therefore, for the Au-SH-B-NH_2-Au junction where –SH is wired to Au substrate, higher current should be obtained under

negative bias as illustrated in experimental I-V curves (**Figure 4.2C**). Oppositely, I-V characteristic for the other orientation Au-NH_2-B-SH-Au reveals a reversed rectification with higher current at positive bias which was also in accordance with this model.

4.4.5 I-V Calculations

Transition voltage spectroscopy A Fowler-Nordheim (F-N) plot of an I-V curve measured from a SMBJ can yield minima at specific transition voltages.[136] The bias voltage at a specific minimum signifies the transition voltage where a trapezoid shaped tunneling barrier turns to a triangle shaped barrier. It is important to note that the transition voltage is usually smaller than the bias potential necessary for the resonant tunneling. As is shown in **Figure 4.4**, for symmetric junctions Au-SH-B-SH-Au and Au-NH_2-B-NH_2-Au, relatively symmetric features were observed in the F-N curves (black and green). But the F-N curve of Au-SH-B-SH-Au lacks the well-defined minima which were observed in the F-N curve of Au-NH_2-B-NH_2-Au. This suggests that the transition voltage for Au-SH-B-SH-Au lies outside the bias window (−1 to 1 V) applied in our experiments. For the two asymmetric junctions, only one side of F-N plots show pronounced minimum and the displacement of F-N curves is rather asymmetric. The transition voltages for Au-SH-B-NH_2-Au and Au-NH_2-B-SH-Au are determined to be −0.45 V and 0.65 V, respectively. The transition voltages for Au-NH_2-B-NH_2-Au are determined to be −0.85 V and 0.85 V under negative and positive bias, respectively. Previous study suggested that a relatively weak binding energy leads to a smaller difference between the Fermi level of electrodes and FMO.[99] This may explain why transition voltage of Au-NH_2-B-NH_2-Au is reached earlier than that of Au-SH-B-SH-Au. Using the well-defined minima at both sides of the F-N plot for Au-NH_2-B-NH_2-Au, the

energy gap ε between the Fermi level of the electrodes and FMO is calculated to be 0.69 eV, suggesting that the HOMO of NH_2-B-NH_2 is still outside the conduction window (−0.5 eV to 0.5 eV). Due to the lack of well-defined minima at both sides of the F-N curves for the other molecular junctions, it is not possible to derive the energy gap via transition voltage spectroscopy (TVS) analysis.

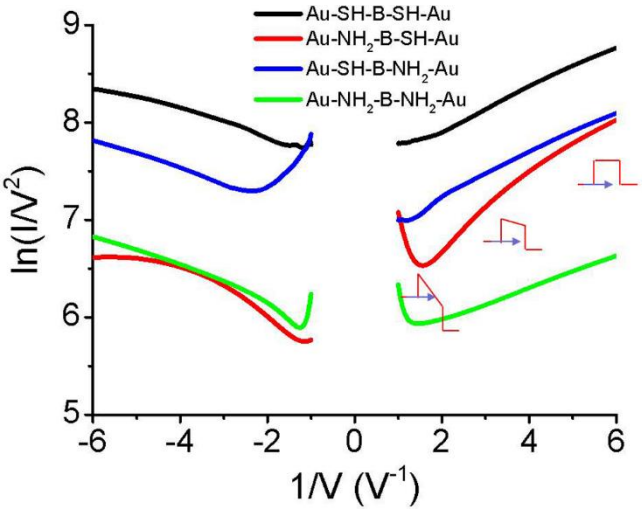

Figure 4.4 F-N plots for each molecular junction. The change in tunneling barrier from rectangular shape, trapezoid shape to triangle shape is demonstrated along the F-N curve of Au-NH_2-B-SH-Au (red). Reprinted from ref. 100, with the permission of AIP Publishing.

Laudauer Fitting I-V curve can also be fit to a simplified Landauer formula, **Eqn. (4.1)**, using a Levenberg-Marquardt least squares fitting algorithm:[137]

$$I(V) \propto \int_{-\infty}^{\infty} T(E,V)\left[f(E-\frac{eV}{2}) - f(E+\frac{eV}{2}) \right] dE \tag{4.1}$$

where $$T(E,V) = 4\Gamma_L\Gamma_R \left\{ \left[E - \varepsilon - \frac{eV}{2}\left(\frac{\Gamma_L - \Gamma_R}{\Gamma_L + \Gamma_R} \right) \right]^2 + \left[\Gamma_L + \Gamma_R \right]^2 \right\}^{-1} \tag{4.2}$$

Using **Eqn. (4.1) and (4.2)**, experimental I-V curves can be fitted to three parameters. The three parameters correspond to the gap ε, and the degree of coupling, Γ_L and Γ_R, to each electrode separately. When this fitting method was applied to the different junctions with variable anchoring groups, the results agreed with observations made from the qualitative analysis of the I-V curves (see **Table 4.1**). The junctions when symmetric yielded symmetric values for Γ_L and Γ_R, and yield unequal values when the junctions were asymmetric. This provides a quantitative confirmation for the observation that the asymmetric junctions yielded asymmetric I-V curves due to unequal coupling to the molecule.

Table 4.1 Landauer formula fitting results for all molecular junctions

Molecular junction	Γ_L **(eV)**	Γ_R **(eV)**	ε_{fit} **(eV)**
Au-NH_2-B-NH_2-Au	1.49×10^{-2}	1.52×10^{-2}	0.636
Au-SH-B-SH-Au	3.95×10^{-2}	3.86×10^{-2}	0.698
Au-SH-B-NH_2-Au	6.32×10^{-2}	2.92×10^{-2}	0.848
Au-NH_2-B-SH-Au	1.77×10^{-2}	2.71×10^{-2}	0.735

The energy gap for Au-NH_2-B-NH_2-Au calculated from Landauer fitting is close to the results of TVS analysis. And two symmetric junctions yield a similar energy gap value, which is close to previous reported value.[128] We see that the Γ value for Au-SH is larger than Au-NH_2, which coincides with the previous bonding energy calculations. We also find the introduction of asymmetric anchoring groups alters the FMO and increases the energy gap in asymmetric junctions. It is apparent the energy gap for all molecular junctions is over the applied external energy (0.5eV) applied in our experiments. Overall, the Landauer fitting results imply a non-resonant tunneling charge transport for all

molecular junctions and asymmetric coupling strength at the molecule-electrode contact as the cause of the rectification behavior.

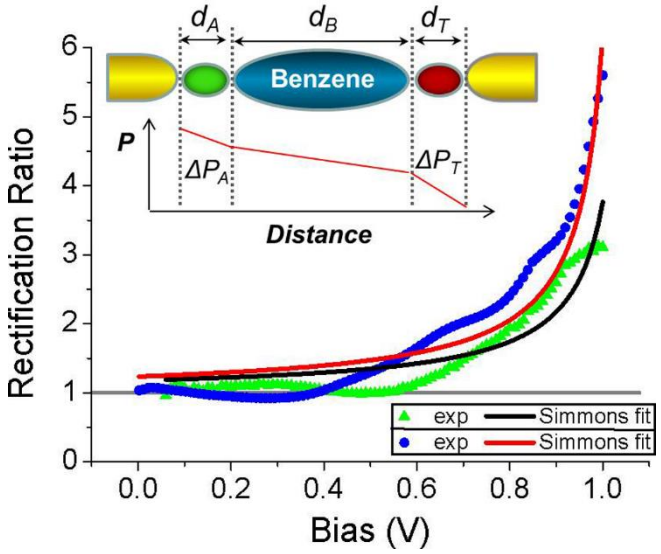

Figure 4.5. Rectification ratio plot for asymmetric junctions of experimental data and corresponding fitting using **Eqn. (4.6)**: Au-NH_2-B-SH-Au (green triangle for experimental data and black curve for Simmons fit) and Au-SH-B-NH_2-Au (blue circle for experimental data and red curve for Simmons fit). The inset shows a schematic of potential drop across different segments of the molecular junctions. d_B is the length of the benzene molecular core and d_A and d_T represent the length of amine and thiol anchoring group, respectively. ΔP_A and ΔP_A represent the potential drop along amine group and thiol group, respectively. The modified Simmons model only cares about the change in potential drop difference $\Delta P = |\Delta P_A - \Delta P_B|$ from forward bias regime to reverse bias regime. Reprinted from ref. 100, with the permission of AIP Publishing.

4.4.6 Rectification Ratio Model

The rectification ratio (RR) calculation reflects the degree of asymmetry as a function of applied bias for asymmetric I-V characteristics. Here we define $RR = |I_{hign}/I_{low}|$. RR for molecular junctions displaying rectification effect is plotted in

Figure 4.5. As expected, the RR for symmetric junctions stays around 1 across the whole bias range, indicating a nearly equal current under positive and negative bias. We see the RR for Au-SH-B-NH_2-Au stays around 1 at lower bias range (0~0.3V), starts increasing at around 0.4V and ends over 5 at 1V. RR for Au-NH_2-B-SH-Au starts increasing later at around 0.6V and ends around 3 at 1V. The onset voltages of rectification, where RR starts increasing beyond 1, agree well with the transition voltages determined by TVS analysis. We ascribe the difference in onset voltage for two asymmetric junctions to different contact geometries induced via bonding thiol group to the sharp Au tip or the flat Au substrate.

Using the Simmons model[89, 90] with image potential included, the current density for intermediate voltage range applicable for our experiment is given by

$$J = J_0\left[\varphi\exp\left(-\kappa\beta_m\sqrt{\varphi}\right)-\left(\varphi+eV\right)\exp\left(--\kappa\beta_m\sqrt{\varphi+eV}\right)\right] \tag{4.3}$$

where $$J_0 = \frac{e}{2\pi h\left(\beta_m d\right)^2}$$

and $$\kappa = \frac{4\pi d\sqrt{2m_e^*}}{h}$$

where φ is the average value of the barrier height considering image potential, β_m is the barrier decay constant, d is the distance across the barrier along the whole molecular junction including end groups, h is Plank constant, and $me*$ is the effective mass of electron. Noticeably, the barrier width is not considered since it is not parameterized in Simmons model. A non-unity rectification can be explained by an asymmetric potential drop across the end group-molecule-end group system when the end groups are not identical as the inset schematic of **Figure 4.5** shows. Here we assume that the potential drop across the benzene molecular core is always the same under forward bias and

reverse bias. Defining forward bias to refer to the half of the I-V curve which has higher current, and reverse bias to refer to the lower current half, we can account for this difference in current as a stronger potential drop ($\Delta P = |\Delta P_A - \Delta P_B|$) in the reverse bias direction across the end group which dominates the electron transport over the other end group, and a negligible potential drop across the same end group during the forward bias direction.[138] This case can be incorporated into the Simmons formula by adding a term to account for the influence of the extra barrier decay ($\Delta\beta$) for the end group during the reverse bias. Thus, the current density under forward bias and reverse bias can be written as

$$J_{forward} = \frac{\lambda}{\beta_m^2}\left[\varphi \exp\left(-\kappa\beta_m\sqrt{\varphi}\right) - (\varphi + eV)\exp\left(-\kappa\beta_m\sqrt{\varphi + eV}\right)\right] \quad (4.4)$$

$$J_{reverse} = \frac{\lambda}{(\beta_m + \Delta\beta)^2}\left[\varphi \exp\left(-\kappa(\beta_m + \Delta\beta)\sqrt{\varphi}\right) - (\varphi + eV)\exp\left(-\kappa(\beta_m + \Delta\beta)\sqrt{\varphi + eV}\right)\right] \quad (4.5)$$

where $$\lambda = \frac{e}{2\pi\hbar d^2}$$

Using these two forms (**Eqn. (4.4)** and **Eqn. (4.5)**) of the Simmons formula, a formula for the rectification ratio of asymmetric junctions can be derived as

$$RR(V) = \frac{J_{forward}}{J_{reverse}} = \frac{B^2}{A^2} \times \frac{\varphi \exp\left(-A\sqrt{\varphi}\right) - (\varphi + eV)\exp\left(-A\sqrt{\varphi + eV}\right)}{\varphi \exp\left(-B\sqrt{\varphi}\right) - (\varphi + eV)\exp\left(-B\sqrt{\varphi + eV}\right)} \quad (4.6)$$

where $$A = \kappa\beta_m$$

and $$B = \kappa(\beta_m + \Delta\beta)$$

Fitting our experimental RR curves to **Eqn. (4.6)** yields essential information about the junction. **Eqn. (4.6)** leaves only three fitting parameters: $A, B, and\ \varphi$. The fitting curves for asymmetric junctions are also illustrated in **Figure 4.5**. First, notice that

the rectification ratio for the Au-NH_2-B-SH-Au junction was calculated using $I(+V)/I(-V)$ while for Au-SH-B-NH_2-Au the inverse was used based on our definition. This approach assured us that the rectification ratio was >1 for most of the curve. Fitting parameters are shown in **Table 4.2**.

Table 4.2. The modified Simmons model fitting parameters for two asymmetric junctions

Molecular junction	***A***	***B***	***φ(eV)***	***Δβ/β$_m$***
Au-NH_2-B-SH-Au	1.673	1.712	1.893	3.9%
Au-SH-B-NH_2-Au	2.993	3.149	1.704	5.0%

For both junctions, the fitting parameters indicate that an extra decay constant or larger potential drop occurs under the reverse bias regime, introducing the asymmetry in potential drop and creating the rectification. But Au-NH_2-B-SH-Au has a slightly higher barrier than Au-SH-B-NH_2-Au does. The $\Delta\beta/\beta_m$ value reveals the proportion of additional decay constant added to the forward bias decay constant when under the reverse bias. Au-SH-B-NH_2-Au has a greater $\Delta\beta/\beta_m$ (5.0%), suggesting a larger relative potential drop occurring in the reverse bias regime than that (3.9%) for Au-NH_2-B-NH_2-Au. This also implies a higher RR for Au-SH-B-NH_2-Au, as we observed from the experimental data (blue circle in **Figure 4.5**). Similar fitting yields a straight line with a value of around 1 for both symmetric junctions, which suggests a symmetric potential drop under both bias polarities. This is also in accordance with experimental I-V curves.

The Simmons approximation to the Landauer's formula has proven to be a very powerful tool to study molecular break junctions. However, its canonical form **Eqn. (4.3)** is unable to accommodate asymmetric junctions because it was explicitly derived for

symmetric junctions.[89] By rewriting the Simmons formula in the form of a rectification ratio, asymmetry can be explicitly incorporated into the formula. This both provides a physical model to describe the rectification behavior of any single molecular I-V curve, and adapts the Simmons model for broader use than its original application. Furthermore, it provides a tool to explicitly calculate the contribution of the end groups to the overall character of the I-V curve.

The theoretical analysis demonstrated above provides multiple ways to understand the physical meaning of obtained experimental data. In our study, the rectification behavior of a molecular junction with different anchoring groups is suggested to be induced by an asymmetric relative shift of FMO with respect to Fermi level of the electrode in the energy band model, an asymmetric displacement of transition voltages in TVS analysis, an asymmetric coupling degree in Landauer fitting and asymmetric potential drop in the modified Simmons model. Significant information like this offers us the chance to thoroughly understand the nature of charge transport property within a molecular junction and paves steps towards the ultimate molecular devices. Noticeably, by isolating the contact part, we have studied the rectification behavior simply induced by the asymmetry in contact coupling, which is different from the donor-acceptor model developed for asymmetric molecular core.[139, 140] Interestingly, the rectification ratio we obtained is comparable to some of the donor-acceptor molecules,[133] which again highlights the influence of the contact interfaces.

4.5 Conclusion

In summary, by experimentally exploring the electron transport properties of molecular junctions with asymmetric contact conformations, we have demonstrated a systematic investigation of molecular rectification behavior regarding contact effect of asymmetric anchoring group. Rectification behavior was observed under asymmetric contact conditions. Using theoretical models and calculations, the cause of rectification behavior is mainly attributed to asymmetric coupling strength at the two contacts which leads to an asymmetric relative shift between FMO and Fermi level of the electrodes. A newly modified Simmons model allows us to extract critical parameters from the experimental rectification ratio curve. Using this model, we find that the rectification can also be ascribed to asymmetric potential drop under forward bias and reverse bias. Our results provide important information in understanding the mechanisms of rectification behaviors. Overall, our study will give opportunity to complete the picture of electronic properties related to rectification behaviors in various molecular junctions with asymmetric contacts.

CHAPTER 5

STRUCTURE-DETERMINED CHARGE TRANSPORT IN DNA SINGLE MOLECULE JUNCTIONS

❖ [117] K. Wang, J Hamill, B Wang, CL Guo, S Jiang, Z Huang, BQ Xu, Chem. Sci., 2014, 5, 3425-3431. Reprinted here with permission of publisher.

5.1 Abstract

Experimental study of the charge transport properties associated with structural variations due to a change in the ionic environment will provide essential physical information in determining the nature of DNA molecules. This work reports an experimental study of the change in electronic transport properties induced by the conformational transition of a poly $d(GC)_4$ DNA. By gradually increasing the concentration of $MgCl_2$ in the buffer solution from 0 M to 4 M, the conductance of the single DNA molecule decreased by two orders of magnitude. Circular dichroism (CD) measurements confirmed that a B to Z conformational transition caused the reduction in conductance. Using a stretch-hold mode scanning probe microscopy break junction (SPM-BJ) technique, this B–Z transition process was monitored and a transition trend line was successfully achieved from conductance measurements alone. The transition midpoint occurred at a $MgCl_2$ concentration of 0.93 M for this DNA sequence. This method provides a general tool to study transitions of molecular properties associated with conductance differences.

5.2 Introduction

DNA, the repository of genetic information, has gained considerable attention because of its potential application in tomorrow's molecular electronics, such as building DNA chips.[141, 142] To pave the way towards this goal, great efforts have been made experimentally and theoretically.[143, 144] In order to approximate natural conditions, experiments are usually performed in an appropriate buffer. However, discrepancies exist, not only between experimental results and simulated data, but also among different

experimental studies on similar DNA molecules. For example, a wide range of electronic properties of λ-DNA, varying from insulating to conducting and even to superconducting, have been reported by different groups.[29, 30, 145, 146] Similarly, for the same DNA, the conductance measured in solution was an order of magnitude greater than the conductance measured in dry conditions.[146] As various simulations suggested, it is quite possible that these discrepancies are caused by different experimental conditions, especially different ionic environments in buffer solutions where the electronic properties of DNA were measured.[147-149] Ions surrounding DNA molecules could not only vary the degree of charge delocalization, but also perturb the structure of DNA molecules.

DNA molecules have proven to exhibit surprising conformational versatility, while retaining remarkable precision and uniformity.[150] As well as right handed (RH) B- and A-DNA, left-handed (LH) Z-DNA has also been explored by chemists and biologists due to its biological and medical significance.[151-153] Using circular dichroism (CD), the ionic conditions necessary to induce a conformation shift from a right-handed (RH) B-DNA to a left-handed (LH) Z-DNA helix have been determined for various counterions.[154-156] The presence of ethanol in addition to alkaline metal ions in solution was also reported to cause a RH internal switch from B- to A-DNA.[157, 158]

The conductance of short strands of RH double helix DNA has been determined theoretically and experimentally.[104, 144] Concurrent simulations highlighted the conductance changes due to conformational perturbations.[159, 160] The dependency of these conformational perturbations on salt concentration suggests that counterion configurations around DNA play a prominent role in charge migration, especially in solutions with high salt concentration.[143, 147, 148, 161-163] Therefore, the ionic environment

around DNA has a significant influence on electrical measurements, but this information is unfortunately still missing. Systematic investigations into the correlations between the ionic conditions in buffer solutions and the subsequent physical conformational alteration induced conductance changes of DNA will provide further understanding of the nature of DNA, as well as providing essential groundwork for the development of DNA-based molecular devices.

Given that previous DNA conductance measurements were performed in buffer solutions containing fixed ionic concentrations, it is still unclear how the electronic properties of a short DNA molecule vary as the ionic environment changes, and what the underlying mechanism could be. Herein, we report conductance measurements of poly $d(GC)_4$ DNA based on a SPM break junction (SPM-BJ) technique (**Figure 5.1**). By gradually increasing the $MgCl_2$ concentration in the buffer solution, a decrease in conductance by two orders of magnitude was revealed. Circular dichroism (CD) measurements proved the reduction in the charge transport ability of short strand DNA to be a result of a secondary molecular structural transition. Combined with CD, we further developed a novel method to determine the transition degree (TD) and conductance simultaneously.

5.3 Experimental Details

Chemicals and materials Oligonucleotides treated with HPLC purification (purity>85%) were ordered from Integrated DNA Technology (IDT, Coralville, IA, USA). The single strand DNA sequences of two DNA duplexes used for conductance measurements are 5'-CGCGCGCG-3' and 5'-CGCGAAACGCG-3', both with thiol group modified at 3' end

respectively. Short strand (8 and 11 base pairs) of DNA molecules (5'-CGCGCGCG-3'and 5'-CGCGAAACGCG-3') was chosen because it has less possibility in structural bending and rolling. More importantly, SPM-BJ technique prefers highly conducting molecules. The increase in molecule length will exponentially decrease the conductivity of the molecule, which denies the choice of long DNA molecules. Sequence of poly $d(GC)_n$ was chosen for the fact that it can be easily transformed from one to another conformation under appropriate buffer condition, which makes it a commonly used sequence for DNA secondary structure variation study. Single strand DNA was stored in PBS (10mM phosphate, 100mM NaCl, pH 7.4) at -20˚C before use.

$MgCl_2$ was chosen to control counterion concentrations in buffer solutions. Although some other counterions like Na^+ and K^+ have been reported to successfully access DNA conformational variation, their relatively weak ionic strength,[154, 155] requesting a very high ionic concentration (>5M) to complete the variation for a short DNA duplex like ours, makes them inappropriate for precise electrical measurements at single-molecule level. Due to the high ionic strength of Mg^{2+} counterions, narrower concentration window is necessary to complete a full conformational transition, qualifying $MgCl_2$ a proper choice for our experiments. A series of different amounts of $MgCl^2$ was dissolved into PBS to produce buffer solutions with different $MgCl_2$ concentrations. Final sample solution at a specific concentration was obtained by adding single strand DNA to buffer solution with this concentration of $MgCl_2$. Then the sample solution was heated up to 90˚C in a water bath. Kept in dark, the solution temperature naturally dropped back to room temperature within 2hrs and the complementary duplex was formed. The concentration of DNA duplex is 3μM for all conductance

measurements. The melting temperature for both DNA sequences in solutions containing $MgCl_2$ concentrations within a range like ours is at least above 50˚C. And the higher the ionic concentration, the higher the melting temperature will be. As all electrical measurements were conducted under room temperature (~23˚C), it is hardly possible that the temperature of a single-molecule junction increased above this melting temperature even considering local heating effect.[164] Thus, we presume that the conductance measurements were mostly conducted for DNA duplexes.

The acquired DNA duplex sample solution was dropped on a freshly hydrogen flame annealed Au(111) surface for 40 min incubation. After the incubation, the conductance measurement was immediately performed.

STM imaging and electrical measurement setup STM imaging and conductance measurements were conducted in DNA solutions containing different concentrations of $MgCl_2$ by a PicoPlus SPM system (Molecular Imaging) with a PicoScan 3000 Controller (Molecular Imaging). Sheared gold wire with diameter of 0.25 mm (99.999%, Alfa Aesca) was used as a STM tip. To avoid ionic conduction, the STM tip was coated with Apiezon wax to keep ionic leakage current below 1pA. The obtained STM images were processed by WSxM software.[165]

The conductance measurement was carried out under 0.3V at room temperature (~23˚C) by SPM break junction technique (SPM-BJ). Upon this technique, the STM tip was initially driven by piezoelectric transducer (PZT) to approach the DNA duplex monolayer on Au substrate until the current reached a preset value which implied the formation of Au-DNA-Au junctions. Then the tip retracted so that current-distance trace was recorded simultaneously. For SHM SPMBJ, a 33 ms period of pause was set for

every 0.6 nm retracting distance in SHM so that steady molecular junctions were consequently generated. For both CSM and SHM, the tip kept retracting until every molecular junction was completely broken. This technique also guarantees that the single-molecule conductance was always measured at a junction conformation where a DNA molecule was approximately perpendicular to the surface right before the junction broke. It is possible that small amounts of DNA molecules might lay on the Au substrate before the junction was formed, although STM imaging suggested that most molecules were standing up on the surface. Conductance histograms were created from around 1000 individual conductance traces for each Mg^{2+} concentration. The first, most prominent peak in the histogram represents the conductance of a single DNA molecule in the break junction.

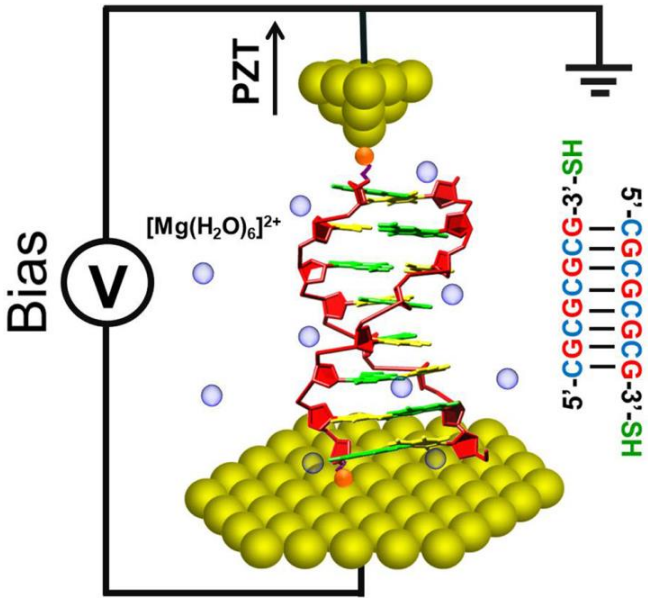

Figure 5.1 Experimental schematic of SPM break junction. $[Mg(H_2O)_6]^{2+}$ ions are represented by spheres around DNA skeleton. The three hydrogen bonds connecting cytosine and guanine are not shown in DNA structure. Reprinted from ref. 117.

As the experiment proceeds, water evaporates from the solution, which will increase the Mg^{2+} concentration in the solution. To avoid the influence from the increase of Mg^{2+} concentration on the final results, all the data were collected within one hour so that little variation in Mg^{2+} concentration in the solution was guaranteed.

Log-Scale: Conductance measurements using a log scale STM scanner was conducted in 1M $MgCl_2$ buffer solution where DNA molecules in multiple conformations could coexist. After choosing a flat area of DNA monolayer with the aid of imaging, conductance measurement was immediately performed under CSM. The retraction speed was 10nm/s. One set of data contained 122 traces and total ten sets of data were collected for histogram construction.

Linear-scale: Using a linear STM scanner, conductance measurements was applied at all $MgCl_2$ concentrations under both CSM and SHM. Since we applied two specific measurement regions: window 1 (1V/div) and 2 (50mV/div), data collecting for two windows at each concentration were performed by switching windows alternatively. It means we switched to window 2 for another set of data right after collecting one set of data under window 1, and then switched the scale back to 1V/div. By consecutively operating this way, the influence of concentration variation with measurement time going was minimized and data collected from two windows was under a relatively same condition. The tip retracting speed was 18nm/s. The retracting speed difference between the log and linear scanner was due to nothing but optimizing conductance measurement parameters. One set of data contained 122 traces and total ten sets of data were collected for histogram construction under either window. After analysis, each plateau contributed similar counts (~2000) to the histogram.

Circular dichroism (CD) measurement Setup CD measurement was performed by JASCO J-810. DNA concentration 5μM was used for significant CD signal. The preparation procedure of DNA samples was the same as conductance measurement except for DNA concentration difference. Each single CD spectra was plotted by averaging the results of three consecutive measurements in the corresponding sample solution.

5.4 Results and Discussions

Under a constant bias voltage of 0.3 V, the static conductance of poly $d(GC)_4$ DNA was measured in buffer solutions with various $MgCl_2$ concentrations (0 M, 0.1 M, 0.5 M, 1 M, 1.5 M, 2 M, 3 M and 4 M). The 3' end of single strand DNA was modified with a thiol group in order to form a bond with the Au electrodes to form the molecular junctions. The DNA sample solution prepared at each $MgCl_2$ concentration was dropped on freshly flamed Au(111) to form a DNA monolayer after 40 minutes of incubation. Molecular junctions were formed when the scanning tunneling microscope (STM) tip approached the Au surface, and then broke when the STM tip was retracted from the surface. During each tip retraction process, a conductance trace was recorded. By repeating this process, around 1000 conductance traces were collected for the construction of the final conductance histogram at each $MgCl_2$ concentration. All measurements were conducted at room temperature (~23˚C). A continuous-stretch mode (CSM) SPM-BJ was performed for transient Au–DNA–Au junctions by retracting the tip continuously,[31] and a stretch-hold mode (SHM) SPMBJ was applied to create stable junctions by modifying the tip retraction process with a periodic pause.[56]

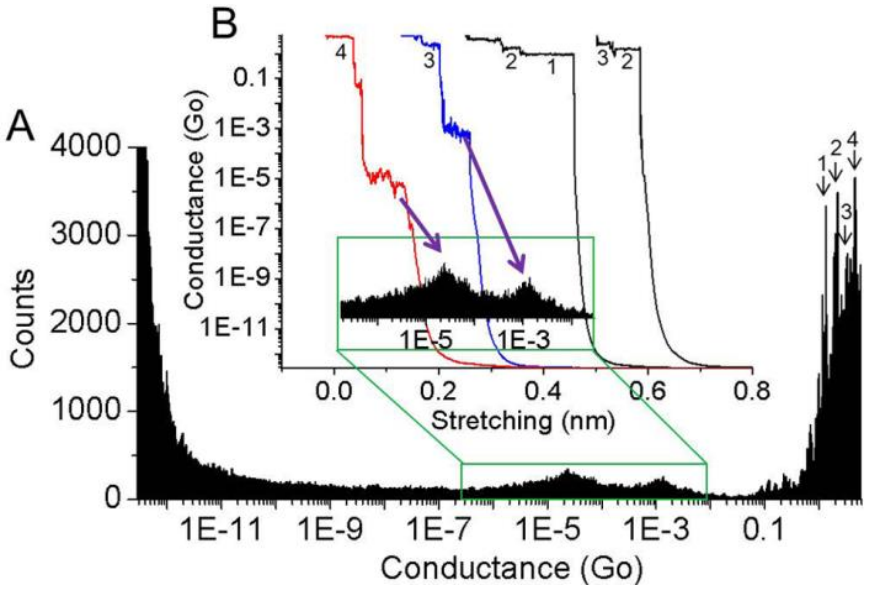

Figure 5.2 Log-scale conductance measurement was performed in 1M $MgCl_2$ solution using CSM-SPMBJ. (A) Log scale conductance histogram was constructed from around 1000 log-scale traces under CSM. (B) Typical conductance traces were shown. The left two traces exhibited plateaus corresponding to peaks at around $1\times10^{-5}G_0$ and $1\times10^{-3}G_0$, respectively. Numbers labelled in conductance histograms and traces represent integer multiples of conductance quantum G_0. The inset in B shows the zoom in of squared area in log-scale conductance histogram. Reprinted from ref. 117.

A logarithmic-scale STM scanner was first applied under CSM to monitor a broad range for a first glance at the possible conductance sets of poly $d(GC)_4$ DNA in 1 M $MgCl_2$ buffer solution, which is supposed to simultaneously access various DNA conformations. In addition to the sharp peaks at integer multiples of the conductance quantum G_0, which correspond to the gold quantum contacts, the histogram also exhibited two apparent peaks at lower conductance: at around $1\times10^{-5}G_0$ and $1\times10^{-3}G_0$, respectively (**Figure 5.2**). Representative log-scale conductance traces are shown in **Figure 5.2B**. Previous measurements on the same DNA sequence confirmed the peak at

$1\times10^{-3}G_0$ to be the conductance in a standard double helix B-conformation.[104] Log-scale data offered a complete view of the possible locations of conductance peaks, but failed to provide the highest resolution of details which is necessary for electrical measurements at the single-molecule level. In order to accurately determine the conductance value and gain more details of the DNA molecular junction, a linear-scale STM scanner was then used for a series of different $MgCl_2$ concentrations under both CSM- and SHM-SPMBJ. To measure the conductance at $\sim1\times10^{-3}G_0$, we chose the measurement window in the higher conductance region (**Figure 5.3A**). As is shown in **Figure 5.3A**, a representative conductance trace (the rightmost) contains a very low plateau at the same level of baseline offset shift. Unfortunately, this information was entirely washed out by slight shifting of the conductance trace baseline under this window. To reveal the lower conductance plateau, we measured the conductance curves by focusing on the lower conductance region, which show a conductance of $\sim 3\times10^{-5}G_0$ (**Figure 5.3B**). Therefore, using SHM-SPMBJ measurements, two peaks were accurately measured to be $1.06(\pm0.27)\times10^{-3}G_0$ and $2.79(\pm0.64)\times10^{-5}G_0$ in 1M $MgCl_2$ solution, respectively. We then measured the conductance of the poly $d(GC)_4$ DNA under different $MgCl_2$ concentrations. For lower concentrations (0M, 0.1M, 0.5M), a conductance peak around $1\times10^{-3}G_0$ was determined, suggesting the DNA to be B-DNA. However for medium and high concentrations (1M ~ 4M), a larger number of individual conductance traces appeared to have significant information at a much lower conductance value which was associated with the peak at around $1\times10^{-5}G_0$ under log scale. Control experiments conducted in pure 4M $MgCl_2$ solution with no DNA molecule implies that these peaks were dominantly contributed by DNA molecules rather than other factors like courterions

and water molecules in the solution. A two-dimensional correlation histogram (2DCH) was also demonstrated for the two measurement regions. Strong anti-correlation regions (circled area) suggest the possibility that each conductance trace contained only a single conductance plateau, either at the height of one, or at two Au-DNA-Au junctions, but rarely both together.

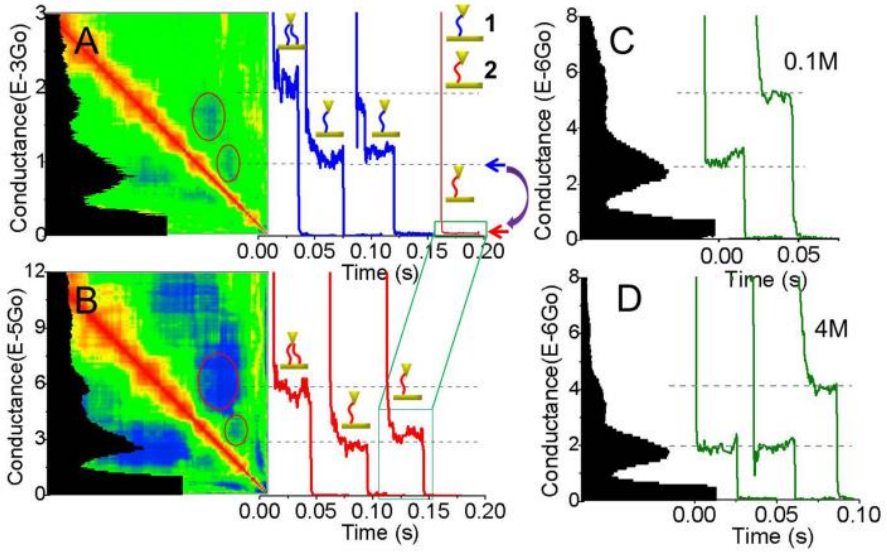

Figure 5.3 (A) and (B) show the conductance measurement results of poly d(GC)$_4$ DNA. In 1M $MgCl_2$ solution, two sets of conductance values ($1\times10^{-3}G_0$ in A and $1\times10^{-5}G_0$ in B) were determined by conductance histograms using the measured conductance traces. In A and B, the rough schematics (1 and 2) of DNA molecular junctions are shown above the each conductance plateau. Short curved strand in blue and red represent the DNA molecules with high and low conductance, respectively. The number of short curved strand in each schematic represents how many DNA molecules were measured when the plateau was recorded. 2DCH show strong anti-correlation regions (circled in 2DCH). For 5'-CGCGAAACGCG-3'DNA, SHM conductance histograms, typical conductance traces measured at 0.1M and 4M are shown in panel C and D, respectively. Reprinted from ref. 117.

While the $1\times10^{-3}G_0$ conductance value was reported to be associated with B-DNA, the appearance of the conductance peak at the level of $1\times10^{-5}G_0$ could be attributed to several possible causes. Firstly, both base pair (bp) mismatch and the single strand DNA could be its source. As poly $d(GC)_4$ is the chosen sequence, there would be multiple mismatched bps once the bp mismatch took place. However, even the mismatch of a single bp leads to one order of magnitude decrease in conductance so that multiple mismatches will make the DNA nearly insulating,[166] which suggests the impossibility in observation of the conductance of the mismatched DNA molecules. Also, in our case, single strand DNA hardly existed due to the high melting temperature (>50˚C) of DNA molecules in 1M $MgCl_2$ solution. Even if it existed, the single strand DNA could not form the molecular junction since only one end of the single strand was modified with a thiol group. Thus, the peak at the level of $1\times10^{-5}G_0$ is not resulted from single strand DNA or bp mismatch. Secondly, as many studies reported, variations in Au-S geometries, effective contact coupling and DNA solvation shell could also cause the decrease in conductance by orders of magnitude.[67, 167-169] To find out if these factors caused the conductance drop, another series of control experiments were conducted on the DNA sequence of 5'-CGCGAAACGCG-3' which has little perturbation in structure due to the three consecutive adenine bases sandwiched at the center of the sequence.[170, 171] In **Figure 5.4C**, CD results suggested that this DNA still remained in RH B-conformation even after addition of high concentrations of $MgCl_2$. Under SHM, conductance of this DNA sequence was measured in $MgCl_2$ solutions prepared the same way as for poly $d(GC)_4$ DNA. As shown in **Figure 5.3C and 5.3D**, the conductance only showed a negligible variation from around $2.5\times10^{-6}G_0$ in 0.1M $MgCl_2$ solution to $2.0\times10^{-6}G_0$ in

4M $MgCl_2$ solution. This small change is possibly caused by a slight structural perturbation of DNA in solutions with high $MgCl_2$ concentration confirmed by the CD measurements (**Figure 5.4C**). No significant number of conductance traces containing low but meaningful plateaus like the case for poly $d(GC)_4$ DNA was observed with $MgCl_2$ concentrations spanning from 0M to 4M in the control measurements. Overall, both conductance measurements and CD results suggest that the influences of contact geometries, effective coupling and solvation shell were trivial in this study. Finally, the newly revealed peak, two orders of magnitude smaller in conductance, could be contributed by another conformation of the poly $d(GC)_4$ DNA duplex.

Over a series of measurements, it was determined that the histogram peak at $1.06(\pm 0.27) \times 10^{-3}G_0$ did not have obvious change with small increases of Mg^{2+} concentration from 0M, 0.1M and 0.5M, even over the entire range of concentrations from 0M to 4M. Instead, the magnitude of this peak decreased with increasing Mg^{2+} concentration, while the magnitude of the other peak at $2.79(\pm 0.64) \times 10^{-5}G_0$ became more pronounced. This implies a clear ratio switch between these two peaks as Mg^{2+} concentration increases. The change in magnitude of two orders suggests not a linear relationship between DNA conductance and counterion concentration, but a significant regime change such as a compete change in DNA conformation.

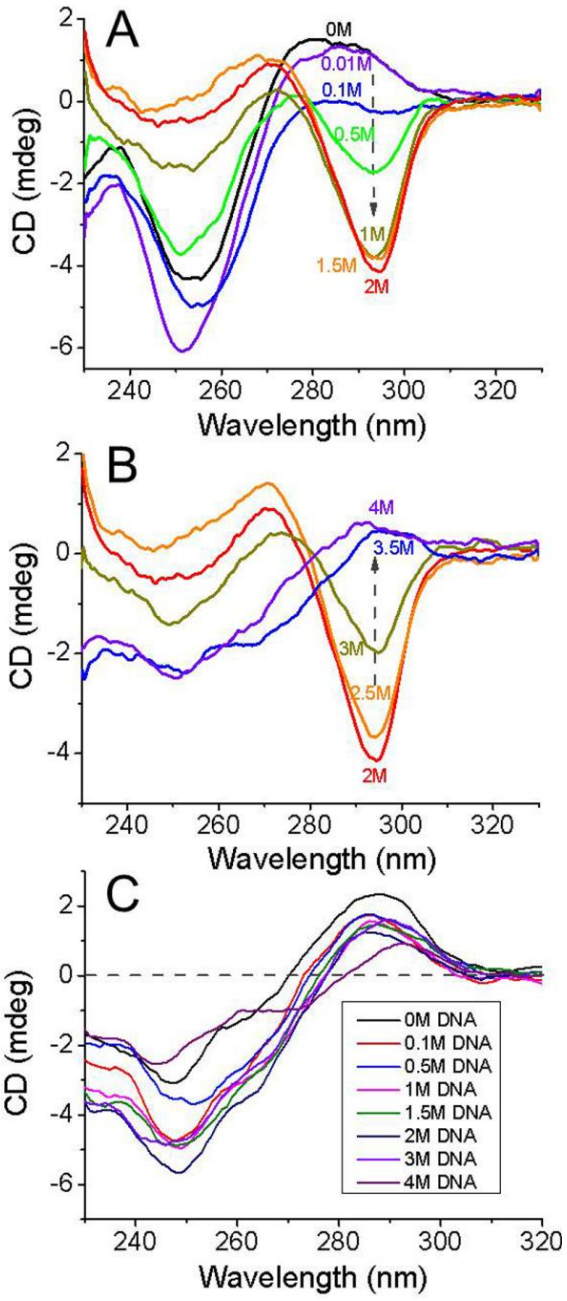

Figure 5.4 (A) and (B) show the CD spectra of poly d(GC)$_4$ DNA measured in 0M~2M and 2M ~4M $MgCl_2$ solutions, respectively. The arrow in either panel shows the variation trend of CD intensity at 295nm as $MgCl_2$ concentration increases. Panel C illustrates the CD spectra of 5'-CGCGAAACGCG-3'DNA measured in 0~4M $MgCl_2$ solutions. Reprinted from ref. 117.

A likely explanation is a change from RH B-DNA to LH Z-DNA, which can be tested by CD measurements, since CD studies[154, 172] have thoroughly explored the ion-dependent transition between B- and Z-DNA. Therefore, we conducted CD measurements on DNA samples under the same $MgCl_2$ concentrations as the conductance measurements, and also two additional concentrations of 0.01 M and 3.5 M. **Figure 5.4A** (concentrations from 0 M to 2 M) shows the complete transition from B-DNA spectra (a positive peak at 275 nm and a negative peak at 250 nm) to Z-DNA spectra (a negative peak at 295 nm and a positive peak at 265 nm), similar to other reports.[154, 172, 173] An unexpected inconsistency in CD trend was observed in concentrations beyond 2 M (**Figure 5.4B**). Negative peaks of increasingly lower intensity were observed at 295 nm, until the peaks eventually became a small bump at very high $MgCl_2$ concentrations (3.5 M and 4 M). We suggest that aggregation of individual DNA molecules was the cause of this odd trend at very high $MgCl_2$ concentrations (3.5 M, 4 M), because high Mg^{2+} concentrations can readily induce the aggregation of short DNA molecules, and the spectra at 3.5 M and 4 M resemble curves associated with ψ-form DNA condensations.[174-177]

To confirm this, STM imaging was carried out on samples prepared in the same way as for CD measurements (**Figure 5.5**). At 0.1 M, a well-assembled monolayer of DNA molecules was observed. After drying the solution with high purity nitrogen, imaging in air showed a negligible aggregation spot in only one of a few images, which may be due to the high concentration (5 mM) of DNA molecules. In 4 M $MgCl_2$ solution, imaging in solution showed lots of aggregation spots in all images. The imaging in air showed even more aggregation spots, because drying the sample forced floating

aggregation bundles which could not be seen in solution to attach to the surface. A control experiment conducted in pure 4 M $MgCl_2$ solution with no DNA molecules revealed no aggregation spots via both imaging in solution and in air, which excludes the possibility that these spots were induced by condensation of salt.

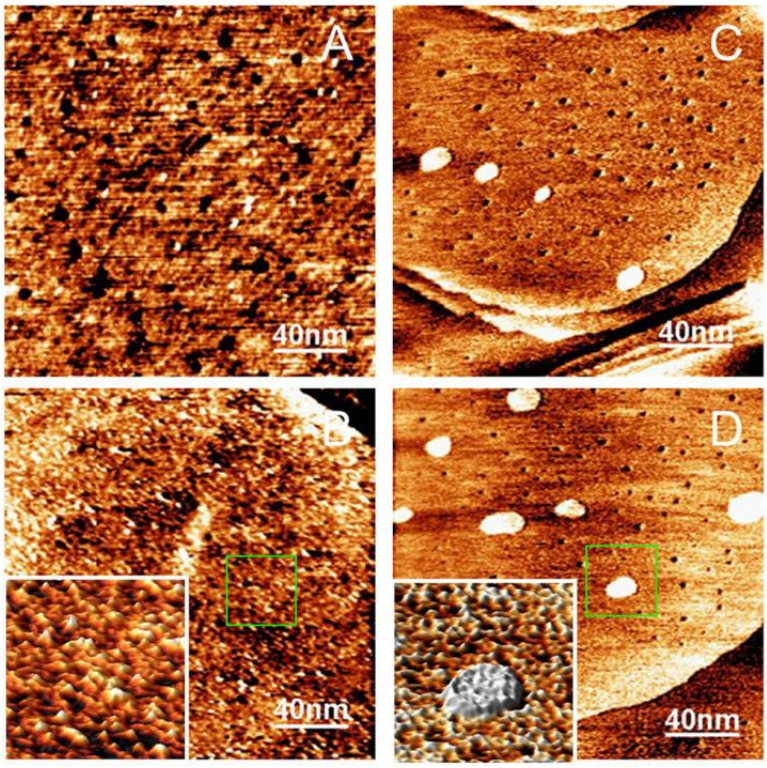

Figure 5.5 STM imaging for DNA samples in 0.1M (A, C) and 4M (B, D). Panel A and B are images scanned in solution under 0.1M and 4M, respectively. Panel C and D show the images obtained in air under 0.1M and 4M, respectively. Reprinted from ref. 117.

It has to be noted that the buffer pH decreased as the $MgCl_2$ concentration increased. Previous CD studies using the same DNA sequence proved that low pH (<3.6) could also contribute to the B–Z conformational transition.[178, 179] Therefore, other than the high ionic concentration, the low pH of the buffer solution is another factor inducing the B–Z transition when the $MgCl_2$ concentration was high (>3 M). The exact

concentration of $MgCl_2$ dissolved in buffer solution decreased as the buffer pH reduced. Given that it is hard to know the exact concentration, we continue using the concentration labelled when we prepared the solution in the following discussion.

Due to DNA aggregation, CD failed to distinguish Z-DNA at high $MgCl_2$ concentrations; however the conductance measurement has little difficulty handling aggregation because STM can image prior to conductance measurements. Before measuring, smooth locations indicative of a DNA monolayer on the Au surface were chosen to conduct measurements. The Au surface itself contributed to breaking up aggregates, and any aggregates floating in solution would not have influenced the conductance measurements, and certainly would not have contributed to histogram peaks.

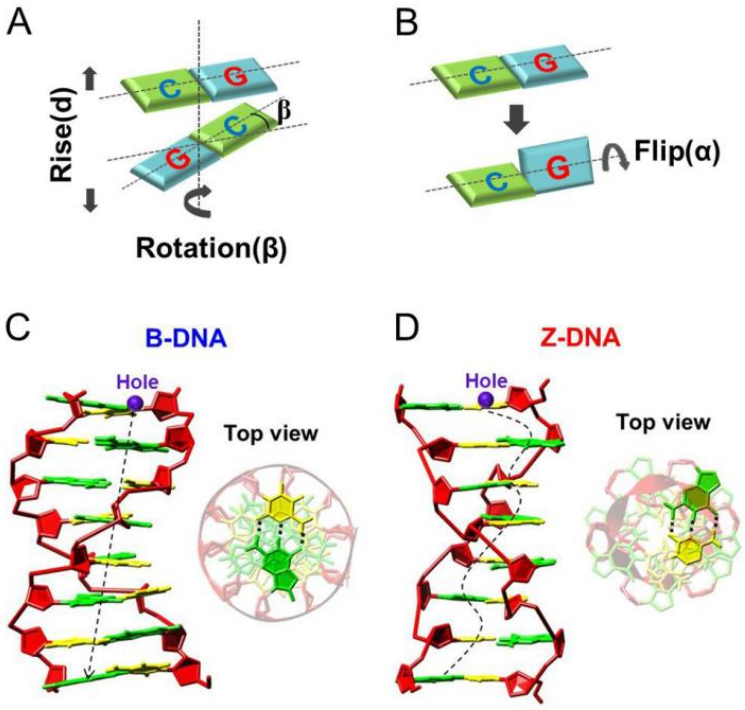

Figure 5.6 (A) Schematics of relative change between neighboring bps during the B-Z transition; (B) The schematic for guanine flipping. (C) and (D) show the structural side view and top view of B- and Z-DNA, respectively. In (C) and (D), the dashed lines demonstrates the intra-strand path for hole migration. Reprinted from ref. 117.

The cause of conductance decrease from B- to Z-DNA

The cause of the decrease in DNA conductance during B–Z conformational transition may come from a few sources, but is primarily due to the structural change induced breaking of π-π orbital stacking between neighboring bps. In **Figure 5.6A**, the average rise (d) between adjacent bps was increased by 14% from 0.332 nm (in B-DNA) to 0.380 nm (in Z-DNA), which could rapidly reduce the charge transfer rate; the axial twist (b) in Z-DNA was determined to be -30˚, which is very different from the 36˚ angle for the highest charge transport in B-DNA. Most importantly, the transition results in a flipping of guanine (G) bases by almost 180˚ for this DNA sequence (**Figure 5.6B**).[160] The alternating *anti* and *syn* orientations transform the location of G bases from the center of the helix in B-DNA to the edge of the helix in Z-DNA. These changes cause the bases to be held on the edge of the helix, and place guanine bases over the neighboring cytosine's sugar residues. The result is a disruption of the ordered π-π stacking, which is the major source of the relatively high conductance of B-DNA (**Figure 5.6C and 5.6D**).[143, 180] Although the diameter of Z-DNA is narrower, charge transport along neighboring bps is much easier longitudinally than laterally, and the broken stacking, increased rise and spiral intra-strand path result in a significant reduction in conductance on going from B- to Z-DNA.[181] Since the HOMO is dominated by G orbitals in sequences such as this,[144] the flipping of G will have a detrimental effect on distribution of effective orbitals for charge transport. According to the possible backbone conduction model,[182] the contorted “zigzag” backbone in Z-DNA is less favorable than the standard double helix in B-DNA, thereby lowering the conductance.

Apart from the impact of intrinsic structural change in DNA, the surrounding counter ions and water molecules also affect the charge transport process. It was reported that Mg^{2+} could bind to G and phosphate through its hydration shell.[183] Estimations based on our case show that there are on average 0.8 Mg^{2+} ions around a single DNA junction in 0.1 M $MgCl_2$ solution. But an average of 8.0 Mg^{2+} ions are available to bind to a single DNA molecule at 1 M, and even more ions are possible as the concentration increases. It has to be noted that the dynamic movement of Mg^{2+} ions in solution greatly lowers the binding opportunity between the ions and DNA. Thus, it is plausible that higher concentrations (3 M, 4 M) are necessary to stabilize most DNA molecules in the Z-form.

Simulations[147] have suggested the delocalization of electron states induced by hydrated ions around DNA. Extra pathways for charge hopping could occur via ionization of phosphates and the doping of DNA grooves by Mg^{2+}, water states and base states.[184, 185] Compared with the breaking of π-π orbital stacking, the influence of water and counter ions are presumed to be minor.

Transition degree (TD)

To quantify this DNA conformational change, we calculated the transition degree (TD), defined as the percentage of B-DNA which is converted to Z-DNA, as determined by our SHM conductance measurements. As an analogue to CD reported by others,[154] the key feature of our conductance histograms which allows the distinction between B- and Z-DNA is the two separate peaks. The SHM SPM-BJ technique predicts that each plateau in every conductance trace is ideally equal in counts due to the constant duration, though the position changes. Therefore, each SHM conductance trace contributed equally to the final conductance histogram. Thus, the histogram is composed of a finite number of

equally sized plateaus, the position of which is concentration dependent. By constructing histograms from two separate sets of traces, the transition degree was determined as SHM-TD=$A_Z/(A_Z+A_B)$, where A is the sum of counts beneath the first peak area in the SHM histograms.

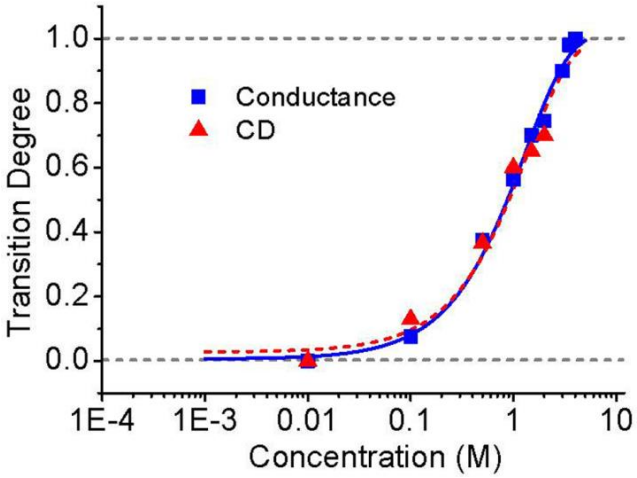

Figure 5.7 TD vs log $MgCl_2$ concentration. SHM-TD data points (■) and its corresponding Boltzmann fitting (solid curve). CD-TD data points (▲) and its fitting (dashed curve). Reprinted from ref. 117.

To accurately mark the transition midpoint, where 50% of BDNA was converted into Z-DNA, it is important to first note that at low concentrations (0.1 M), past research has agreed the conformation is predominantly B-DNA. The Boltzmann fitting on the SHM-TD data (squares in **Figure 5.7**) suggested the transition midpoint to be 0.93 M. This was larger than the previously reported value of around 0.66 M for indeterminately long strands of poly $d(GC)_m$ in $MgCl_2$ solution using CD.[154] But it matched well with the trend reported in the same paper, that the shorter the DNA length, the larger the concentration required to induce a 50% transition. Due to the sensitivity our electrical measurement has to high ionic concentration, we were unable to obtain meaningful

results beyond 4 M. Similarly, the Boltzmann fitting suggests that the B – Z transition was saturated at around 4 M. Using the well-behaved part (0 ~ 2M) of the CD results (triangles), we also plotted a CD-TD trend line (dashed curve). Boltzmann fitting was still suitable for estimating an entire transition line based on these CD results. It suggested a transition midpoint (0.91 M) very close to the SHM-TD result. The SHM- and CD-TD trend lines overlap reasonably well.

5.5 Conclusion

Based on the SPMBJ technique, by increasing the concentration of $MgCl_2$ in the buffer solution, two different DNA conformations (B and Z) were distinguished exclusively by their difference in conductance due to the physical and electronic differences between the two conformations. Experimental results revealed that the increase of ionic concentration in a DNA sample solution induced a secondary structure transition of DNA molecules, and the conformational change reduced the DNA conductance by two orders of magnitude. Our technique successfully monitored changes in DNA conformation at a spatial and temporal resolution never before achieved, providing a powerful tool to explore some of the more confounding problems in molecular biology. In addition, using a SHM modification, our method offers an alternative way to build up transition trend lines between two DNA conformations, particularly when CD fails to work. This method is a general tool for studying transitions of other molecular properties associated with conductance differences.

CHAPTER 6

MOLECULAR RECTIFIER COMPOSED OF DNA WITH HIGH RECTIFICATION RATIO BY INTERCALATION

❖ [38] C.L. Guo*, K. Wang*, E. Zerah-Harush, J. Hamill, B. Wang, Y. Dubi, B.Q. Xu, Nature Chemistry, 8, 484-490. (*equal contribution). Reprinted here with permission of publisher.

6.1 Abstract

The predictability, diversity and programmability of DNA make it a leading candidate for the design of functional electronic devices that use single molecules, yet its electron transport properties have not been fully elucidated. This is primarily because of a poor understanding of how the structure of DNA determines its electron transport. Here, we demonstrate a DNA-based molecular rectifier constructed by site-specific intercalation of small molecules (coralyne) into a custom-designed 11-base-pair DNA duplex. Measured current–voltage curves of the DNA–coralyne molecular junction show unexpectedly large rectification with a rectification ratio of about 15 at 1.1 V, a counter-intuitive finding considering the seemingly symmetrical molecular structure of the junction. A non-equilibrium Green's function-based model—parameterized by density functional theory calculations—revealed that the coralyne-induced spatial asymmetry in the electron state distribution caused the observed rectification. This inherent asymmetry leads to changes in the coupling of the molecular HOMO−1 level to the electrodes when an external voltage is applied, resulting in an asymmetric change in transmission.

6.2 Introduction

The field of molecular electronics, the goal of which is to functionally incorporate molecular components in electronic devices[8, 17, 62], has focused intensively on DNA. In addition to the molecule's high density of genetic information, its inherent structural and molecular recognition properties render it ideal for molecular electronics applications. In the past two decades DNA has therefore attracted inordinate amounts of attention in the

molecular electronics and spintronics fields[186-188] for its potential to transport charge in molecular electronics applications such as DNA chips[141, 144].

Shown to be sequence-dependent, the conduction mechanism of native duplex DNA was found to be dominated by tunneling when the guanine–cytosine (G–C) pairs are separated by three or fewer adenine–thymine (A–T) pairs. If the number of A–T pairs is increased, however, diffusive hopping becomes the main electronic transport mechanism[189, 190]. To further complicate matters, researchers recently demonstrated that DNA charge transport includes an intermediate tunneling–hopping regime[191]. Achieving the goal of obtaining a functional electronic device based on DNA will thus require that its molecular structure be altered to obtain non-monotonic I–V behavior. The conductivity of DNA was recently found to be sensitive to subtle changes in DNA conformation caused by alterations in the ionic environment[117] or by its modification with methylation[192, 193] or with metal ions[194, 195]. Remarkable in their own right, these achievements hint at the tantalizing possibility that the electronic transport properties of DNA can be fine-tuned via structural modification for the development of a diversity of DNA-based electronic devices, especially an applicable DNA molecular rectifier.

First proposed by Aviram and Ratner in 1974,[5] the notion of a molecular rectifier continues to be a subject of intense interest in the field of molecular electronics. To date, using conductance measuring methods based on self-assembled monolayers[133, 140] and single-molecule junctions[40, 118, 196], rectification can be observed either with asymmetric molecules[119, 197] or with inconsistent molecule–electrode contacts[100]. Most rectifications have been observed using small organic molecules, the structures of which usually

comprise electron-donor and electron-acceptor groups separated by an insulating group[119, 140].

Here, we report the successful creation of a DNA-based rectifier, accomplished by intercalating coralyne molecules into specifically designed duplex DNA. Electrical measurements of single DNA–coralyne complex molecular junctions made using the scanning tunneling microscopy break junction (STM-BJ) technique[31, 56] (**Figure 6.1A**) unexpectedly revealed rectification with a high rectification ratio of around 15 at 1.1 V, a completely counter-intuitive finding in light of the apparent structural symmetry of the DNA–coralyne complex. Non-equilibrium Green's function (NEGF) calculations of a coherent, tight-bonding model based on density functional theory (DFT) suggested that the rectification behavior was caused mainly by the coralyne-induced local spatial asymmetry of the distribution of electron states along the DNA chain, which, in turn, leads to an asymmetric change in the transmission function associated with the second highest occupied molecular orbital (HOMO−1).

6.3 Experimental Details

Chemicals and Materials Oligonucleotides were ordered from Integrated DNA Technology (IDT, Coralville, IA, USA) with 3'-thiol linkers. DNA sequences for measurement were 5'-CGC GAA ACG CG-3' (DNA(A)) and 5'-CGC GTT TCG CG-3' (DNA(T)), respectively. DNA sequence 5'-CGC GCG CG-3' (poly $d(CG)_4$) was also measured as complementary study. Coralyne chloride was purchased from Sigma-Aldrich (St. Louis, MO, USA) and dissolved in water before use. DNA was stored in PBS (10 mM phosphate, 100 mM NaCl, pH 7.4) at -20 ˚C. The concentrations of DNA and

coralyne were determined by UV-Vis spectroscopy with the corresponding extinction coefficients: DNA(A), ε_{260} = 105 500 M-1 cm -1; DNA(T), ε_{260} = 94 200 $M^{-1}cm^{-1}$; coralyne chloride, ε_{420} = 14 500 $M^{-1}cm^{-1}$. Absorption spectra were recorded on a UV-1700 spectrophotometer (Shimadzu Scientific Instruments). Circular dichroism (CD) was measured at 25 °C on Chirascan spectrometer with 1 mm optical-path quartz cuvette.

DNA–coralyne complex sample preparation The DNA–coralyne complex was prepared by mixing equivalent amounts of DNA (5′-CGCGAAACGCG-3′-SH) and coralyne in PBS. The DNA–coralyne mixture was heated to 80 °C in a water bath and allowed to return slowly to room temperature for annealing and formation of the DNA–coralyne complex. The final concentration of DNA–coralyne complex used in subsequent electrical measurements was 3 μM. As a control, the complementary duplex DNA was prepared in the same concentration using identical methods. Once the DNA–coralyne complex was acquired, it was applied to a freshly annealed Au(111) surface to form a self-assembled monolayer. Immediately after 40 min incubation, the samples were measured. The Au substrate was made by thermally evaporating an Au layer (thickness of ∼100 nm) on a freshly cleaved mica surface. Before using the Au substrate, it was annealed by hydrogen flame to form a Au(111) surface.

Molecular junction formation and electrical measurements Electrical measurements were performed in PBS buffer on a PicoPlus SPM system (Molecular Imaging) with a PicoScan 3000 controller (Molecular Imaging). Sheared gold wire with a diameter of 0.25 mm (99.999%, Alfa Aesca) coated with wax was used as an STM tip. The measurements were carried out with both CS-SPMBJ and SH-SPMBJ. For CS-STMBJ, the STM tip was first driven by a piezoelectric transducer (PZT) close to the DNA–

coralyne complex monolayer on the Au surface until the current reached a preset value, which indicated that the Au–DNA–Au junctions had formed. Subsequently, a current–distance trace was recorded while simultaneously retracting the STM tip. Typically, 1,000–2,000 traces were collected for a given experimental condition at a retrace rate of 24–30 nm/s. For SH-STMBJ, the retraction was divided into two processes: abrupt stretching and free holding of the molecular junctions by withdrawing the STM tip by ~0.6 nm and then holding it stably in position for 25 ms. The stretching–holding processes, which were controlled by a homemade LabView computer program, were alternately implemented until the molecular junctions were completely broken. The current–distance traces were measured at different biases using these two different techniques to study the electrical properties of the DNA–coralyne complex. In the present system, the external bias was applied on the substrate with the tip grounded.

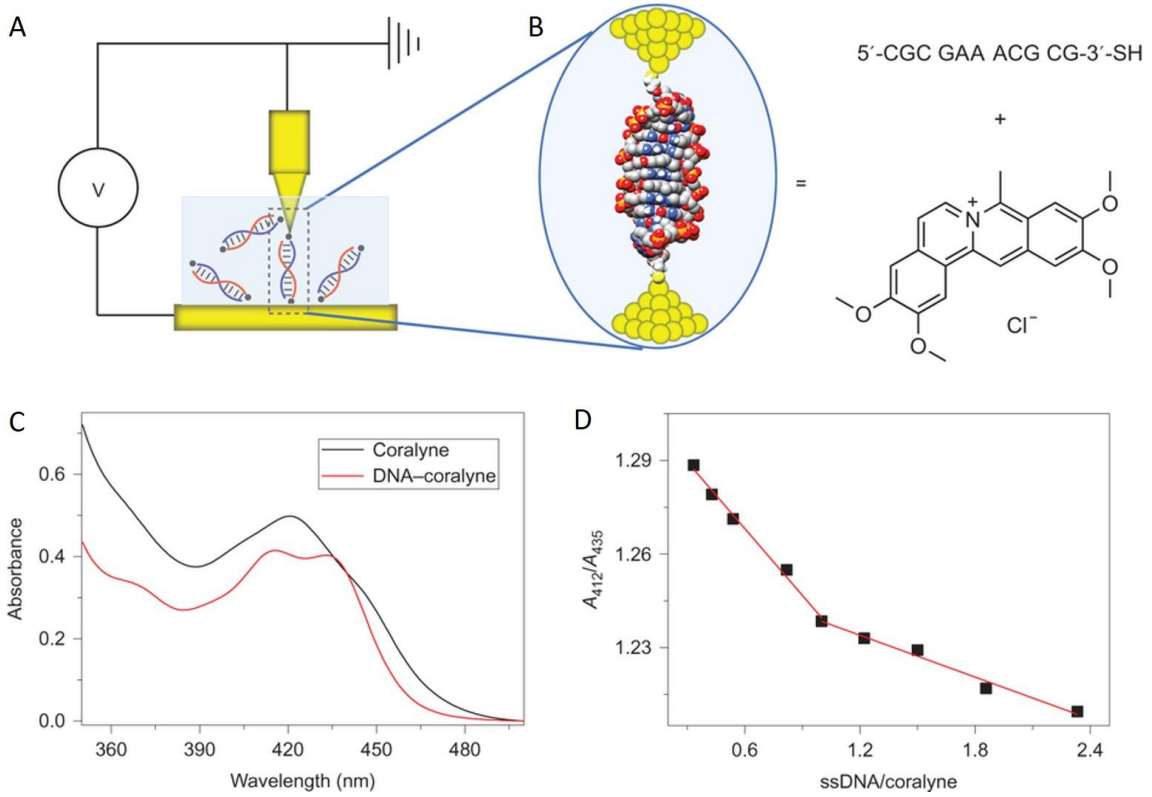

Figure 6.1 (A) Schematic of the STMBJ system. The single-molecule junction is formed in the region indicated by the dashed box. (B) Molecular junction composed of the DNA–coralyne complex (magnified view of the dashed box in A). The DNA–coralyne complex is formed with a coralyne molecule and a sample DNA molecule (5′-CGCGAAACGCG-3′-SH). (C) UV–vis absorbance spectra of coralyne alone (black) and coralyne in the presence of DNA (red). The ratio of ssDNA to coralyne is 1. After adding DNA to a coralyne solution, the single absorption peak of coralyne at 420 nm splits into two peaks at 412 and 435 nm, indicating the intercalation of coralyne into native DNA. (D) Job plot of DNA with coralyne, in which an inflection point of 1 is observed, indicating that two coralyne molecules have been inserted into the formed DNA duplex. ssDNA/coralyne (horizontal axis) represents the concentration ratio of ssDNA to coralyne. The total concentration of coralyne and ssDNA remained unchanged (at 10 μM) during the entire titration.A_{412}/A_{435} (vertical axis) is the absorption ratio of coralyne at 412 nm versus 435 nm. Sample conditions for UV–vis absorption were 10 mM phosphate, 100 mM NaCl, pH 7.4. Reprinted from ref. 38.

6.4 Results and Discussions

Coralyne is a small, planar molecule that has been shown to specifically intercalate in poly (dA) and strongly bind with adenine–adenine (A–A) base pair mismatches[198-200]. Given the π conjugation nature of coralyne, its intercalation in native DNA is expected to perturb the π–π stacking interaction between the neighboring bases of DNA strands, thereby modulating electron transport through the treated DNA molecule. We prepared the DNA–coralyne complex by specifically intercalating two coralyne molecules into a custom-designed 11-base-pair (bp) DNA molecule (5′-CGCGAAACGCG-3′) containing three mismatched A–A base pairs at the center (**Figure 6.1b**). UV–vis spectroscopy shows that the addition of the DNA molecules to the

coralyne alters the UV–vis absorption of the latter; instead of a single maximum at 420 nm, the DNA–coralyne complex has two local maxima of 412 nm and 435 nm, an indication that the coralyne is intercalated between the adenine bases (**Figure 6.1C**)[199]. The results of continuous fraction analysis (Job plot, **Figure 6.1D**), in which an inflection point of 1 was obtained for the single-stranded (ss) DNA to coralyne concentration ratio, indicate that two coralyne molecules were inserted into one formed DNA duplex. Further confirmation of this outcome was provided by structural and energy simulations as well as a circular dichroism (CD) spectrum, which showed that the most stable complex structure was symmetric and composed of B-form DNA with two coralyne molecules inserted. Temperature-dependent ultraviolet and CD measurements prove that the DNA–coralyne complex is stable at room temperature. The DNA molecules used in this study were thiolated at their 3′ ends to facilitate their contact with the Au(111) surface via a Au–S bond. Before electrical measurements, the morphologies of the native duplex DNA and of the DNA–coralyne complex on an Au (111) surface in PBS solution were studied using STM imaging. The electronic transport properties of the DNA–coralyne complex were then measured and compared with those of the native duplex DNA using STM-BJ techniques.

Conductance behavior of DNA–coralyne complex molecular junctions

Static differential conductance measurements of single DNA–coralyne complex molecular junctions were first performed under different bias voltages using STMBJ either in the continuous-stretching (CS) mode to form transient junctions or under the stretching–holding (SH) approach to form stabilized junctions. Both techniques have been detailed elsewhere[31, 56]. Using CS-STMBJ, we generated conductance histograms

comprising 1,000–2,000 differential conductance traces. The first and second peaks obtained in the histogram correspond to one and two molecules trapped in measured junctions, respectively. Therefore, the conductance of native duplex DNA was $G = 2.69\times10^{-6}G_0$ under a bias of 0.3 V (**Figure 6.2A**) and $G = 3.30\times10^{-6}G_0$ under a bias of −0.9 V (**Figure 6.2B**), where $G_0 = 2e^2/h = 77.4$ μS (e is the electron charge and h is Planck's constant). Repeating the conductance measurements for the DNA–coralyne complex using the same method and the same bias voltage of 0.3 V showed that its conductance was $3.17\times10^{-6}G_0$ (**Figure 6.2C**), that is, very close to that of the duplex DNA. However, under higher bias values, the conductance measurements of native DNA diverged from those of the DNA–coralyne complex, especially when under negative bias conditions. For example, at a bias of −0.9 V, the conductance of the DNA–coralyne complex was $10.77\times10^{-6}G_0$ (**Figure 6.2D**), which is three times that of the native DNA ($3.30\times10^{-6}G_0$) (**Figure 6.2B**). This striking phenomenon was also observed using the SH-STMBJ technique.

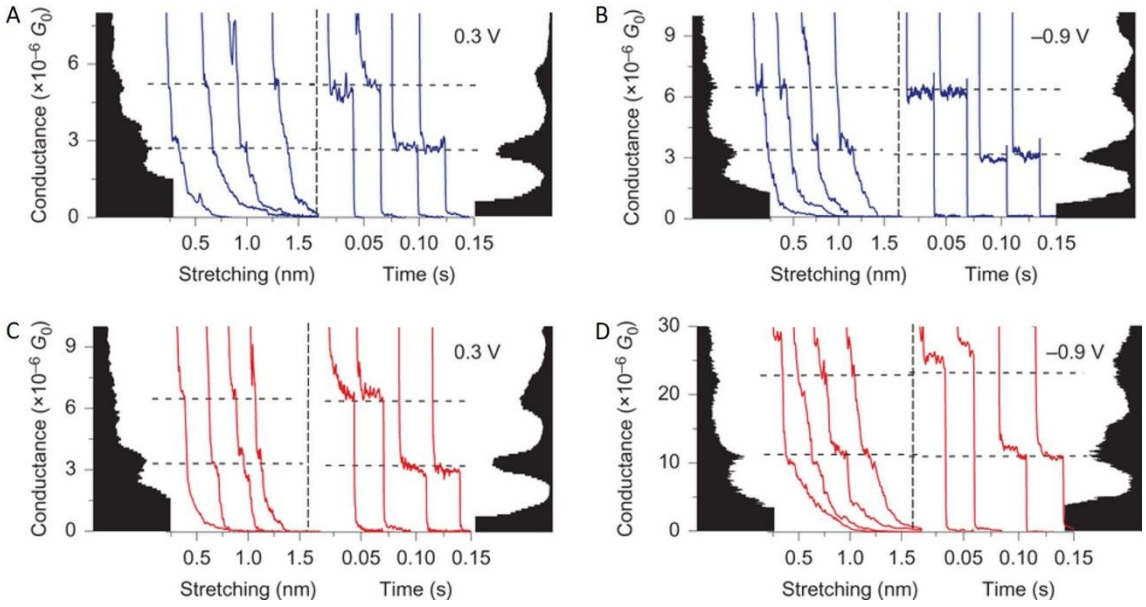

Figure 6.2 (A-D) Native DNA (A,B) and DNA–coralyne complex (C,D) were measured with both CS-STMBJ and SH-STMBJ techniques under 0.3 V (A,C) and −0.9 V (B,D). A conductance histogram and typical conductance traces obtained using both the CS-STMBJ and SH-STMBJ methods are shown to the left and right of the middle dashed line, respectively. All histograms were constructed from 1,000–2,000 traces. Note that under −0.9 V, the conductance of the DNA–coralyne complex is three times that of the native DNA, although they do not show a significant difference under 0.3 V. Reprinted from ref. 38.

To elucidate the variable conductance behavior of the DNA–coralyne complex under different bias voltages, we carried out I–V measurements of native DNA and of the DNA–coralyne complex by continuously sweeping the bias voltages (−1.1 to 1.1 V) across single junctions stabilized by the free-holding action of the SH-STMBJ technique[56]. The I–V evaluation of native DNA revealed symmetrical current behavior under opposite bias polarities (Fig. 3a). In stark contrast, the DNA–coralyne complex exhibited decidedly asymmetrical I–V behavior, with a sharp increase in current under negative bias. The inset in Fig. 3a is a graph overlay of the continuously measured I–V curves and the static current measured under different bias voltages. Compared with directly measured I–V characteristics, the static current, obtained here by statistically averaging over a large number of molecular junctions, may obscure some of the detail revealed by the direct I–V measurements. However, the I–V characteristics obtained using either of the two methods agreed well with each other, thus validating the measurements. The results therefore indicate that the DNA–coralyne complex junction functions as a molecular rectifier. We emphasize that the observed strong rectification behavior is highly counterintuitive in light of the apparent symmetrical molecular

structure of the DNA–coralyne complex. Indeed, such strong rectification is an unprecedented feature exclusive to DNA-based molecular devices. A complementary study performed on poly d(CG)4 DNA, which eliminates the three mismatched base pairs, shows the absence of rectification, suggesting the specificity of the designed mismatch sequence for the observed I–V rectification.

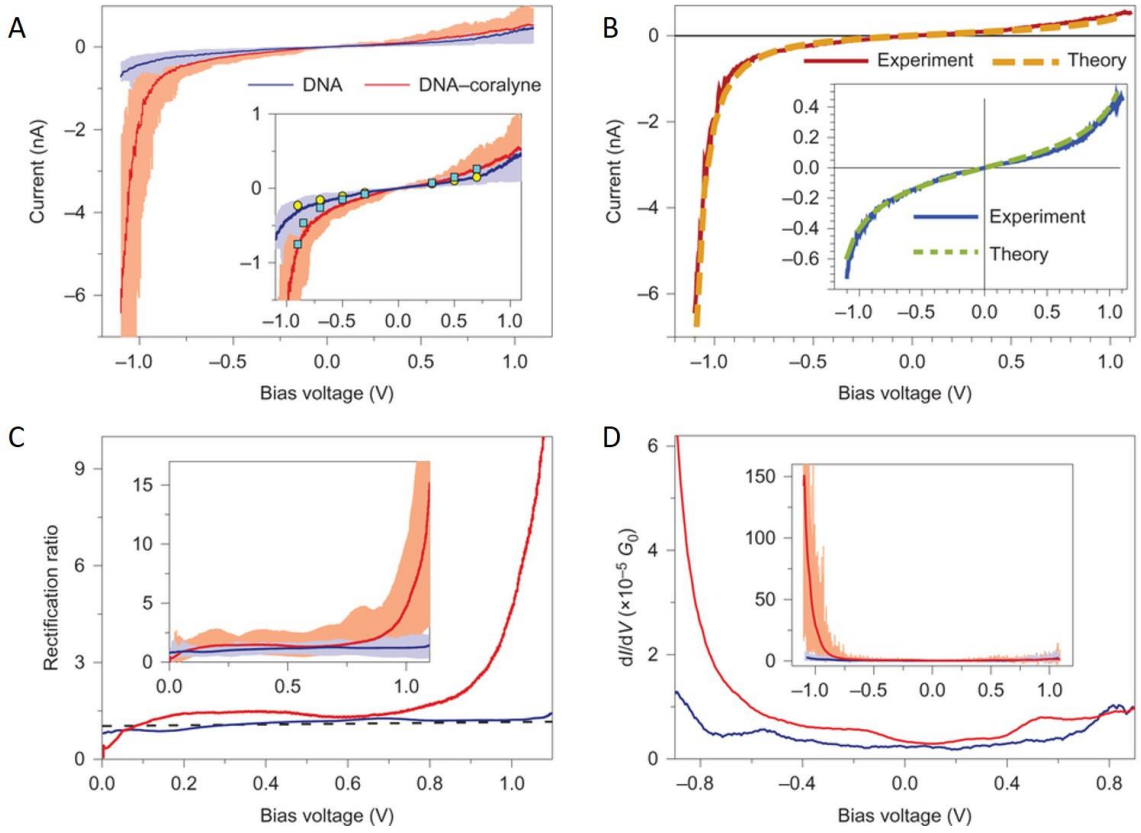

Figure 6.3 (A) Average I–V curves (solid line) over 40 individual curves (light shadow) of native DNA (blue) and DNA–coralyne complex (red). Inset: Graph overlay of I–V curves with static current values (yellow circles, native DNA; cyan squares, DNA–coralyne complex) under different bias voltages. (B) Experimental (solid red line) and theoretical (dashed orange line) I–V curves for DNA–coralyne complex (main panel) and native DNA (inset). (C) Average rectification ratios of native DNA (blue) and DNA–coralyne complex (red). Inset: Average rectification ratios of native DNA and DNA–coralyne complex over 40 individual rectifications

versus bias voltage curves. (D) Average differential conductance (dI/dV) of native DNA (blue) and DNA–coralyne complex (red). Inset: Average dI/dV of native DNA and DNA–coralyne complex over 40 individual dI/dV curves. Reprinted from ref. 38.

To describe rectification, two quantities are necessary: the rectification ratio (RR) and the switch-on voltage. **Figure 6.3C** presents RR versus bias curves following RR = $\left|I_{forward}/I_{reverse}\right|$ (here $-I(V_-)/I(V_+)$) for both the native DNA and the DNA–coralyne complex. In contrast to the native DNA, the average RR of which was close to unity within the entire bias sweeping regime, the DNA–coralyne complex exhibited small RR values slightly above unity under low bias (0~0.7 V) that increased sharply when the bias exceeded 0.7 V and then jumped to ~15 at 1.1 V. We define the bias voltage at which the RR value starts to deviate from unity toward higher values as the switch-on voltage, which for this DNA–coralyne molecular rectifier is thus determined to be ~0.7 V. Given the symmetrical nature of the molecular structure of the DNA–coralyne complex, its RR of 15 – much greater than the RR values (2~10) typically reported for molecular junctions with asymmetric molecules or inconsistent molecule–electrode contacts—is encouraging[100, 119]. This value is also close to the theoretically estimated upper limit of RR (~20) that can be achieved in a coherent transport molecular junction system[201]. A much higher RR can thus be expected when additional asymmetric factors, such as the asymmetric environmental control of the junction system[39] or asymmetric gating[202, 203], are introduced into the demonstrated DNA–coralyne junction system. Based on our promising results, we believe that this DNA–coralyne junction system is an ideal testbed for pushing the limits of experimental molecular rectification closer to achieving the goal of functional molecular devices.

Rectification mechanism of DNA-coralyne complex junctions

To explore the mechanism of DNA-coralyne complex junction rectification, we turned to theoretical calculations, central to which is the assumption that the electron transport along the DNA molecular junction is fully coherent, which is reasonable in light of the short lengths of the DNA molecules used in our experiments.[204, 205] Therefore, we used a fully coherent, tight-binding model for the DNA junction[206-209], graphically depicted in **Figure 6.4A**. The electronic states localized on the base units are defined as $|n, s\rangle$, where n denotes the position of the base along the DNA chain and s denotes the strand (top or bottom). The double-strand DNA molecule is encoded into a tight-binding double ladder, described by the Hamiltonian,

$$\mathcal{H} = \sum_{n=1}^{11} \sum_{s=1,2} \epsilon_{n,s} \, |n, s\rangle\langle n, s| + \sum_{n,s} \left(\alpha_{n,n+1}^{s} |n, s\rangle\langle n+1, s| + \text{h. c.}\right) + \sum_{n} (\beta_n |n, 1\rangle\langle n, 2| + \text{h. c.}) \, , \quad (6.1)$$

where $\epsilon_{n,s}$ are the onsite energies of the (excess) charges localized on the $|n, s\rangle$ basis, $\alpha_{n,n+1}^{s}$ are the intra-strand coupling matrix elements between neighboring bases, and β_n are the inter-strand coupling matrix elements. These parameters for the native DNA, which depend on the bases and their sequence (i.e., order of the bases), were evaluated in earlier theoretical studies.[210-212] However, considering the possible electrostatic interaction between the electrodes and the DNA chain, which is known to alter the energetics of molecules in proximity to metallic surfaces, the onsite energies of the bases that are in contact with the electrodes[42], $\epsilon_{1,1}$ and $\epsilon_{11,2}$, are treated as free fitting parameters.

To address the rectification behavior, an additional term that phenomenologically describes the voltage drop across the junction[213] was added to the Hamiltonian

$$\mathcal{H}_V = \sum_{n=1}^{11} \sum_s V_n |n,s\rangle\langle n,s|, \quad (6.2)$$

where V_n is the shift in the local energy. Assuming that the voltage profile along the chain is linear and that a fraction φ of the total voltage drop V falls on the DNA chain, the local potential shift can be estimated via[213]

$$V_n = \varphi\left(\frac{n-1}{10} - \frac{1}{2}\right)V, \quad (6.3)$$

such that $V_1 = -\frac{\varphi V}{2}, V_{11} = \frac{\varphi V}{2}$, leading to a total voltage drop of φV across the DNA chain and to a voltage-dependent Hamiltonian. The value of φ is treated as a fitting parameter. For the electrodes, we calculated the current using the Landauer formalism in the frame of the wide-band approximation.[214]

Electron transport properties of native duplex DNA The first step in characterizing DNA junctions is to calculate the transport properties of the native duplex DNA. Considering that the local onsite energies and coupling matrix elements are provided from previous calculations, there are four fitting parameters: the onsite energy shift S_1 at the edge sites in contact with the electrodes, the level broadening Γ, the voltage drop fraction φ and the electrode chemical potential μ. We calculated the I-V curves and fit the theoretical curve with the experimental data by minimizing (using a Dynamic Metropolis Monte-Carlo minimization algorithm[215]) the squared difference of $I_{theory}(V) - I_{data}(V)$.

Figure 6.3B (inset) shows the excellent agreement between the experimental (solid blue) and theoretical (dashed green) I-V curves. We note that the chemical potential of gold that we found with our fitting procedure is close to its known value of ~

-5.1~5.3 eV. However, we found surprising values for two of the fitting parameters: first, level broadening was about 1eV, much larger than the values found in most molecular junctions, i.e., 10^{-3}~10^{-1} eV; second, the voltage drop along the junction was extremely small. Because such strong molecule-electrode binding usually results in a substantial voltage drop on the molecule, these two unexpected fitting parameter values seem to contradict each other.

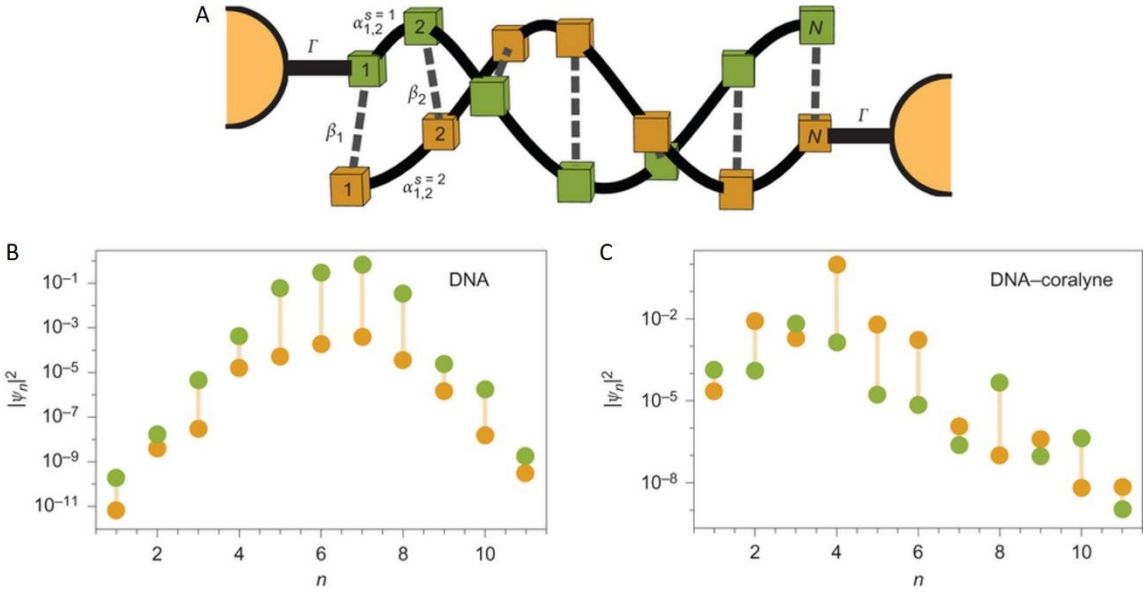

Figure 6.4 (A) Schematic representation of the tight-binding model for the double-stranded DNA molecular junction.(B, C) Weight of the wavefunction (orange, top strand; green, bottom strand) closest to the chemical potential as a function of base pair position along the chains of the native DNA chain (B) and the DNA–coralyne complex (C). Note that, for the DNA–coralyne complex, the asymmetric electronic structure induced by the intercalation of coralyne shifts the orbital weights asymmetrically, resulting in a highly asymmetric effective coupling of the orbitals to the electrodes. Reprinted from ref. 38.

To unravel this apparent contradiction, we plotted the squared amplitude $|\psi_n|^2$ of the wave function of the DNA double strands (orange – top strand; blue – bottom strand) as a function of its position along the DNA chain (**Figure 6.4B**). Examining the wave functions closest in energy to the electrodes' chemical potential (i.e., the state that contributes the most to the charge transport) shows that the wave functions are highly localized around the central area of the DNA chain. Moreover, from the center of the chain to its edges, the wave function weight drops by approximately eight orders of magnitude. Therefore, despite its large level broadening value, the DNA junction effectively behaves as a molecular level localized at the center of the chain and very weakly coupled to the electrodes, which explains the observed small voltage drop. In addition, the wave function exhibited only slight asymmetry, which conferred on the native DNA its relatively poor rectification behavior.

DNA-coralyne complex electron transport properties To account for the electron transport properties of the DNA-coralyne complex, we postulated that intercalation of the two coralyne molecules between the three A-A base pairs located at the center of the DNA strands would only alter the local energies of the surrounding bases. Under this scenario, we can safely assume that parameters related to DNA-electrode coupling – Γ, μ, S_1 and φ – are not affected and should be the same for the DNA-coralyne complex and for the native duplex DNA. In addition, their values should match those found above when fitting the I-V curves of the native DNA. On the other hand, the on-site energies of the central sites, i.e., close to the intercalation points of the coralyne molecules, are altered, and the numerical values obtained from the literature cannot be used. Therefore,

we define the local energy shifts ($S_{5,1}, S_{6,1}, S_{7,1}, S_{5,2}, S_{6,2}, S_{7,2}$) due to the presence of the coralyne.[209-211]

The coralyne-induced local energy shifts are new fitting parameters that should be found by minimizing the difference between the theoretical and experimental I-V curves. We note, however, that we are unable to fit the experimental curve with high accuracy (<1%) without breaking all the spatial symmetries in these sites. For example, one could imagine that the symmetry $S_{n,1} = S_{n,2}, n = 5,6,7$ exists, but we found that this is not the case, a logical outcome dictated by the asymmetry of the coralyne molecule. The fitting results show that the theoretical I-V curve (blue line) and the corresponding experimental I-V curve (green line) agree well with each other (**Figure 6.3B**).

To understand the origin of the rectification, we again plotted the squared wave function $|\psi_n|^2$ for the DNA level closest to the electrode Fermi level (**Figure 6.4C**). In contrast to the wave function of native DNA, that of the DNA-coralyne complex exhibits striking asymmetry, such that a difference of four orders of magnitude was found between the wave function weights at the left and right edges. The spatial asymmetry induced by coralyne intercalation thus explains the strong rectification by the DNA-coralyne complex.

We also measured the current through the single-molecule junction by cyclically sweeping the bias between −1.2 V and 1.2 V, which showed a large hysteresis under negative bias for the DNA-coralyne complex, a finding that is in contrast to the well overlapped forward and backward currents of native DNA and that suggests a bias-dependent structural change[213, 216]. When the voltage drops along the chain, the response to the voltage drop, which depends on the direction of the bias drop due to the above-

mentioned asymmetry, is different, thus leading to a dependence of the transmission function – and consequently, the current – on bias direction. This observation is in good agreement with the experimental dI/dV result, which shows a pronounced asymmetry in the local density of states that contributed to the current under opposite bias directions (Fig. 3d). It is surprising that such strong rectification behavior can be achieved with such a small value of the voltage drop fraction $\varphi \sim 2 \times 10^{-4}$, a finding that demonstrates the strong sensitivity of the transport properties to local conditions.

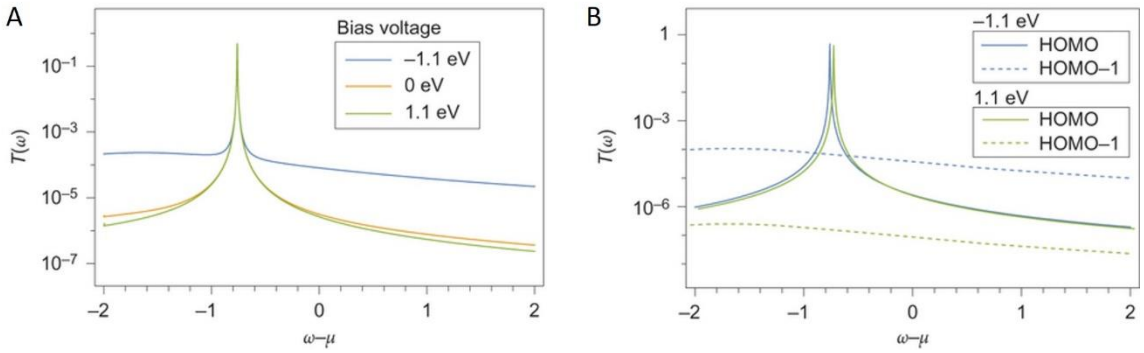

Figure 6.5 (A) Transmission function T(ω) as a function of ω for different values of bias voltage V = –1.1, 0 and 1.1 eV. The position and height of the transmission resonance are unaffected by the bias, indicating that the origin of rectification is a change in the off-resonance background transmission. (B) HOMO (solid lines) and HOMO−1 (dashed lines) contributions to the transmission function T(ω) as a function of ω for different values of bias voltage V = –1.1 and 1.1 eV. The HOMO contribution, corresponding to the transmission resonance, is unaffected by the voltage drop, while that of HOMO−1 increases by three orders of magnitude. This demonstrates that, although for low bias the conductance and current are typically determined by the resonant transmission channel, the rectification behavior of the DNA–coralyne complex at large biases is determined by the off-resonance transmission channel. Reprinted from ref. 38.

We explored the role of the voltage drop further by plotting the transmission function $T(\omega, V)$ of the DNA-coralyne complex for three voltage values $V = -1.1, 0, 1.1V$ (**Figure 6.5A**). The first conclusion that can be drawn from **Figure 6.5A** is that electron transport through the DNA is indeed dominated by a single orbital (HOMO level, i.e., the level at which the energy is closest to the chemical potential). Second, it can also be concluded that the voltage drop along the junction (which is small due to the small value of φ) does not affect the position of the resonance. Considering that the coralyne molecules intercalated between three mismatched A-A base pairs, this result coincides with those of previous reports showing that the HOMO of DNA molecules is dominated mainly by the HOMO of guanine bases, which are not expected to be perturbed in our case.[117, 144] However, the substantial change induced by coralyne intercalation is conferred by the off-resonance background transmission.

A more detailed examination of the wave function reveals that the large background transmission enhancement is related to a four-order increase in the magnitude of the coupling between the electrodes and a level lying about 1.65 eV away from the chemical potential, i.e., the HOMO 1 level. This outcome is seen in Fig. 5b, where the HOMO and HOMO-1 contributions to the transmission function (solid and dashed lines, respectively) are plotted for bias voltages $V = -1.1, 1.1$ eV (orange and green lines). We can thus conclude that while the overall conductance is dominated by the level closest to the electrodes' chemical potentials, the rectification behavior is in fact due to a voltage-drop-induced change in the coupling (and resulting transmission) of the HOMO-1 level.

The picture that emerges from these calculations is thus the following. Although the native DNA exhibits some asymmetry, it is not sufficient to generate substantial rectification, especially in light of the small voltage drop on the molecule. When coralyne is intercalated between the DNA strands, the asymmetric structure of the coralyne molecule induces additional asymmetry onto the DNA orbitals. This asymmetry is manifested mainly in a shift in the orbital structure of the wave-functions but not in the orbital energies. The most striking consequence of this change is an increase in the effective coupling between the HOMO-1 orbital and the electrodes (which is by itself asymmetric, being very small for positive bias and large for negative bias). Thus, the HOMO-1 conduction channel, which is off-resonant and governed by the level broadening for all voltages studied, is the one mostly affected by the coralyne intercalation.

To the best of our knowledge, our finding that coralyne intercalation only manipulates the HOMO-1 transmission function by increasing its coupling strength without perturbing the frontier orbital of HOMO is a feature unique to DNA-coralyne complex molecular junctions. We note that this rectification mechanism is essentially different from any models proposed in the past to account for the rectification behavior of molecular junction systems that possess asymmetric molecular cores dominated by a single orbital asymmetrically coupled to the electrodes.[130, 131, 133] We point out, however, the resemblance between the mechanism we suggest here to a similar mechanism in molecular junctions responsible for negative differential conductance, where a bias voltage drop along an asymmetric molecule changes the effective coupling between the molecular orbitals and the electrodes.[213]

6.5 Conclusion

In summary, we constructed a single molecular rectifier based on intercalating specific, small molecules into designed DNA strands. Characterization by diverse STMBJ techniques of the electronic transport properties of single molecular junctions consisting of native DNA or of a DNA-coralyne complex showed drastic differences. The I-V curves of the single DNA-coralyne complex junction device exhibited a strong rectification ratio of around 15 at 1.1 V. Using the NEGF method, calculations based on a coherent tight-binding model revealed that the rectification is predominantly caused by the coralyne-induced spatial asymmetry, which leads to voltage-drop-induced changes in the coupling and transmission functions of the molecular HOMO-1 level. Not only do these results offer a new method for studying DNA-molecule interaction, they also suggest a novel strategy for the engineering of single molecular electronic elements based on a specifically designed functional DNA complex.

CHAPTER 7

FERMI LEVEL PINNING OF CHARGE-TRANSFER RESONANCES IN MOLECULAR JUNCTIONS

- "*Fermi level pinning of charge-transfer resonances in molecular junctions containing the 2,2':5',2''-terthiophene:TCNE charge-transfer complex*" Kun Wang*, Andrea Vezzoli*, Iain M. Grace*, Maeve McLaughlin, Richard J. Nichols, Bingqian Xu, Colin J. Lambert and Simon J. Higgins. (* equal contribution). To be submitted to J. Phys. Chem. Lett..

7.1 Abstract

Interference feature in the transmission spectra can dominate charge transport in metal-molecule-metal junctions. We introduced interferences (such as Fano resonances) in the transmission profile of electron-rich molecular wires by forming their charge-transfer complexes with tetracyanoethylene (TCNE). Single-molecule conductance measurement using the STM-BJ technique allowed us to demonstrate experimentally that the conductance of the complex is almost independent of the conductance of the uncomplexed wire, a strong proof of the predicted pinning of the Fano resonance to the Fermi level of the metallic leads. Furthermore, our results show that, for better agreement between experimental data and theoretical predictions, the use of weak Au-coordinating contact groups is preferable when studying supramolecular effects and room-temperature quantum interference.

7.2 Introduction

Charge transport through organic molecules was first described from a theoretical point of view in the 1970s, with the seminal Aviram-Ratner molecular diode,[5] and this is generally considered the birth of the field of molecular electronics. However, it wasn't until the end of the 20th century that reliable methods to actually drive current through organic molecules were described, such as the mechanically controlled break junction setup[18] and scanning probe microscope techniques, using an STM[31-33] or an AFM.[217] Recently, supramolecular interactions such as solvent effects[218-221], charge-transfer (CT) or host-guest complexation[54, 222-225], π-stacking interactions[226-229] and hydrogen-bonding[230, 231] have attracted increasing attention as a way to increase chemical

complexity of metal-molecule-metal junctions. Furthermore, supramolecular interactions that have a strong effect on junction conductance can be exploited in electronic devices such as sensors[219, 224] and chemFETs.[232] Among the supramolecular interactions, CT complexation is particularly interesting from the point of view of electronic devices. Several ground-breaking discoveries, such as the first organic material with metallic behavior (TTF:TCNQ)[233] and the first organic superconductor (Beechgard salts, [TMTSF]2PF6)[234] used CT complexes as bulk conductors.

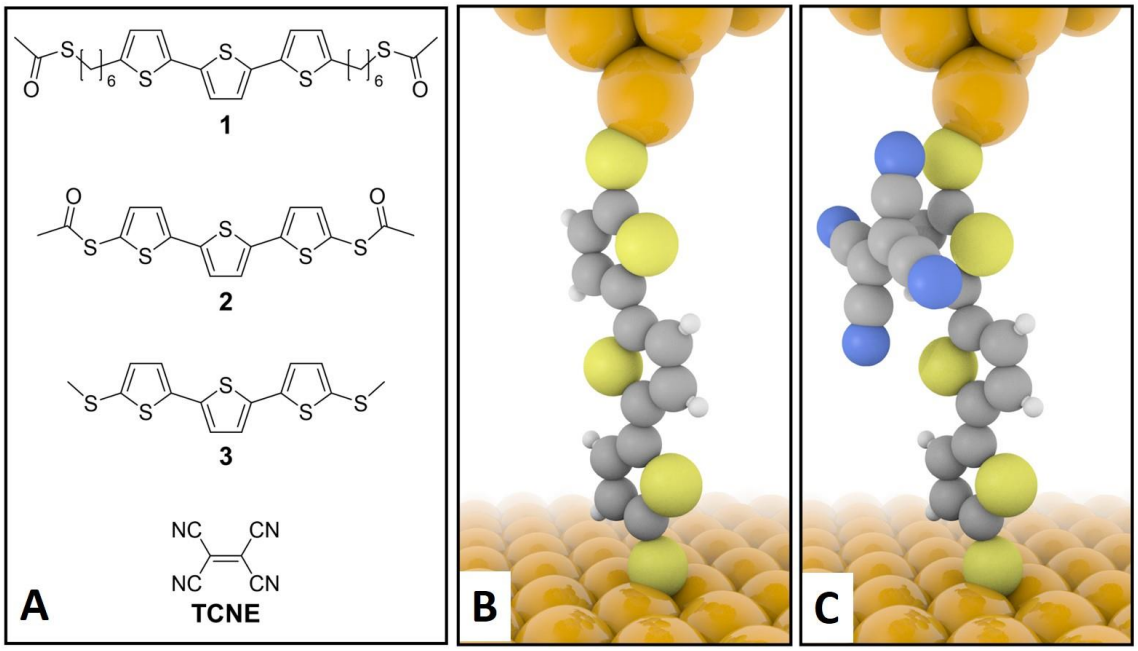

Figure 7.1 Structures of molecular wires mentioned in this study (A) and illustration of a molecular junction with compound 2 (B), and its CT TCNE complex (C), sandwiched between two Au electrodes.

While the solid-state structure determines the bulk properties, CT complexation in nanoscale molecular junctions results in additional resonances in the transmission profile, and we recently reported that these additional resonance promote charge transport with a

large conductance enhancement.11 In particular, a molecular wire with a 2,2':5',2"-terthiophene core showed >30-fold conductance increase upon complexation with the electron acceptor tetracyanoethylene (TCNE). As the additional CT resonance arises from a part-filled TCNE orbital, we proposed that its position in the energy profile of the junction must be always near to the Fermi energy EF, and therefore the charge transport through the complex is less dependent on the position of the molecular resonances. To probe this phenomenon, we synthesized two 2,2':5',2"-terthiophene containing molecular wires (molecules 2 and 3 in **Figure 7.1**) with different terminal units that bind to the electrodes, and measured their conductance as TCNE CT complexes.

We found that, while the three molecular wires have different conductance values in their "free" state, spanning more than one order of magnitude, they all give very similar values of $\sim 10^{-3}\, G_0$ (where G_0 is the quantum of conductance, 77.48 μS), when complexed with TCNE. This is a strong experimental proof of the Fermi level pinning of the additional conductance channel introduced by the part-filled TCNE orbital, and that charge transport is dominated by this additional resonance, characteristic of CT complexation.

7.3 Experimental Details

Conductance measurements The conductance of molecular junctions were determined using the STM break junction (STM-BJ) method.[31] The gold substrates were prepared by evaporating ~100 nm of gold onto freshly cleaved mica sheets using a thermo-evaporator under a vacuum of 10^{-7} Torr. The gold beads for Au substrate deposition was purchased from Kurt J. Lesker Company (99.999%), and mica sheets were purchased from Ted

Pella, Inc. The Au surfaces were annealed in hydrogen flame for several minutes before immersion in sample solutions of molecule. This annealing step allowed epitaxial reconstruction of gold atoms to form large terraces of Au(111). Then sample solution containing target molecules was dropped onto the freshly flamed Au surface to form the self-assembled monolayer of molecules for following conductance measurements, which were conducted in the absence of a liquid medium. Typically, conductance data were collected by driving a freshly cut Au tip into Au substrate and then withdrawing it. As the tip was pushed into the surface and then retracted, a fresh Au–Au junction was formed, thinned down to a single atom (point contact), and finally broken upon further retraction. After the rupture of the junction, a molecule can bridge the tip-substrate gap. The current (I) was recorded at a fixed tip-substrate bias (V) and conductance G is determined by Ohm's Law (G=I/V). The STM tip engaged towards the Au substrate at a stop position controlled by a threshold tip-substrate current of 25 μA under a bias voltage of 0.3 V, plus an additional engage distance of 0.5 nm to ensure the physical contact between the tip and substrate. This setting guaranteed that all conductance traces displayed clear Au-Au point contact plateau prior to the molecular plateau. The tip engaging speed of 35 nm s^{-1} and retraction speed of 20 nm s^{-1} were used in the experiments. This process was repeated thousands of times to reveal thousands of curves that were subsequently used for the construction of conductance histograms. To prepare the samples, sample molecules were first dissolved in the mixed solution of CH_2Cl_2 and ethanol (1:1 (v:v)) to give a 10^{-3} M solution of sample molecules. Sample molecule solution was placed onto the freshly flamed Au surface and left for an incubation of 15 minutes which led to the formation of a self-assembled monolayer. Then the sample surface was rinsed with ethanol and dried

with high purity nitrogen gas. Conductance measurements were subsequently conducted in air at room temperature (~20 ˚C). To form TCNE doped molecules, TCNE solution (10^{-2}M in CH_2Cl_2) was dropped onto the prepared monolayer of sample molecules for a subsequent incubation period of 1 h. Then the sample was copiously rinsed with ethanol and dried with high purity nitrogen gas. Conductance measurements for doped molecular wires were also carried out in air at room temperature (~20 ˚C). In these experiments, the bias voltage was 0.3 V.

Synthesis All reactions were performed in degassed or dry solvents, in oven dried glassware, under Ar. All reagents were purchased from Sigma-Aldrich Chemical Company. Solvents were dried and stored under activated 3 Å molecular sieves (20% m/v).[235] Alkyllithium compounds were titrated against benzylbenzamide to a blue endpoint before use. 2,2':5',2"-terthiophene was synthesized following published procedures[236] by Kumada coupling of 2-thienylmagnesium bromide and 2,5-dibromothiophene, using $NiCl_2$(dppe) as catalyst.

Preparation of mol 2: To a solution of 2,2':5',2"-terthiophene (0.5 g, 2.01 mmol) in dry THF (40 mL) n-butyllithium (**caution!** 1.6 M, 4.00 mmol) was added dropwise at -78 ºC. The yellow suspension was stirred for 30 minutes at that temperature and dimethyl disulfide (0.36 mL, 4.05 mmol) was added dropwise. The mixture was allowed to return to room temperature and stirred for 4 hours. Water (100 mL) and CH_2Cl_2 (30 mL) were then added, the phases were separated and the aqueous phase extracted three times with CH_2Cl_2. The combined organic phases were then washed with brine, dried over $MgSO_4$ and concentrated under vacuum. The resulting yellow crude product was then purified by column chromatography (20 % CH_2Cl_2 in hexanes) to afford a slightly impure (NMR)

yellow solid. Recrystallization from hot hexanes afforded the title compound as bright yellow solid (0.329 g, 48 %). Found: C = 49.34, H = 3.53, S = 48.71 %. $C_{14}H_{12}S_5$ requires C = 49.37, H = 3.55, S = 47.08 %. ^{1}H NMR (400 MHz, $CDCl_3$): 7.01 (s, 2H, Th), 6.99 (ABq, J = 3.9 Hz, J_{AB} = 7.0 Hz, 4H, Th), 2.51 (s, 6H, CH_3) ppm. ^{13}C NMR (100 MHz, $CDCl_3$): 139.0, 136.6, 135.9, 131.8, 124.3, 123.7, 22.1 ppm. *m/z* (HRMS, CI, CH_4) 340.9632 $[M + H]^+$, $C_{14}H_{13}S_5$ calc. 340.9621.

Preparation of mol 3: To a solution of 2,2':5',2"-terthiophene (0.5 g, 2.01 mmol) in dry THF (40 mL) *n*-butyllithium (**caution!** 1.55 M, 4.00 mmol) was added dropwise at -78 ºC. The yellow suspension was stirred for 30 minutes at that temperature and a suspension of S_8 (129 mg, 0.5 mmol) in THF (10 mL) was added dropwise. After further 60 minutes of stirring at -78 ºC, acetyl chloride (0.3 mL, 4.1 mmol) was added dropwise, and the mixture was allowed to return to room temperature and stirred overnight. Water (75 mL) and CH_2Cl_2 (15 mL) were then added, the phases were separated and the aqueous phase extracted three times with CH_2Cl_2. The combined organic phases were then washed with brine, dried over $MgSO_4$ and concentrated under vacuum. The resulting yellow crude product was then purified by column chromatography (10 % hexanes in CH_2Cl_2) to afford the title compound as bright yellow solid (0.577 g, 72 %). $C_{16}H_{12}O_2S_5$ requires C = 48.46, H = 3.05, S = 40.42 %. Found: C = 48.25, H = 3.06, S = 40.25 %. ^{1}H NMR (400 MHz, $CDCl_3$): 7.11 (s, 2H, Th), 7.12 (AXq, J = 3.9 Hz, J_{AX} = 33.7 Hz, 4H, Th), 2.43 (s, 6H, CH_3) ppm. ^{13}C NMR (100 MHz, $CDCl_3$): 194.1, 142.9, 136.5, 136.1, 125.2, 124.3, 124.1, 29.6. *m/z* (HRMS, ES+, CH_3OH + NaOAc) 418.9347 $[M + Na]^+$, $C_{16}H_{12}NaO_2S_5$ calc. 418.9339.

7.4 Results and Discussions

In our previous work, TCNE complexation with molecule 1 has shown a > 30-fold conductance boost compared to the conductance of molecule 1 alone. In the present work, we focus on the influence of linker effect (the chemical moiety responsible for the formation of the contact with the electrodes) on the conductance boost caused by TCNE complexation. We reasoned that the removal of the insulating hexyl chains present in compound 1 would results in an increased conductance of the bare molecular wire, and this may lead to a different increase in conductance upon complexation. We therefore synthesized molecular wires containing the 2,2':5',2"-terthiophene (see experimental details for synthetic procedures) with two different contacts directly bound in 2,5"-position: a protected thiol (as thioacetate), that readily cleaves in the presence of gold to give a thiolate covalent bond,[237, 238] and a methyl sulfide, that preferentially binds to under-coordinated gold sites[105, 239] through lone-pair interactions. The STM-BJ technique[31] was then used to measure the electrical properties of Au-molecule-Au junction with sample molecules in the presence and absence of TCNE. Briefly, a Au STM tip was brought close to the surface of a Au(111) substrate, in the presence of either sample molecule or of the sample molecule:TCNE complex. It was then retracted while the tunneling current was monitored. A fresh Au-Au junction is formed, and on retraction this thins down to a single atom (point contact), which is finally broken upon further retraction. This process results in peaks in a conductance histogram at integer multiples of G_0 owing to atomic rearrangements in the junction. When the point contact breaks, if a molecule (or molecules) binds to both gold contacts, then subsequent additional plateau are seen in the current–distance plot at conductance values much smaller than G_0,

corresponding to tunneling transport through the molecule. Eventually, as retraction continues, the molecular junction breaks and the current rapidly falls to a very low value consistent with direct electrode tunneling. Example conductance traces with Au-Au point contact plateau and molecular junction plateau are shown in right panels of **Figure 7.2** for sample molecules (green traces) and molecule:TCNE complexes (orange traces). Typically, thousands of such traces were employed for each set of experimental conditions, and the traces were binned to produce one-dimensional log-scale conductance histograms and two-dimensional density plots. 2:TCNE complex yielded a conductance of $\sim 1.2 \times 10^{-3} G_0$, with an 8-fold increase when compared to the isolated molecule. 3:TCNE gave a conductance of $\sim 2 \times 10^{-3} G_0$, the highest conductance among all molecule:TCNE complexes and around 20 times larger than the conductance of molecule 3 alone.

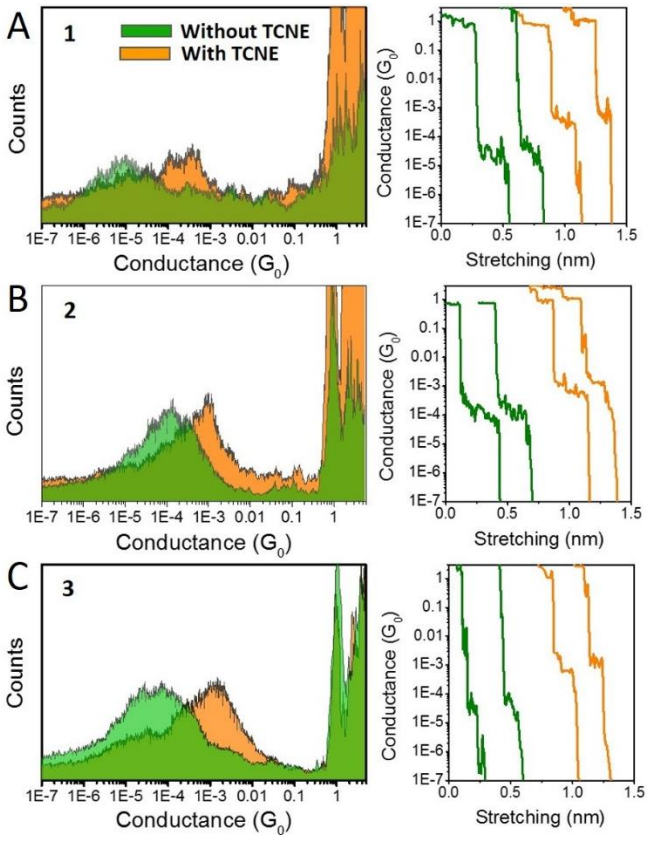

Figure 7.2: Conductance histograms (left) and example break-junction traces (right) of mol 1 (A), 2 (B) and 3 (C). Green: isolated molecule; Orange: TCNE complex.

It is worth noting that while the three molecular wires (1[54], 2 and 3) had different conductance values when in their uncomplexed state (spanning the range 10^{-5} to $10^{-3.7}$ G_0), they all give very similar conductance values ($\sim 10^{-3}$ G_0) when complexed with TCNE. In fact, the least conductive molecular wire 1 showed the largest conductance boost upon complexation (30-fold), while the most conductive compound 2 had the smallest increase (8-fold). This is a strong indication that the charge transport through molecule:TCNE complex is dominated by the additional conductance channel introduced by the presence of TCNE, and that its position in energy, as arising from a semi-occupied orbital, is pinned to the E_F of the electrodes. However, the linker plays a crucial role in deciding the coupling strength between the TCNE and sample molecule. Extra Fano-resonance peak has been previously observed for molecule 1:TCNE complex which very well interpreted the conductance boost phenomena.

To probe the underlying mechanism to see if it is the same for different linkers, we performed theoretical studies using DFT. The previous theoretical work on molecule 1 assumed an optimized geometry of the molecular junction with possible fluctuations in the complex geometry being treated through sampling a wide range of possible binding geometries for the TCNE molecule. Due to the localized nature of the orbital producing the Fano resonance, the effect of these fluctuations showed that the anti-resonance feature was ‘smeared’ out. We now expand on this approach by focusing on modelling the geometrical fluctuations using molecular dynamics which goes beyond the idealized model previously used.

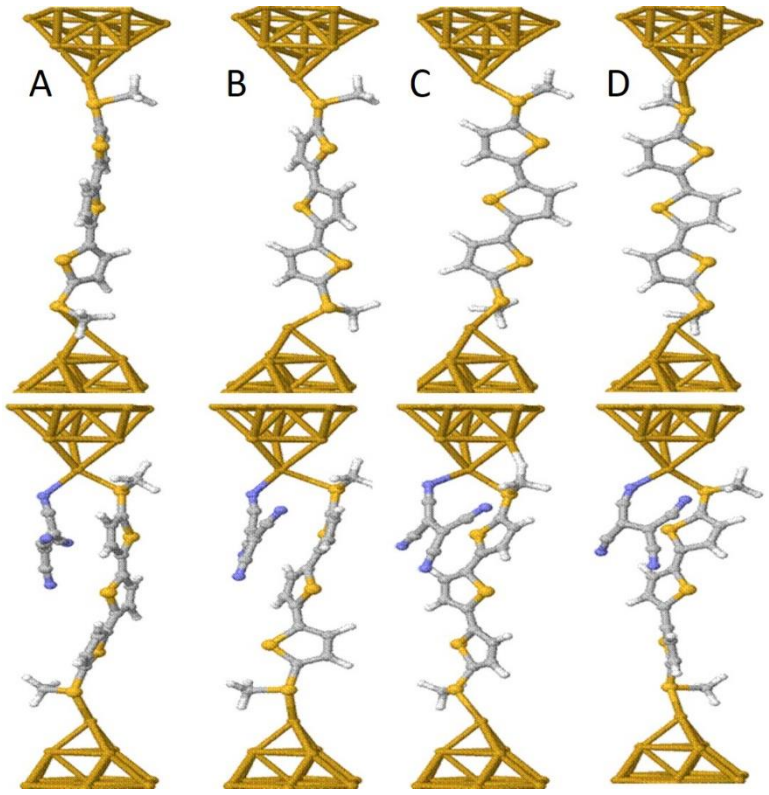

Figure 7.3 'Snapshots' of the molecular junction for molecule 2 (top) and molecule 2:TCNE (bottom) after (a) 0.5ps, (b) 1ps, (c) 1.5 ps and (d) 2.0 ps.

The evolution of the junction (**Figure 7.3** for molecule 2) over a small time increment (0.5 ~ 2ps) shows that at room temperature the structure of the molecule, the binding configuration and the complex geometry changes significantly. To see the role this plays in the conductance of the junction the zero bias transmission coefficient T(E) is calculated for each of these 'snapshots'. For molecule 2 (**Figure 7.4B**) the effect of using the different linker group (-SMe) shifts the Fermi Energy (0 eV) into the middle of the HOMO-LUMO gap in comparison to molecules 1 (**Figure 7.4A**) and 3 (**Figure 7.4C**) where the thiol linkers produce HOMO dominated transport. For all of these junctions, the effect of temperature fluctuations causes the value of T(E) to vary by at least an order of magnitude and more in the case of molecule 1. For the complexed molecules (**Figure**

7.4D-F) the appearance of the extra resonance with a Fano line shape can be seen close to the Fermi energy, showing that the previously expected behavior is independent of the linker group. In the case of the thiol linker groups the resonances shift with fluctuations, while the -SMe linker seems to strongly pin this resonance at the Fermi Energy.

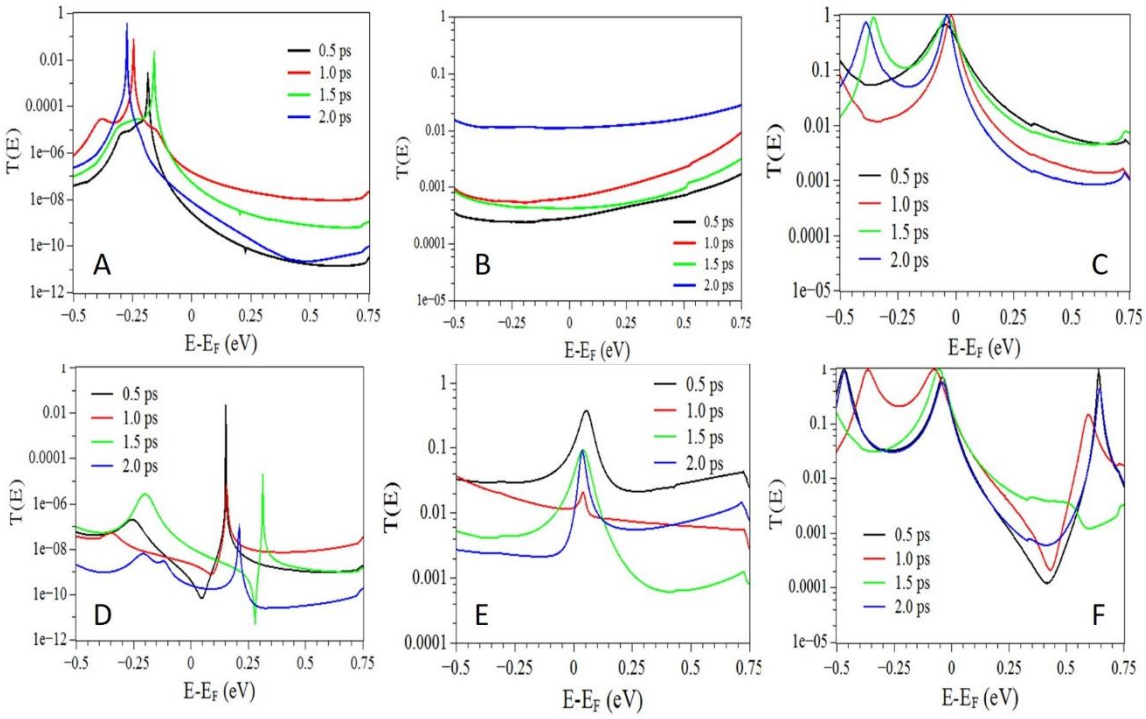

Figure 7.4 Zero bias transmission coefficient T(E) against electron energy at four different junction times for molecule 1 (A), 1:TCNE (D), molecule 2 (B), 2:TCNE (E) and molecule 3 (C), 3:TCNE (F).

To compare to the experimental measurements, we take an average of the thermally broadened transmission curves over the timespan of the molecular dynamic simulation (2ps) using the equation:

$$G(E_F) = \frac{2e^2}{h} \int T(E) \left(-\frac{df}{dE} \right) dE$$

where $G(E_F)$ is the average of 450 transmission curves and f is the Fermi distribution. For molecule 2 (**Figure 7.5B**) the conductance at 0 eV is ~3×10^{-3} G_0 and the conductance increases for 2:TCNE to ~6.5×10^{-2} G_0 which is a 21-fold boost. Comparing to the measured values, the theoretical conductance is higher by approximately an order of magnitude which may be due to the known limitations in DFT based quantum transport calculations.**[]** In the cases of molecule 1 and 3 the position of the Fano resonance is shifted away from 0 eV, and is at approximately 0.2 eV for molecule 1 and 0.35 eV for molecule 3. The ratio increase in the conductance at these energies is large for molecule 1 in the HOMO-LUMO gap**,** approximately 1000 at 0.2 eV (but smaller ~10 at 0 eV). While molecule 3 shows a smaller ratio ~8 at 0.5 eV. Therefore, depending on the position of the chosen Fermi energy the results give good agreement with experimental measurements in that the largest ratio increase is found in molecule 1.

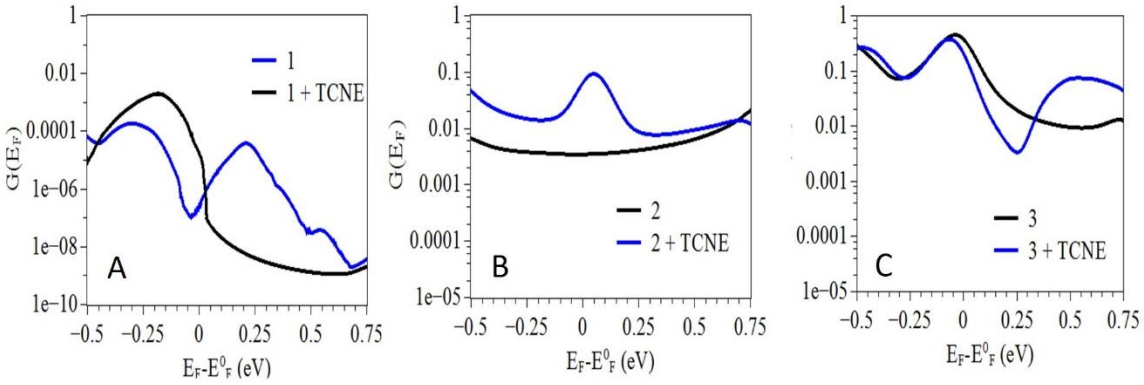

Figure 7.5 Thermally averaged conductance against Fermi energy for molecule 1 (A), 2 (B) and 3 (C).

However, the general trends of the measurements are applicable over a wide range of energies in the HOMO-LUMO gap which suggest that the mechanism of a Fano resonance arising upon CT complexation close to the Fermi energy is not dependent on

the linker group. The discrepancies between theory and measurement in molecules 1 and 3 can be attributed to the thiol linker group which changes the molecule on binding to gold and leads to a pinning of the HOMO resonance to the Fermi energy, while with the -SMe anchor the molecule remains unchanged and the Fermi energy lies in the gap. While confirming the proposed mechanism of conductance increase upon CT complexation, this also suggests that for better agreement between theory and experiment molecules with -SMe anchor groups are preferable. With such molecules, charge transport is likely happening in the HOMO-LUMO gap and no pinning of molecular resonances arises in the DFT calculations.

7.5 Conclusion

In summary, we measured charge transport through single-molecules and their charge-transfer complexes with TCNE, and showed that, while the molecules alone have conductance values spanning more than one order of magnitude, their complexes all give very similar conductance values ($\sim 10^{-3}$ G_0). Our results are a strong proof of the Fermi level pinning of the CT resonance we postulated in our previous work,[54] and strengthen the possibility of using such systems as detectors for electron-deficient analytes. During the theoretical analysis of these systems, we also found that, in DFT, pinning to the Fermi level of the HOMO resonance of molecules bearing thiol contacts competes with the pinning of the CT Fano resonance. This creates discrepancies between theory and experiments, and therefore the use of weaker binding groups (such as methyl thioether -SMe) is preferable in the study of supramolecular effects in molecular junctions to overcome the known DFT limitations.

CHAPTER 8

SUMMARY AND OUTLOOK

8.1 Summary

The major focus of this dissertation has been to explore and understand charge transport properties of single molecule junctions by combining delicate SPM-BJ experimental control with advanced data analysis methods. Molecules studied in this dissertation span from simple alkane molecules (octane-based molecules), small π-conjugated molecules (benzene-based molecules and terthiophene-based molecules) to complex large biomolecules (DNA molecules). The presented research projects have aimed at addressing several challenging issues in metal-molecule-metal junction system, including the effect of molecule-electrode contact interfaces, structure-property relation, current rectification, and quantum interference effect.

First, the widely studied yet to be fully understood contact effect in Au-alkanedithiol-Au junction was investigated via modulating a stabilized single molecule junction using modified CAFM-BJ technique. Strong force-conductance correlation was for the first time observed with the help of force-conductance cross-correlation analysis, suggesting a kinship between the mechanical behavior and the charge transport properties caused by variations at the molecule-electrode interfaces. Then, a more detailed investigation of the conductance change along with the junction elongation in Au-octanedithiol-Au junction revealed a unique shape of contact tunneling barrier, a linear

increase followed by a plateau in barrier height, which was interpreted by a newly developed tunneling barrier model.

Second, by alternating the two anchoring groups between thiol and amine in 1,4-disubstituted benzene molecular junctions, single-molecule conductance and I-V characteristic measurements revealed a strong correlation between current rectification effects and the asymmetry in contacts, i.e., rectification occurred whenever asymmetric contacts were introduced. Fitting of the rectification ratio by a newly modified Simmons model suggests asymmetry in potential drop across the asymmetric anchoring groups as the mechanism of rectifying I-V behavior.

Third, the effect of DNA's structural change on its conductance was explored by monitoring the conductance of a poly $d(GC)_4$ DNA while increasing the concentration of $MgCl_2$ in the buffer solution. It was found that the B- to Z- conformational change reduced the DNA conductance by two orders of magnitude. Using modified STM-BJ, we offered an alternative way to build up transition trend lines between two DNA conformations and monitored changes in DNA conformation at a spatial and temporal resolution never before achieved. This study also underscored the extreme sensitivity of DNA's conductance to its secondary structure change.

Fourth, we have constructed a molecular rectifier based on intercalating specific, small molecules into designed DNA strands. The I–V curves of the single DNA–coralyne complex junction device exhibited a strong rectification ratio of around 15 at 1.1 V. A non-equilibrium Green's function-based model—parameterized by density functional theory calculations—revealed that the coralyne-induced spatial asymmetry in the electron state distribution caused the observed rectification. This inherent asymmetry leads to

changes in the coupling of the molecular HOMO−1 level to the electrodes when an external voltage is applied, resulting in an asymmetric change in transmission.

At last, we introduced interferences (such as Fano resonances) in the transmission profile of electron-rich molecular wire by forming their charge-transfer complexes with tetracyanoethylene (TCNE). It was demonstrated experimentally that the conductance of the complex is almost independent of the conductance of the uncomplexed wire, a strong proof of the pinning of the Fano resonance to the Fermi level of the metallic electrodes. Furthermore, our results showed that, for better agreement between experimental data and theoretical predictions, the use of weak Au-coordinating contact groups is preferable when studying supramolecular effects and room-temperature quantum interference.

In summary, this dissertation has shown that both the important yet latent information in the experimental data can be isolated for specific study by incorporating detailed experimental modulations and controls, and functional charge transport properties can be finely tuned via modifying the structure of the junction. The experimental results and physical understanding presented in this dissertation have delivered a few significant hints for future investigation: 1) non-rectangle contact barrier should be carefully considered in junction systems involving Au-thiol contact; 2) asymmetric contact interfaces, either asymmetric anchoring groups or asymmetric electrode materials, can be used as a strategy to both create current rectification and enhance the existing rectification of the molecular core in molecular junctions; 3) DNA's secondary structure strongly depends on the ionic environment it stays in, and DNA's conductance is highly sensitive to its structural change; 4) DNA-small molecule complexation serves as a promising approach to effectively modify the electronic

structure of DNA molecule and create functional transport properties, and the introduced DNA-coralyne molecular rectifier can be used as a testbed for pushing the limit of rectification ratio of molecular rectifier; 5) quantum interference resonance (Fano resonance) formed by charge transfer complexation between electron-donor molecules and strong electron-acceptor molecules has strong Fermi level pinning effect, and this effect is not only significant for boosting the molecular conductance but also believed to greatly enhance the thermopower of molecular junction devices.

8.2 Outlook

One answer to the often-posed question of "when will we see molecular electronics in the real world" is "as soon as molecular devices can do something not currently possible with silicon.".[2] Based on the experimental and theoretical results obtained over the past two decades on molecular junctions, it is now sufficient to conclude that charge transport through 1~20 nm molecules has distinct properties from that in traditional semiconductor materials. Tremendous amount of researches as those discussed in this dissertation have highlighted the success of single molecule break-junction based techniques and their remarkable contributions in bringing us closer towards the overarching ambition to build, control, and use functional molecular devices.

In terms of charge transport in single-molecule junction system, there are still a few questions to answer: What is the effective contact chemistry to achieve solid mechanical connection between the molecule and the electrodes and to reduce the contact resistance? What is the ideal molecular candidate that can be used for future design and large-scale fabrication of molecular diode and field effect transistor (FET)? What is the

most effective way to electronically gate a molecular junction? How to significantly enhance the poor performance of single-molecule devices, e.g., low rectification ratio of molecular rectifier and small on/off ratio of molecular switches? What is the proper mean to scale up from single-molecule device to integrated circuits? To answer these questions or offer useful hints towards the solution of these questions, it is necessary that intense collaboration efforts between experimentalists, theorists, chemists and all other related researchers are extensively sparked.

Molecular junction system has become a playground of many fundamental studies which aim to improve our understanding of the physical nature of metal-molecule-metal junctions. As the field of molecular electronics continues to grow, physical properties beyond charge transport have also come into view recently. Recent studies are beginning to explore the rich physics of molecular junctions through measurements of piezoelectricity,[116, 240] optical effects,[241, 242] thermoelectricity,[51, 52] spintronics,[49, 243] and quantum interference[22, 55] concepts for which there are no analogues in conventional electronics.[62] Multiple properties that are of great interest and can be probed in single-molecule junction system are illustrated in **Figure 8.1**. A few experimental and theoretical attempts[49, 51, 53, 62, 186, 241] have suggested that molecular junction behavior can be finely controlled by manipulating the effects of light emission, heat flow, electron spin and quantum interference. Therefore, we have enough reason to believe that investigations of these varied properties of single-molecule junctions should be valuable for deeply understanding charge transport through molecular junctions, the device fabrication process, and the roadmap for future practical molecular electronics.

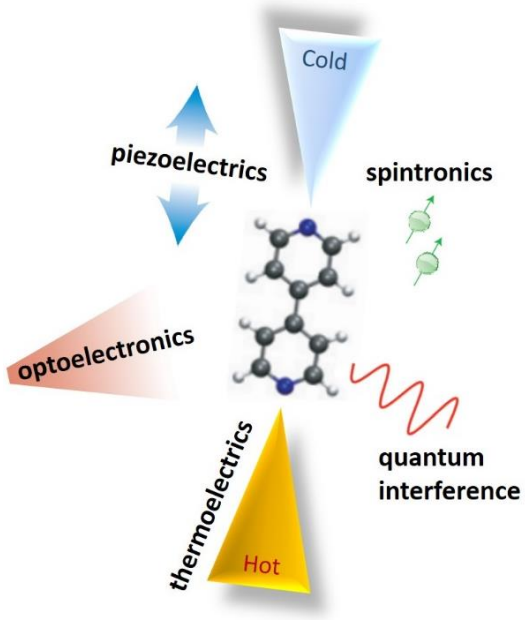

Figure 8.1 Probing multiple properties of single molecule junctions.

REFERENCES

1. G. E. Moore, *Electronics*, 1965, **38**, 114.
2. R. L. McCreery, H. Yan and A. J. Bergren, *Phys. Chem. Chem. Phys.*, 2013, **15**, 1065.
3. J. L. Zhang, J. Q. Zhong, J. D. Lin, W. P. Hu, K. Wu, G. Q. Xu, A. T. S. Wee and W. Chen, *Chem. Soc. Rev.*, 2015, **44**, 2998.
4. C. Jia and X. Guo, *Chem. Soc. Rev.*, 2013, **42**, 5642.
5. A. Aviram and M. A. Ratner, *Chem. Phys. Lett.*, 1974, **29**, 277.
6. K. Wang, J. M. Hamill, J. Zhou, C. Guo and B. Xu, *Faraday Discuss.*, 2014, **174**, 91.
7. E. Lortscher, *Nat. Nanotech.*, 2013, **8**, 381.
8. N. J. Tao, *Nat. Nanotech.* , 2006, **1**, 173.
9. S. Gregory, *Phys. Rev. Lett.*, 1990, **64**, 689.
10. C. M. Fischer, M. Burghard, S. Roth and K. Vonklitzing, *Appl. Phys. Lett.*, 1995, **66**, 3331.
11. K. Slowinski, R. V. Chamberlain, C. J. Miller and M. Majda, *J. Am. Chem. Soc.*, 1997, **119**, 11910.
12. C. Zhou, M. R. Deshpande, M. A. Reed, L. Jones and J. M. Tour, *Appl. Phys. Lett.*, 1997, **71**, 611.
13. J. Chen, M. A. Reed, A. M. Rawlett and J. M. Tour, *Science*, 1999, **286**, 1550.
14. R. L. McCreery and A. J. Bergren, *Adv. Mater.*, 2009, **21**, 4303.

15. Z. H. Zhong, D. L. Wang, Y. Cui, M. W. Bockrath and C. M. Lieber, *Science*, 2003, **302**, 1377.

16. J. Hamill, K. Wang and B. Xu, *Rep. Electrochem.* , 2014, **4**, 1.

17. M. Ratner, *Nat. Nanotech.*, 2013, **8**, 378.

18. M. A. Reed, C. Zhou, C. J. Muller, T. P. Burgin and J. M. Tour, *Science*, 1997, **278**, 252.

19. C. Joachim, J. K. Gimzewski and A. Aviram, *Nature*, 2000, **408**, 541.

20. R. Landauer, *Philos. Mag.*, 1970, **21**, 863.

21. M. Büttiker, Y. Imry, R. Landauer and S. Pinhas, *Phys. Rev. B*, 1985, **31**, 6207.

22. C. J. Lambert, *Chem. Soc. Rev.* , 2015, **44**, 875.

23. G. Sedghi, V. M. Garcia-Suarez, L. J. Esdaile, H. L. Anderson, C. J. Lambert, S. Martin, D. Bethell, S. J. Higgins, M. Elliott, N. Bennett, J. E. Macdonald and R. J. Nichols, *Nat. Nanotech.* , 2011, **6**, 517.

24. X. Zhao, C. Huang, M. Gulcur, A. S. Batsanov, M. Baghernejad, W. Hong, M. R. Bryce and T. Wandlowski, *Chem. Mater.*, 2013, **25**, 4340.

25. A. Salomon, D. Cahen, S. Lindsay, J. Tomfohr, V. B. Engelkes and C. D. Frisbie, *Adv. Mater.*, 2003, **15**, 1881.

26. S. M. Lindsay and M. A. Ratner, *Adv. Mater.*, 2007, **19**, 23.

27. D. D. Dunlap, R. Garcia, E. Schabtach and C. Bustamante, *Proc. Natl. Acad. Sci. USA*, 1993, **90**, 7652.

28. D. Porath, A. Bezryadin, S. de Vries and C. Dekker, *Nature*, 2000, **403**, 635.

29. H. W. Fink and C. Schonenberger, *Nature*, 1999, **398**, 407.

30. A. Y. Kasumov, M. Kociak, S. Gueron, B. Reulet, V. T. Volkov, D. V. Klinov and H. Bouchiat, *Science*, 2001, **291**, 280.

31. B. Q. Xu and N. J. Tao, *Science*, 2003, **301**, 1221.

32. W. Haiss, H. van Zalinge, S. J. Higgins, D. Bethell, H. Hobenreich, D. J. Schiffrin and R. J. Nichols, *J. Am. Chem. Soc.*, 2003, **125**, 15294.

33. W. Haiss, R. J. Nichols, H. van Zalinge, S. J. Higgins, D. Bethell and D. J. Schiffrin, *Phys. Chem. Chem. Phys.*, 2004, **6**, 4330.

34. R. J. Nichols, W. Haiss, S. J. Higgins, E. Leary, S. Martin and D. Bethell, *Phys. Chem. Chem. Phys.*, 2010, **12**, 2801.

35. C. J. Muller, J. M. Vanruitenbeek and L. J. Dejongh, *Physica C*, 1992, **191**, 485.

36. N. Agrait, A. L. Yeyati and J. M. van Ruitenbeek, *Phys. Rep.*, 2003, **377**, 81.

37. E. Lörtscher, J. W. Ciszek, J. Tour and H. Riel, *Small*, 2006, **2**, 973.

38. C. Guo, K. Wang, E. Zerah-Harush, J. Hamill, B. Wang, Y. Dubi and B. Xu, *Nat. Chem.*, 2016, **8**, 484.

39. B. Capozzi, J. Xia, O. Adak, E. J. Dell, Z.-F. Liu, J. C. Taylor, J. B. Neaton, L. M. Campos and L. Venkataraman, *Nat. Nanotech.*, 2015, **10**, 522.

40. I. Diez-Perez, J. Hihath, Y. Lee, L. Yu, L. Adamska, M. A. Kozhushner, I. I. Oleynik and N. Tao, *Nat. Chem.*, 2009, **1**, 635.

41. J. Zhou, S. Samanta, C. Guo, J. Locklin and B. Xu, *Nanoscale*, 2013, **5**, 5715.

42. M. L. Perrin, R. Frisenda, M. Koole, J. S. Seldenthuis, A. C. GilJose, H. Valkenier, J. C. Hummelen, N. Renaud, F. C. Grozema, J. M. Thijssen, D. Dulić and S. J. van der ZantHerre, *Nat. Nanotech.*, 2014, **9**, 830.

43. X. Xiao, L. A. Nagahara, A. M. Rawlett and N. Tao, *J. Am. Chem. Soc.*, 2005, **127**, 9235.

44. G. D. Scott, D. Natelson, S. Kirchner and E. Muñoz, *Phys. Rev. B*, 2013, **87**, 241104.

45. R. Frisenda, R. Gaudenzi, C. Franco, M. Mas-Torrent, C. Rovira, J. Veciana, I. Alcon, S. T. Bromley, E. Burzurí and H. S. J. van der Zant, *Nano Lett.*, 2015, **15**, 3109.

46. D. Rakhmilevitch, R. Korytár, A. Bagrets, F. Evers and O. Tal, *Phys. Rev. Lett.*, 2014, **113**, 236603.

47. Z. Li, H. Li, S. Chen, T. Froehlich, C. Yi, C. Schönenberger, M. Calame, S. Decurtins, S.-X. Liu and E. Borguet, *J. Am. Chem. Soc.*, 2014, **136**, 8867.

48. M. Baghernejad, X. Zhao, K. Baruël Ørnsø, M. Füeg, P. Moreno-García, A. V. Rudnev, V. Kaliginedi, S. Vesztergom, C. Huang, W. Hong, P. Broekmann, T. Wandlowski, K. S. Thygesen and M. R. Bryce, *J. Am. Chem. Soc.*, 2014, **136**, 17922.

49. J. Schwöbel, Y. Fu, J. Brede, A. Dilullo, G. Hoffmann, S. Klyatskaya, M. Ruben and R. Wiesendanger, *Nat. Commun.*, 2012, **3**, 953.

50. S. Schmaus, A. Bagrets, Y. Nahas, T. K. Yamada, A. Bork, M. Bowen, E. Beaurepaire, F. Evers and W. Wulfhekel, *Nat. Nanotech.*, 2011, **6**, 185.

51. Y. Kim, W. Jeong, K. Kim, W. Lee and P. Reddy, *Nat. Nanotech.*, 2014, **9**, 881.

52. P. Reddy, S.-Y. Jang, R. A. Segalman and A. Majumdar, *Science*, 2007, **315**, 1568.

53. H. Vazquez, R. Skouta, S. Schneebeli, M. Kamenetska, R. Breslow, L. Venkataraman and M. S. Hybertsen, *Nat. Nanotech.*, 2012, **7**, 663.

54. A. Vezzoli, I. Grace, C. Brooke, K. Wang, C. J. Lambert, B. Xu, R. J. Nichols and S. J. Higgins, *Nanoscale*, 2015, **7**, 18949.

55. R. J. Nichols and S. J. Higgins, *Nat. Nanotech.*, 2012, **7**, 281.

56. J. Zhou, F. Chen and B. Xu, *J. Am. Chem. Soc.*, 2009, **131**, 10439.

57. P. Makk, D. Tomaszewski, J. Martinek, Z. Balogh, S. Csonka, M. Wawrzyniak, M. Frei, L. Venkataraman and A. Halbritter, *ACS Nano*, 2012, **6**, 3411.

58. J. M. Hamill, K. Wang and B. Xu, *Nanoscale*, 2014, **6**, 5657.

59. K. Wang, J. M. Hamill, J. Zhou and B. Xu, *J. Am. Chem. Soc.*, 2014, **136**, 17406.

60. K. Wang and B. Xu, *Phys. Chem. Chem. Phys.*, 2016, **18**, 9569.

61. M. Kiguchi and S. Kaneko, *Phys. Chem. Chem. Phys.*, 2013, **15**, 2253.

62. S. V. Aradhya and L. Venkataraman, *Nat. Nanotech.* , 2013, **8**, 399.

63. L. Venkataraman, J. E. Klare, C. Nuckolls, M. S. Hybertsen and M. L. Steigerwald, *Nature*, 2006, **442**, 904.

64. S. Y. Quek, M. Kamenetska, M. L. Steigerwald, H. J. Choi, S. G. Louie, M. S. Hybertsen, J. B. Neaton and VenkataramanLatha, *Nat. Nanotech.* , 2009, **4**, 230.

65. D. Xiang, H. Jeong, T. Lee and D. Mayer, *Adv. Mater.* , 2013, **25**, 4845.

66. X. Li, J. He, J. Hihath, B. Xu, S. M. Lindsay and N. Tao, *J. Am. Chem. Soc.*, 2006, **128**, 2135.

67. C. Li, I. Pobelov, T. Wandlowski, A. Bagrets, A. Arnold and F. Evers, *J. Am. Chem. Soc.*, 2008, **130**, 318.

68. W. Haiss, S. Martin, E. Leary, H. Van Zalinge, S. J. Higgins, L. Bouffier and R. J. Nichols, *J. Phys. Chem. C*, 2009, **113**, 5823.

69. C. R. Arroyo, E. Leary, A. Castellanos-Gómez, G. Rubio-Bollinger, M. T. González and N. Agraït, *J. Am. Chem. Soc.*, 2011, **133**, 14313.

70. C.-C. Kaun and T. Seideman, *Phys. Rev. B*, 2008, **77**, 033414.

71. K. B. Dhungana, S. Mandal and R. Pati, *J. Phys. Chem. C*, 2012, **116**, 17268.

72. M. Tachibana, K. Yoshizawa, A. Ogawa, H. Fujimoto and R. Hoffmann, *J. Phys. Chem. B*, 2002, **106**, 12727.

73. M. Paulsson, C. Krag, T. Frederiksen and M. Brandbyge, *Nano Lett.*, 2009, **9**, 117.

74. S. Guo, J. Hihath, I. Diez-Perez and N. Tao, *J. Am. Chem. Soc.*, 2011, **133**, 19189.

75. W. R. French, C. R. Iacovella, I. Rungger, A. M. Souza, S. Sanvito and P. T. Cummings, *J. Phys. Chem. Lett.*, 2013, **4**, 887.

76. B. Xu, *Small*, 2007, **3**, 2061.

77. J. Zhou, G. Chen and B. Xu, *J. Phys. Chem. C*, 2010, **114**, 8587.

78. A. Halbritter, P. Makk, S. Mackowiak, S. Csonka, M. Wawrzyniak and J. Martinek, *Phys. Rev. Lett.*, 2010, **105**, 266805.

79. M. M. Wawrzyniak, J.; Susla, B.; Ilnicki, G., *Acta Phys. Pol., A*, 2009, **115**, 384.

80. M. Frei, S. V. Aradhya, M. S. Hybertsen and L. Venkataraman, *J. Am. Chem. Soc.*, 2012, **134**, 4003.

81. G. Michael, A. R. Mark and N. Abraham, *J. Phys.: Condens. Matter*, 2007, **19**, 103201.

82. J. C. Cuevas and E. Scheer, *Molecular Electronics an Introduction to Theory and Experiment*, **(World Scientific, 2010)**.

83. B. Q. Xu, X. Y. Xiao and N. J. Tao, *J. Am. Chem. Soc.*, 2003, **125**, 16164.

84. F. Demir and G. Kirczenow, *J. Chem. Phys.*, 2012, **136**, 014703.

85. J. Hihath, C. Bruot and N. Tao, *ACS Nano*, 2010, **4**, 3823.

86. I. Diez-Perez, J. Hihath, T. Hines, Z.-S. Wang, G. Zhou, K. Mullen and N. Tao, *Nat. Nanotech.*, 2011, **6**, 226.

87. J. Hihath and N. Tao, *Semicond. Sci. Technol.* , 2014, **29**, 054007.

88. J. M. Beebe, V. B. Engelkes, J. Liu, J. J. Gooding, P. K. Eggers, Y. Jun, X. Zhu, M. N. Paddon-Row and C. D. Frisbie, *J. Phys. Chem. B*, 2005, **109**, 5207.

89. J. G. Simmons, *J. Appl. Phys.*, 1963, **34**, 1793.

90. H. B. Akkerman, R. C. G. Naber, B. Jongbloed, P. A. van Hal, P. W. M. Blom, D. M. de Leeuw and B. de Boer, *Proc. Nat. Acad. Sci. USA* 2007, **104**, 11161.

91. R. I. Frank and J. G. Simmons, *J. Appl. Phys.* , 1967, **38**, 832.

92. J. Zhou, C. Guo and B. Xu, *J. Phys.: Condens. Matter*, 2012, **24**.

93. J. Zhou and B. Xu, *Appl. Phys. Lett.*, 2011, **99**, 042104.

94. H. B. Akkerman and B. de Boer, *J. Phys.: Condens. Matter*, 2008, **20**, 013001.

95. H. Rascón-Ramos, J. M. Artés, Y. Li and J. Hihath, *Nat. Mater.*, 2015, **14**, 517.

96. C. Van Dyck and M. A. Ratner, *Nano Lett.*, 2015, **15**, 1577.

97. C. Jin, M. Strange, T. Markussen, G. C. Solomon and K. S. Thygesen, *J. Chem. Phys.*, 2013, **139**, 184307.

98. M. Tsutsui, M. Taniguchi and T. Kawai, *J. Am. Chem. Soc.*, 2009, **131**, 10552.

99. M. Kiguchi, S. Miura, T. Takahashi, K. Hara, M. Sawamura and K. Murakoshi, *J. Phys. Chem. C*, 2008, **112**, 13349.

100. K. Wang, J. Zhou, J. M. Hamill and B. Xu, *J. Chem. Phys.*, 2014, **141**, 054712.

101. Kim, J. M. Beebe, Y. Jun, X. Y. Zhu and C. D. Frisbie, *J. Am. Chem. Soc.* , 2006, **128**, 4970.

102. M. Kamenetska, S. Y. Quek, A. C. Whalley, M. L. Steigerwald, H. J. Choi, S. G. Louie, C. Nuckolls, M. S. Hybertsen, J. B. Neaton and L. Venkataraman, *J. Am. Chem. Soc.*, 2010, **132**, 6817.

103. P. Moreno-García, M. Gulcur, D. Z. Manrique, T. Pope, W. Hong, V. Kaliginedi, C. Huang, A. S. Batsanov, M. R. Bryce, C. Lambert and T. Wandlowski, *J. Am. Chem. Soc.*, 2013, **135**, 12228.

104. B. Xu, P. Zhang, X. Li and N. Tao, *Nano Lett.*, 2004, **4**, 1105.

105. Y. S. Park, A. C. Whalley, M. Kamenetska, M. L. Steigerwald, M. S. Hybertsen, C. Nuckolls and L. Venkataraman, *J. Am. Chem. Soc.*, 2007, **129**, 15768.

106. M. Frei, S. V. Aradhya, M. Koentopp, M. S. Hybertsen and L. Venkataraman, *Nano Lett.*, 2011, **11**, 1518.

107. W. Wenyong, L. Takhee and A. R. Mark, *Rep. Prog. Phys.*, 2005, **68**, 523.

108. J. R. Widawsky, W. Chen, H. Vázquez, T. Kim, R. Breslow, M. S. Hybertsen and L. Venkataraman, *Nano Lett.*, 2013, **13**, 2889.

109. F. Chen, X. Li, J. Hihath, Z. Huang and N. Tao, *J. Am. Chem. Soc.*, 2006, **128**, 15874.

110. B. Kim, S. H. Choi, X. Y. Zhu and C. D. Frisbie, *J. Am. Chem. Soc.*, 2011, **133**, 19864.

111. A. J. Bergren, R. L. McCreery, S. R. Stoyanov, S. Gusarov and A. Kovalenko, *J. Phys. Chem. C*, 2010, **114**, 15806.

112. I. Bâldea and H. Köppel, *Phys. Status Solidi B*, 2012, **249**, 1791.

113. I. Franco, G. C. Solomon, G. C. Schatz and M. A. Ratner, *J. Am. Chem. Soc.*, 2011, **133**, 15714.

114. I. Franco, C. B. George, G. C. Solomon, G. C. Schatz and M. A. Ratner, *J. Am. Chem. Soc.*, 2011, **133**, 2242.

115. S. M. Parker, M. Smeu, I. Franco, M. A. Ratner and T. Seideman, *Nano Lett.*, 2014, **14**, 4587.

116. C. Bruot, J. Hihath and N. Tao, *Nat. Nanotech.*, 2012, **7**, 35.

117. K. Wang, J. M. Hamill, B. Wang, C. Guo, S. Jiang, Z. Huang and B. Xu, *Chem. Sci.*, 2014, **5**, 3425.

118. A. Batra, P. Darancet, Q. Chen, J. S. Meisner, J. R. Widawsky, J. B. Neaton, C. Nuckolls and L. Venkataraman, *Nano Lett.*, 2013, **13**, 6233.

119. S. K. Yee, J. Sun, P. Darancet, T. D. Tilley, A. Majumdar, J. B. Neaton and R. A. Segalman, *ACS Nano*, 2011, **5**, 9256.

120. E. Loertscher, B. Gotsmann, Y. Lee, L. Yu, C. Rettner and H. Riel, *ACS Nano*, 2012, **6**, 4931.

121. X. Chen, S. Yeganeh, L. Qin, S. Li, C. Xue, A. B. Braunschweig, G. C. Schatz, M. A. Ratner and C. A. Mirkin, *Nano Lett.*, 2009, **9**, 3974.

122. C. Toher, I. Rungger and S. Sanvito, *Phys. Rev. B*, 2009, **79**, 205427.

123. G.-P. Zhang, G.-C. Hu, Y. Song, Z.-L. Li and C.-K. Wang, *J. Phys. Chem. C*, 2012, **116**, 22009.

124. Y. Lee, B. Carsten and L. Yu, *Langmuir*, 2009, **25**, 1495.

125. M. Kiguchi, H. Nakamura, Y. Takahashi, T. Takahashi and T. Ohto, *J. Phys. Chem. C*, 2010, **114**, 22254.

126. Y. Q. Xue and M. A. Ratner, *Phys. Rev. B*, 2003, **68**, 115406.

127. H. Song, Y. Kim, Y. H. Jang, H. Jeong, M. A. Reed and T. Lee, *Nature*, 2009, **462**, 1039.

128. S. Y. Quek, L. Venkataraman, H. J. Choi, S. G. Louie, M. S. Hybertsen and J. B. Neaton, *Nano Lett.*, 2007, **7**, 3477.

129. X. Y. Xiao, B. Q. Xu and N. J. Tao, *Nano Lett.*, 2004, **4**, 267.

130. P. E. Kornilovitch, A. M. Bratkovsky and R. S. Williams, *Phys. Rev. B*, 2002, **66**, 165436.

131. R. Liu, S. H. Ke, W. T. Yang and H. U. Baranger, *J. Chem. Phys.*, 2006, **124**, 024718.

132. N. Armstrong, R. C. Hoft, A. McDonagh, M. B. Cortie and M. J. Ford, *Nano Lett.*, 2007, **7**, 3018.

133. C. A. Nijhuis, W. F. Reus and G. M. Whitesides, *J. Am. Chem. Soc.*, 2010, **132**, 18386.

134. J. Zhao, C. Yu, N. Wang and H. Liu, *J. Phys. Chem. C*, 2010, **114**, 4135.

135. S. Miranda-Rojas, A. Munoz-Castro, R. Arratia-Perez and F. Mendizabal, *Phys. Chem. Chem. Phys.*, 2013, **15**, 20363.

136. J. M. Beebe, B. Kim, J. W. Gadzuk, C. D. Frisbie and J. G. Kushmerick, *Phys. Rev. Lett.*, 2006, **97**, 026801.

137. B. M. Briechle, Y. Kim, P. Ehrenreich, A. Erbe, D. Sysoiev, T. Huhn, U. Groth and E. Scheer, *Beilstein J. Nanotech.*, 2012, **3**, 798.

138. B. Cui, Y. Xu, G. Ji, H. Wang, W. Zhao, Y. Zhai, D. Li and D. Liu, *Org. Electron.* , 2014, **15**, 484.

139. G. J. Ashwell, B. Urasinska and W. D. Tyrrell, *Phys. Chem. Chem. Phys.*, 2006, **8**, 3314.

140. G. J. Ashwell, W. D. Tyrrell and A. J. Whittam, *J. Am. Chem. Soc.*, 2004, **126**, 7102.

141. D. Cees and R. Mark, *Phys. World*, 2001, **14**, 29.

142. Y. Ye, L. Chen, X. Liu and U. J. Krull, *Anal. Chim. Acta*, 2006, **568**, 138.

143. J. C. Genereux and J. K. Barton, *Chem. Rev.*, 2010, **110**, 1642.

144. S. S. Mallajosyula and S. K. Pati, *J. Phys. Chem. Lett.*, 2010, **1**, 1881.

145. E. Braun, Y. Eichen, U. Sivan and G. Ben-Yoseph, *Nature*, 1998, **391**, 775.

146. P. Tran, B. Alavi and G. Gruner, *Phys. Rev. Lett.*, 2000, **85**, 1564.

147. R. N. Barnett, C. L. Cleveland, A. Joy, U. Landman and G. B. Schuster, *Science*, 2001, **294**, 567.

148. Y. A. Mantz, F. L. Gervasio, T. Laino and M. Parrinello, *Phys. Rev. Lett.*, 2007, **99**, 058104.

149. R. G. Endres, D. L. Cox and R. R. P. Singh, *Rev. Mod. Phys.*, 2004, **76**, 195.

150. A. Rich, *Gene*, 1993, **135**, 99.

151. P. Vasudevaraju, Bharathi, R. M. Garruto, K. Sambamurti and K. S. J. Rao, *Brain Res. Rev.*, 2008, **58**, 136.

152. H. Hamada, M. G. Petrino and T. Kakunaga, *Proc. Natl. Acad. Sci. U. S. A.*, 1982, **79**, 6465.

153. A. Rich, A. Nordheim and A. H. J. Wang, *Annu. Rev. Biochem.*, 1984, **53**, 791.

154. F. M. Pohl and T. M. Jovin, *J. Mol. Biol.*, 1972, **67**, 375.

155. J. H. van de Sande, L. P. McIntosh and T. M. Jovin, *EMBO J.*, 1982, **1**, 777.

156. A. Krzyźaniak, P. Salański, J. Jurczak and J. Barciszewski, *FEBS Lett.*, 1991, **279**, 1.

157. V. I. Ivanov, L. E. Minchenkova, E. E. Minyat, M. D. Frank-Kamenetskii and A. K. Schyolkina, *J. Mol. Biol.*, 1974, **87**, 817.

158. J. Zheng, Z. Li, A. Wu and H. Zhou, *Biophys. Chem.*, 2003, **104**, 37.

159. K. Siriwong and A. A. Voityuk, *J. Phys. Chem. B*, 2008, **112**, 8181.

160. S. S. Mallajosyula, A. Gupta and S. K. Pati, *J. Phys. Chem. A*, 2009, **113**, 3955.

161. D. R. Latulippe and A. L. Zydney, *Biotechnol. Bioeng.*, 2008, **99**, 390.

162. F. L. Gervasio, P. Carloni and M. Parrinello, *Phys. Rev. Lett.*, 2002, **89**, 108102.

163. R. Gutiérrez, S. Mandal and G. Cuniberti, *Nano Lett.*, 2005, **5**, 1093.

164. B. X. Z. Huang, Y. Chen, M. Di Ventra, N. Tao, *Nano Lett.*, 2006, **6**, 1240.

165. I. Horcas, R. Fernández, J. M. Gómez-Rodríguez, J. Colchero, J. Gómez-Herrero and A. M. Baro, *Rev. Sci. Instrum.*, 2007, **78**, 013705.

166. J. Hihath, B. Xu, P. Zhang and N. Tao, *Proc. Natl. Acad. Sci. U. S. A.*, 2005, **102**, 16979.

167. S. Lindsay, *Faraday Discuss.*, 2006, **131**, 403.

168. E. Wierzbinski, R. Venkatramani, K. L. Davis, S. Bezer, J. Kong, Y. Xing, E. Borguet, C. Achim, D. N. Beratan and D. H. Waldeck, *ACS Nano*, 2013, **7**, 5391.

169. H. van Zalinge, D. J. Schiffrin, A. D. Bates, W. Haiss, J. Ulstrup and R. J. Nichols, *ChemPhysChem*, 2006, **7**, 94.

170. S. Brahms and J. G. Brahms, *Nucleic Acids Res.*, 1990, **18**, 1559.

171. E. Segal and J. Widom, *Curr. Opin. Struct. Biol.*, 2009, **19**, 65.

172. J. H. van de Sande and T. M. Jovin, *EMBO J.*, 1982, **1**, 115.

173. T. Miyahara, H. Nakatsuji and H. Sugiyama, *J. Phys. Chem. A*, 2013, **117**, 42.

174. P. Várnai and Y. Timsit, *Nucleic Acids Res.* , 2010, **38**, 4163.

175. E. Hamori and T. M. Jovin, *Biophys. Chem.*, 1987, **26**, 375.

176. S. K. Zavriev, L. E. Minchenkova, M. Vorlíčková, A. M. Kolchinsky, M. V. Volkenstein and V. I. Ivanov, *Biochim. Biophys. Acta, Nucleic Acids Protein Synth.*, 1979, **564**, 212.

177. F. J. Ramírez, T. J. Thomas, T. Antony, J. Ruiz-Chica and T. Thomas, *Biopolymers*, 2002, **65**, 148.

178. G. S. Kumar and M. Maiti, *J. Biomol. Struct. Dyn.*, 1994, **12**, 183.

179. G. J. Puppels, C. Otto, J. Greve, M. Robert-Nicoud, D. J. Arndt-Jovin and T. M. Jovin, *Biochemistry*, 1994, **33**, 3386.

180. C. R. Treadway, M. G. Hill and J. K. Barton, *Chem. Phys.*, 2002, **281**, 409.

181. A. Hübsch, R. G. Endres, D. L. Cox and R. R. P. Singh, *Phys. Rev. Lett.*, 2005, **94**, 178102.

182. H. Ikeura-Sekiguchi and T. Sekiguchi, *Phys. Rev. Lett.*, 2007, **99**, 228102.

183. R. V. Gessner, G. J. Quigley, A. H. J. Wang, G. A. Van der Marel, J. H. Van Boom and A. Rich, *Biochemistry*, 1985, **24**, 237.

184. V. V. Zakjevskii, S. J. King, O. Dolgounitcheva, V. G. Zakrzewski and J. V. Ortiz, *J. Am. Chem. Soc.*, 2006, **128**, 13350.

185. M. S. José, A. Emilio, D. G. Julian, G. Alberto, J. Javier, O. Pablo and S.-P. Daniel, *J. Phys.: Condens. Matter*, 2002, **14**, 2745.

186. M. Di Ventra and Y. V. Pershin, *Nat. Nanotech.*, 2011, **6**, 198.

187. J. C. Genereux and J. K. Barton, *Nat. Chem.*, 2009, **1**, 106.

188. G. I. Livshits, A. Stern, D. Rotem, N. Borovok, G. Eidelshtein, A. Migliore, E. Penzo, S. J. Wind, R. Di Felice, S. S. Skourtis, J. C. Cuevas, L. Gurevich, A. B. Kotlyar and D. Porath, *Nat. Nanotech.*, 2014, **9**, 1040.

189. B. Giese, J. Amaudrut, A.-K. Kohler, M. Spormann and S. Wessely, *Nature*, 2001, **412**, 318.

190. F. D. Lewis, X. Liu, J. Liu, S. E. Miller, R. T. Hayes and M. R. Wasielewski, *Nature*, 2000, **406**, 51.

191. L. Xiang, J. L. Palma, C. Bruot, V. Mujica, M. A. Ratner and N. Tao, *Nat. Chem.*, 2015, **7**, 221.

192. H. Joshua, G. Shaoyin, Z. Peiming and T. Nongjian, *J. Phys.: Condens. Matter*, 2012, **24**, 164204.

193. M. Tsutsui, K. Matsubara, T. Ohshiro, M. Furuhashi, M. Taniguchi and T. Kawai, *J. Am. Chem. Soc.*, 2011, **133**, 9124.

194. H. Liu, G. Li, H. Ai, J. Li and Y. Bu, *J. Phys. Chem. C*, 2011, **115**, 22547.

195. S. Liu, G. H. Clever, Y. Takezawa, M. Kaneko, K. Tanaka, X. Guo and M. Shionoya, *Angew. Chem. Int. Ed.* , 2011, **50**, 8886.

196. M. Elbing, R. Ochs, M. Koentopp, M. Fischer, C. von Hänisch, F. Weigend, F. Evers, H. B. Weber and M. Mayor, *Proc. Natl. Acad. Sci. U. S. A.*, 2005, **102**, 8815.

197. H. J. Yoon, K.-C. Liao, M. R. Lockett, S. W. Kwok, M. Baghbanzadeh and G. M. Whitesides, *J. Am. Chem. Soc.*, 2014, **136**, 17155.

198. Ö. Persil, C. T. Santai, S. S. Jain and N. V. Hud, *J. Am. Chem. Soc.*, 2004, **126**, 8644.

199. M. Polak and N. V. Hud, *Nucleic Acids Res.*, 2002, **30**, 983.

200. J. Ren and J. B. Chaires, *Biochemistry*, 1999, **38**, 16067.

201. R. Stadler, V. Geskin and J. Cornil, *J. Phys.: Condens. Matter*, 2008, **20**, 374105.

202. C. Huang, A. V. Rudnev, W. Hong and T. Wandlowski, *Chem. Soc. Rev.*, 2015, **44**, 889.

203. B. Capozzi, Q. Chen, P. Darancet, M. Kotiuga, M. Buzzeo, J. B. Neaton, C. Nuckolls and L. Venkataraman, *Nano Lett.*, 2014, **14**, 1400.

204. J. C. Genereux, S. M. Wuerth and J. K. Barton, *J. Am. Chem. Soc.*, 2011, **133**, 3863.

205. B. Tan, M. Hodak, W. Lu and J. Bernholc, *Phys. Rev. B*, 2015, **92**, 075429.

206. D. Brisker-Klaiman and U. Peskin, *J. Phys. Chem. C*, 2010, **114**, 19077.

207. E. M. G. Cuniberti, A. Rodríguez, R. A. Römer, *Tight-Binding Modeling of Charge Migration in DNA Devices*, Springer, 2007.

208. J. Yi, *Phys. Rev. B*, 2003, **68**, 193103.

209. N. Grib, D. Ryndyk, R. Gutiérrez and G. Cuniberti, *J. Biophys. Chem.*, 2010, **1**, 77.

210. J. Jortner, M. Bixon, A. A. Voityuk and N. Rösch, *J. Phys. Chem. A*, 2002, **106**, 7599.

211. A. A. Voityuk, J. Jortner, M. Bixon and N. Rösch, *Chem. Phys. Lett.*, 2000, **324**, 430.

212. A. A. Voityuk, N. Rösch, M. Bixon and J. Jortner, *J. Phys. Chem. B*, 2000, **104**, 9740.

213. X. Bingqian and D. Yonatan, *J. Phys.: Condens. Matt.* , 2015, **27**, 263202.

214. C. J. O. Verzijl, J. S. Seldenthuis and J. M. Thijssen, *J. Chem. Phys.*, 2013, **138**, 094102.

215. D. Vanderbilt and S. G. Louie, *J. Comput. Phys.*, 1984, **56**, 259.

216. A. M. Nowak and R. L. McCreery, *J. Am. Chem. Soc.*, 2004, **126**, 16621.

217. X. D. Cui, A. Primak, X. Zarate, J. Tomfohr, O. F. Sankey, A. L. Moore, T. A. Moore, D. Gust, G. Harris and S. M. Lindsay, *Science*, 2001, **294**, 571.

218. V. Fatemi, M. Kamenetska, J. B. Neaton and L. Venkataraman, *Nano Lett.*, 2011, **11**, 1988.

219. E. Leary, H. Höbenreich, S. J. Higgins, H. van Zalinge, W. Haiss, R. J. Nichols, C. M. Finch, I. Grace, C. J. Lambert, R. McGrath and J. Smerdon, *Phys. Rev. Lett.*, 2009, **102**, 086801.

220. B. Choi, B. Capozzi, S. Ahn, A. Turkiewicz, G. Lovat, C. Nuckolls, M. L. Steigerwald, L. Venkataraman and X. Roy, *Chem. Sci.*, 2016, **7**, 2701.

221. D. C. Milan, O. A. Al-Owaedi, M.-C. Oerthel, S. Marqués-González, R. J. Brooke, M. R. Bryce, P. Cea, J. Ferrer, S. J. Higgins, C. J. Lambert, P. J. Low, D.

Z. Manrique, S. Martin, R. J. Nichols, W. Schwarzacher and V. M. García-Suárez, *J. Phys. Chem. C*, 2016, **120**, 15666.

222. R. García, M. Á. Herranz, E. Leary, M. T. González, G. R. Bollinger, M. Bürkle, L. A. Zotti, Y. Asai, F. Pauly, J. C. Cuevas, N. Agraït and N. Martín, *Beilstein J. Org. Chem.*, 2015, **11**, 1068.

223. B. S. T. Kasibhatla, A. P. Labonté, F. Zahid, R. G. Reifenberger, S. Datta and C. P. Kubiak, *J. Phys. Chem. B*, 2003, **107**, 12378.

224. J. Del Re, M. H. Moore, B. R. Ratna and A. Szuchmacher Blum, *Phys. Chem. Chem. Phys.*, 2013, **15**, 8318.

225. W. Zhang, S. Gan, A. Vezzoli, R. J. Davidson, D. C. Milan, K. V. Luzyanin, S. J. Higgins, R. J. Nichols, A. Beeby, P. J. Low, B. Li and L. Niu, *ACS Nano*, 2016, **10**, 5212.

226. S. Martín, I. Grace, M. R. Bryce, C. Wang, R. Jitchati, A. S. Batsanov, S. J. Higgins, C. J. Lambert and R. J. Nichols, *J. Am. Chem. Soc.*, 2010, **132**, 9157.

227. S. Wu, M. T. Gonzalez, R. Huber, S. Grunder, M. Mayor, C. Schonenberger and M. Calame, *Nat. Nanotech.*, 2008, **3**, 569.

228. S. T. Schneebeli, M. Kamenetska, Z. Cheng, R. Skouta, R. A. Friesner, L. Venkataraman and R. Breslow, *J. Am. Chem. Soc.*, 2011, **133**, 2136.

229. T. Ghane, D. Nozaki, A. Dianat, A. Vladyka, R. Gutierrez, J. P. Chinta, S. Yitzchaik, M. Calame and G. Cuniberti, *J. Phys. Chem. C*, 2015, **119**, 6344.

230. T. Nishino, N. Hayashi and P. T. Bui, *J. Am. Chem. Soc.*, 2013, **135**, 4592.

231. S. Chang, J. He, A. Kibel, M. Lee, O. Sankey, P. Zhang and S. Lindsay, *Nat. Nanotech.*, 2009, **4**, 297.

232. J. Janata, *Electroanalysis*, 2004, **16**, 1831.

233. J. Ferraris, D. O. Cowan, V. Walatka and J. H. Perlstein, *J. Am. Chem. Soc.*, 1973, **95**, 948.

234. D. Jérome, A. Mazaud, M. Ribault and K. Bechgaard, *J. Physique Lett.*, 1980, **41**, 95.

235. D. B. G. Williams and M. Lawton, *J. Org. Chem.* , 2010, **75**, 8351.

236. B. J. J. Smeets, R. H. Meijer, J. Meuldijk, J. A. J. M. Vekemans and L. A. Hulshof, *Org. Process Res. Dev.*, 2003, **7**, 10.

237. N. Robertson and C. A. McGowan, *Chem. Soc. Rev.*, 2003, **32**, 96.

238. N. Stuhr-Hansen, J. K. Sørensen, K. Moth-Poulsen, J. B. Christensen, T. Bjørnholm and M. B. Nielsen, *Tetrahedron*, 2005, **61**, 12288.

239. R. S. Klausen, J. R. Widawsky, T. A. Su, H. Li, Q. Chen, M. L. Steigerwald, L. Venkataraman and C. Nuckolls, *Chem. Sci.*, 2014, **5**, 1561.

240. C. Bruot, J. L. Palma, L. Xiang, V. Mujica, M. A. Ratner and N. Tao, *Nat. Commun.*, 2015, **6**, 8032.

241. M. Galperin and A. Nitzan, *Phys. Chem. Chem. Phys.*, 2012, **14**, 9421.

242. S. Battacharyya, A. Kibel, G. Kodis, P. A. Liddell, M. Gervaldo, D. Gust and S. Lindsay, *Nano Lett.*, 2011, **11**, 2709.

243. A. C. Aragonès, D. Aravena, J. I. Cerdá, Z. Acís-Castillo, H. Li, J. A. Real, F. Sanz, J. Hihath, E. Ruiz and I. Díez-Pérez, *Nano Lett.*, 2016, **16**, 218.